Department of Precision and Microsystems Engineering

Vacuum induced membrane end-effector for micro laminates

Filippus Hulsman

Report no : 2022.077
Professor : Dr. ir. Marcel Tichem
Specialisation : Micro and nano engineering
Type of report : MSc Thesis
Date : 16 november 2022

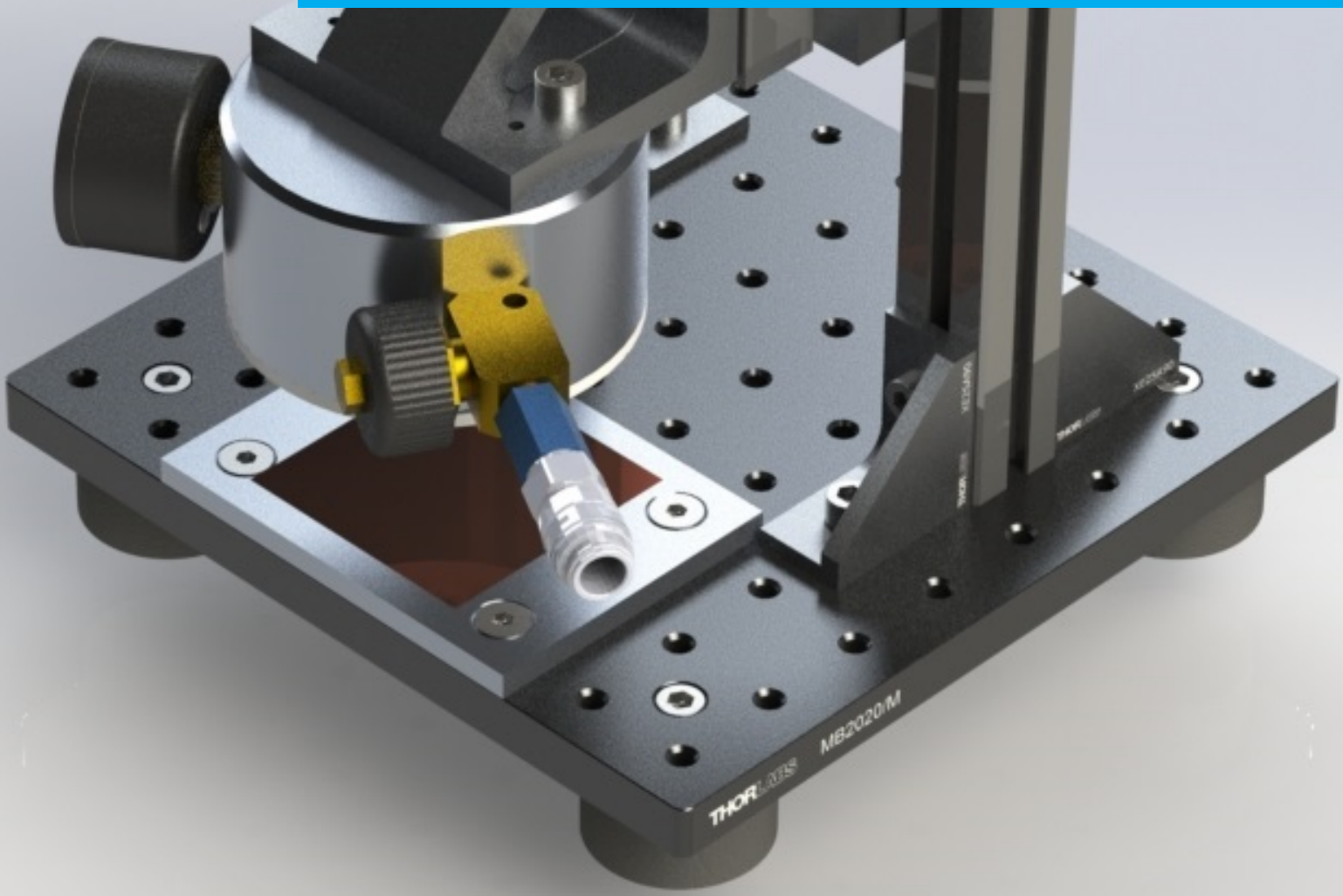

Summary

The research investigates the creation of an end-effector capable of pick-and-placing thin laminates of various materials. The chosen end-effector design induces a pressure differential with a membrane, and is capable to achieve a large switching force ($\approx 50\,kPa$) for various delicate and geometric complex laminates. The concept utilizes an array of holes, over which a membrane is suspended, hereafter called suction cups. By applying pressure upon the suction cups, the membrane deforms, resulting in a vacuum capable of generating large switching forces. During contact the vacuum is created, and during release the membranes are expanded to release the laminate.
The design variables (radius, membrane height, membrane thickness, Young's modulus of membrane) of the concept are numerically investigated to analyze their influence on the suction pressure, the deformation of the membrane and the corresponding stresses in membrane and laminate. The numerical results indicated that the membrane thickness and material are vital. As an increase in thickness and young's modulus results in an exponential increase in switching force. These numerical results and the end-effector production method determine the final dimensions.The prototype is then used to perform a set of experiments to validate the numerical model.

The measurement results on the deformation of the end-effector membrane confirm model results. However, production inaccuracies and the application method of the membrane resulted in inconsistencies in the dimensions and its performance. The force measurement results indicate that the force created by the end-effector is heavily impeded by the sealing performance of the suction-cups. Improving the sealing performance resulted in values in accordance with the numerical model. The pick-and-place experiment indicates that a substantial force is created by the suction cups, capable of pick-and-placing rigid laminates. For the transportation of flexible laminates (thinner and/or smaller young's modulus), smaller forces are created due to the compliance of the laminate, therefore more accurate production and a thinner and more flexible membrane is required.
Depending on the laminate material and shape, certain design guidelines are in place. A larger force can be created on more rigid laminates, allowing for the application of a less flexible membrane. For thinner laminates the switching force is reduced, and therefore the membrane needs to be very flexible and thin. For a more complex shape, smaller and more suction cups are required, impacting the other variables. Additional guidelines for various laminate materials and shapes are found at the end of this report.

In conclusion, an end-effector based on the membrane induced pressure differential is a design path which is worth investigating further for pick-and-placing thin laminates. Depending on the application and thus the target laminates, certain design guidelines are set up at the end of this report. These can be used for further research to pick-and-place geometric intricate laminates of various materials.

Contents

1. Introduction

Metamaterials are used in many fields, ranging from artificial muscles and bio-mimetic materials [1] to enhancing the sensitivity and resolution of sensors [2] and noise-dampening/ -shielding materials [3]. Metamaterials consisting out of multiple materials can be applied in many fields and improve material performance [1]. An example of such multi-material structures are acoustic metafoams which are constructed by creating mass variations within materials with varying densities [4, 5]. The full exploitation of the potential of meta-materials offers the users innovation in countless applications.

Metamaterials are currently mainly produced with point-based production methods (3D printing) which limit the material diversity [6, 7]. Furthermore, literature has shown that the currently applied methods lack not only in material diversity but also in throughput [1]. Thus, the current production methods are restrictive, limiting the material characteristics [1, 8], and thus limits the freedom of design and wider real-world applications.

Therefore, an alternate production method is investigated: additive manufacturing by pick-and-placing laminates. This method stacks 2.5D sheets (laminates) for the creation of multi-material architectures. Literature has shown that pick and placing laminates is a promising method for the creation of these structures [8]. This is mainly because the method enables a large variety in materials and interlayer adhesive methods. Additionally, it is a method which gives flexibility in the creation method of the various laminates, which can be optimized to achieve high throughput.

The exact material characteristics required is very dependent on its application, therefore a few key characteristics are listed which are expected for the new multi-material metamaterials. These characateristics are:

- skeletal structure made from material A with local application of material B,
- large area manufacturing (10x10 cm),
- unit cell scale in the range of 100 µm to 1000 µm,
- high throughput production (Piece cost reduction),
- complex 3-dimensional geometries,
- repetitive layered structure, and
- mainly hollow structures.

The most important new material characteristic is the creation of multi-material architectures, as it allows for the creation of new materials with new features. The applied laminate materials can differ, resulting in a single multi-material architecture consisting out of widely different material properties. Thus, the designed end-effector must be compatible for laminates with different material properties.
Additionally, to achieve the construction of meta-materials with a unit cell of approx 100 µm - 1000 µm, the handling of thin laminates (10-50 µm) with a relative large area (10x10 cm) is a vital feature to enable the creation of larger structures. This requires very delicate handling to not destroy or deform the laminates.

Throughout this report, the goal is to create an end-effector which is capable to delicately pick-and-place thin large area laminates constructed from a wide range of constituent materials for the creation of meta-materials with the characteristics mentioned before. This report starts with the process details in chapter 2 by describing the process flow, the suspected interaction energies and the corresponding boundary conditions which must be considered during design. In chapter 3, six end-effector concepts are investigated with their corresponding working principles and equations. This is followed by a set of criteria and a concept selection to choose the most promising end-effector design. In chapter 4 the mechanical design of the concept is further investigated with a MATLAB model. This numerical model is used to highlight the underlying relations between the variables and to finally predict the performance of the produced end-effector. This model is closely used during production and dimensioning of the end-effector. In chapter 5 the final end-effector

production method is explained together with the final dimensions. In chapter 6 three main experiments are explained which are used to validate the constructed model and test the end-effector performance. In chapter 7 the results of the experiments are documented which is directly analyzed in the discussion. These results finally quantifies the end-effector performance to either validate or reject the concept design.

2. Lamination strategy

2.1. Lamination process flow

In this chapter, the pick and place strategy and its process is elaborated. The process to create the multi material architecture is repetitive and is done in five steps as seen in figure 2.1a. Additionally, the force types acting upon each laminate in each step are shown in figure 2.1b and figure 2.1c. In the process, as the laminates are thin and have a large area, interaction force must be considered. These are further elaborated in section 2.2. In the following paragraphs, every step is systematically analyzed.

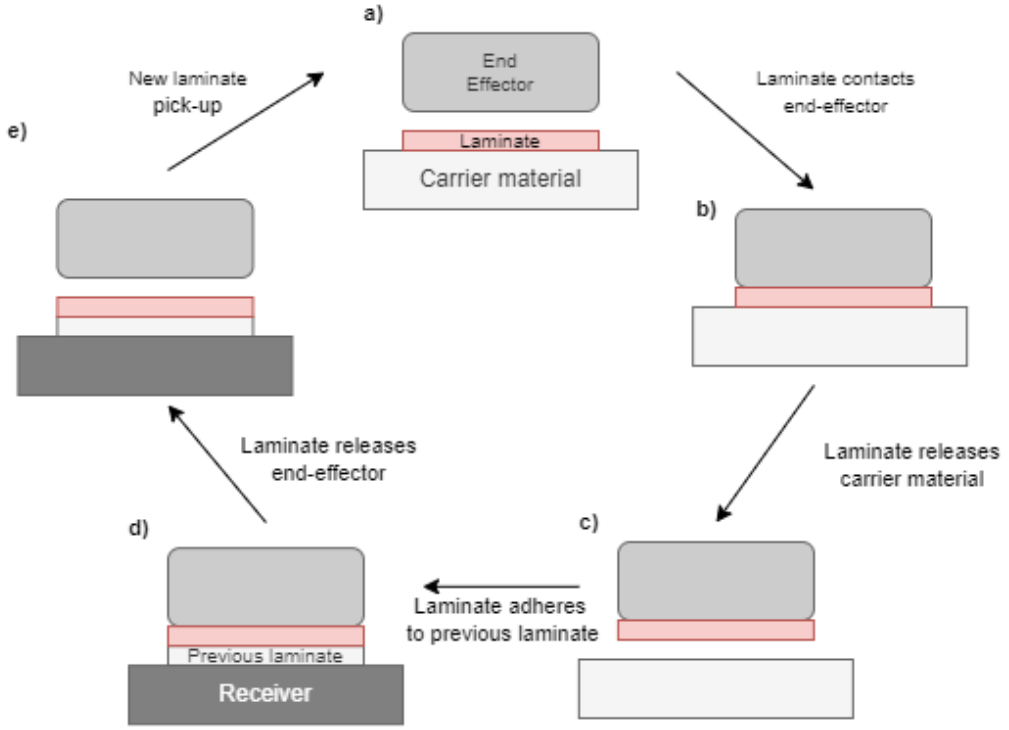

(a) Schematic illustration of laminate placement.

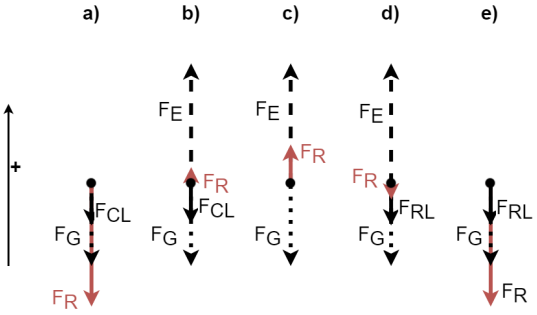

(b) Illustration of the forces acting upon the laminate.

(a)	$\bar{F}_G + \bar{F}_{CL} < 0$	$F_R < 0$
(b)	$\bar{F}_G + \bar{F}_{CL} + \bar{F}_E \geq 0$	$F_R \geq 0$
(c)	$\bar{F}_G + \bar{F}_E > 0$	$F_R > 0$
(d)	$\bar{F}_G + \bar{F}_{RL} + \bar{F}_E \leq 0$	$F_R \leq 0$
(e)	$\bar{F}_G + \bar{F}_{RL} < 0$	$F_R < 0$

(c) Force balance equations.

Figure 2.1: The layer interaction force is denoted as F_{CL} & F_{RL} for respectively the Carrier material and Receiver material. This force is a combination of capillary, van der Waals, Casimir and electrostatic force. The force created by the end-effector is denoted as F_E and the gravitational force denoted as F_G. The resultant force is F_R and is denoted in red. During the process described in figure 2.1a the force balance shifts continuously to perform the desired transfer process.

In the first step, a laminate is on top of a carrier material and the end-effector is lined up correctly. The active forces are gravity (F_G) and the interaction forces between the laminate and the carrier material (F_{CL}).

In the second step, the end-effector contacts the laminate. Depending on the end-effector design, a compression force can be acted onto the laminate to ensure contact. After proper contact, the laminate is ready to be picked up. The end-effector is then actuated, creating a force (F_E). The force partly consists of interaction forces, but predominately consists of an additional pick-up force creation method (e.g. suction, peeling, adhesion etc.). For successful pickup, the forces must exceed the interaction force ($F_C L$) and gravity (F_G).

The third step is to finally pick up the laminate. As the laminate detaches, the interaction forces with the carrier material diminish. Thus, to maintain the position in this step, the required end-effector force must only exceed the gravity force acting upon the laminate. Thus, the force required to detach the laminate is larger than the force required to move the laminate.

In the fourth step, the laminate is put into contact with the build plate, where it is stacked unto the previously placed laminate. As the laminate is placed, an interaction force between the two laminates is present (F_{RL}). This force adheres the two laminates with each other.

In the final step, the end-effector is deactivated, reducing its force significantly. This allows for the release of the laminate. The only forces acting upon the laminate are F_G and F_{RL}. After release, the end-effector is moved back to its initial position and the cycle is repeated.

Within this cycle, all the interaction forces can variate. The interlayer interaction force (F_{RL}) changes depending on the previously placed material. The interaction force with the carrier material (F_{CL}) can be altered by adding a coating or additional surface roughness to either increase or decrease the laminate interaction force [9–13].

2.2. The interaction energies

As the laminates used have a much larger surface area compared to their thickness, it is important to consider the interaction forces as stated in figure 2.1c. These forces result from the following four interaction energies: Capillary, Casimir, van der Waals and Electrostatic. The electrostatic interaction force is only present in the form of contact potential, which is generally lower than the van der Waals [14, 15]. Temporary charging can occur during the process, but no permanent adhesion occurs due to the tribocharge relaxing over time. In general, the electrostatic force will not be a significant force during laminate transfer. Additional information on all interaction energies are shown in appendix D.

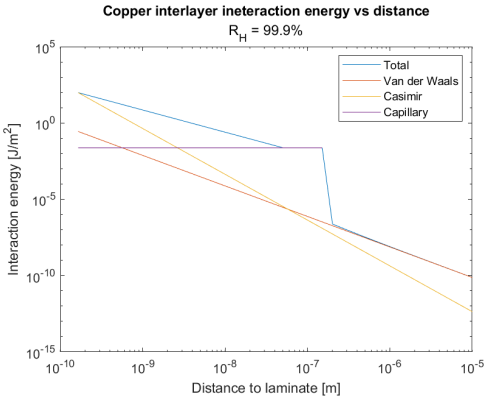

Figure 2.2: Overview of the interaction forces. Model uses copper as material and the max relative humidity (99.9%) achievable in the country of residence [16].

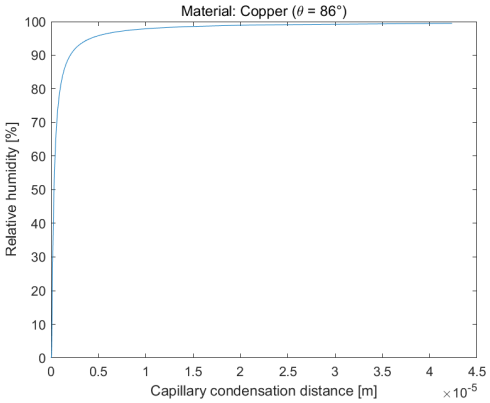

Figure 2.3: Cappillary condensation distance. This distance increases exponentially with higher relative humidity.

In figure 2.2 the interaction energy is plotted against the distance between two laminates. As can be seen in the figure, the interaction mechanisms have a variating impact. The smaller the mean distance is between two plates, the more dominant the Van der Waals effect will be. The Casimir force has the most effect if the mean distance is in the range of a few nanometers, which is rare for flat plates. The interaction force as a result of capillary condensation is the largest force when distances increase. The distance in which capillary condensation occurs is correlated to the relative humidity of the environment. As can be seen in figure 2.3 the

capillary condensation distance increases exponentially as a result of an increase in relative humidity. Thus, the relative humidity alters the capillary condensation distance (distance over which the capillary interaction energy is active) figure 2.2. Indicating that at a large relative humidity (<90%) and a mean distance larger than 0.6 nm that, the capillary interaction energy is the most dominant mechanism. This mechanism is material dependent due to the specific contact angle of the liquid-vapor interface of water and the corresponding laminate.
In reality the relative humidity is lower, and thus the capillary condensation distance decreases, resulting in large interaction forces at smaller distances to the laminate. Then the most dominate interaction energies would be created by the Casimir and Van der Waals.

In the process of picking up a laminate, the interaction forces (F_{CL}&F_{CR}) are acting upon the laminate. These forces can be adjusted by altering the surface area and surface roughness to fit in the design parameters of the concept.
In table 2.1, the interaction pressures with the carrier and receiver material are quantified for two vastly different laminates. These pressures are the base conditions of the end-effector to achieve successful laminate pick-up. The pressures (P_{CL}&P_{PR}) are independent of the area, and can be used as a guideline for the end-effector concept requirements. The materials are chosen based on their vastly different Young's modulus and density and their application in metafoams [4, 5]. The interaction pressures of table 2.1 are based on the material properties stated in appendix A and the equations and graphs listed in appendix B and appendix D.

These results indicate that the effect of the Casimir and Van der Waals interaction energies are significantly reduced when increasing the distance between the laminates. The capillary force is the only force that remains significant over larger interlayer distances. Increasing the material surface roughness and thus the mean distance between the layers can decrease the interaction forces enormously. Therefore, during production (chapter 5), the surface roughness is used as a design parameter.

Interaction parameter	**Symbol**	**Polyurethane**	**Copper - C11000**
Interaction pressures with carrier material (E_{CL})*			
Capillary	P_{Ca}	40.57 kPa	82.80 kPa
Van der Waals	P_{vdW}	1.61 Pa	1.67 Pa
Casimir	P_{Cs}	0.56 Pa	0.58 Pa
Interaction pressures with receiver material (E_{RL})*			
Capillary	P_{Ca}	112.01 kPa	253.75 kPa
Van der Waals	P_{vdW}	9.04 Pa	10.30 Pa
Casimir	P_{Cs}	5.55 Pa	6.61 Pa

Table 2.1: Interaction parameters between copper and polyurethane based on the various equations and variables indicated in table A.1.
*Forces are based on an aluminum carrier material and the receiver material is the previously pick-and-placed laminate (Copper or TPU).

3. Conceptualization

In this chapter, six end-effector concepts are investigated. The selection of concepts is based on literature findings [8], and are structured into two main groups, see figure 3.1. The first group of concepts utilizes interaction forces to pick up the laminate and during release applies a force by changing the contact area. The second group of concepts creates a pressure differential to initiate a force. All concepts are first investigated and are then compared to each other qualitatively to select the most promising concept. These six concepts are considered to create a selection of varying and promising end-effector solutions.

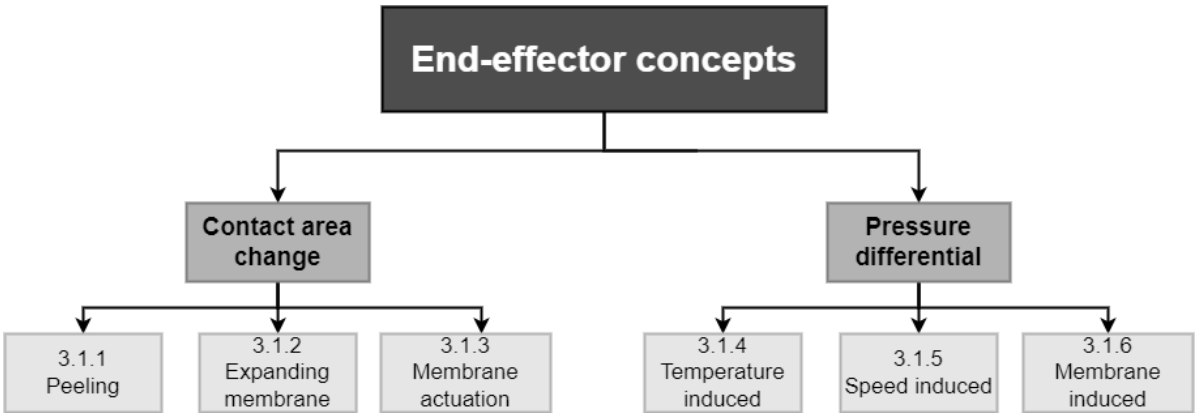

Figure 3.1: Concept categorization. Categorization is based on literature findings to create a variation of feasible concepts [8].

3.1. End-effector concepts

3.1.1. Contact area: Peeling

The first concept utilizes a polymer stamp (Polydimethylsiloxaan - PDMS) which adheres to the laminates to achieve pickup. Pick-up is achieved by applying a large bending radius to pick up the laminates from the substrate. Additionally, the stamp is moved relatively slow to achieve interlayer adhesion between the laminates and the PDMS stamp.
Release is achieved by rolling the stamp with a small radius, reducing the contact area and pushing away the laminates, see figure 3.2. The bending radius, speed and thickness of the stamp determines the force created. [17–20]. Reducing the stamp bending radius and thickness increases the pressure differential created on the peeling edge of the PDMS stamp during laminate release, see figure 3.3a and figure 3.3b. By increasing the peeling velocity, the release force can be increased [19]. This dependency is theoretically quantified with equation (3.1).

$$G_{crit}(v) = G_0\left[1 + \left(\frac{v}{v_0}\right)^n\right] \tag{3.1}$$

In which G_{crit} is the critical energy release rate for the stamp/film interface, G_0 is the critical energy release rate as indicated by a peeling velocity v, v_0 is the reference peeling velocity at which the critical energy release rate is doubled to G_0 and n is a scaling parameter that can be determined experimentally.

With this concept, pick-up is achieved by interaction forces and swiftly peeling the stamp with a tight bending radius is applied to release the laminate. The force created during release exerts a large force onto the receiver and its underlying laminates. With this concept, a pressure difference can be created of about 18 kPa.

3.1.2. Contact area: Expanding membrane

Membrane expansion is the process in which membranes are expanded to reduce the contact area and push away the target laminate [21–23]. In this concept, this is done through thermal expansion of air pockets in the end-effector. The laser heats the air in selective pockets rapidly, which results in thermal expansion and

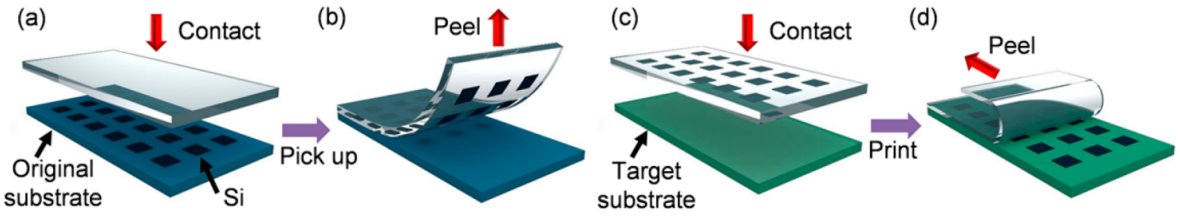

Figure 3.2: Schematic illustrations of a transfer printing procedure by controlling the bending radius of an elastomeric stamp. (a) Stamp brought into contact with the laminates to release them from the substrate. (b) Pick-up of laminates with a relatively large bending radius picks up the micro Si plates from the original substrate. (c) Stamp holding the micro Si plates is brought into contact with the target substrate. (d) Stamp is peeled away swiftly with a tight bending radius to release laminates. [17]

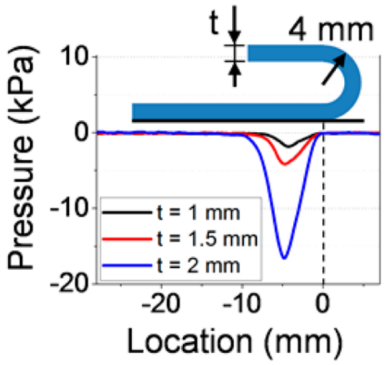

(a) Release pressure created for varying stamp thicknesses.

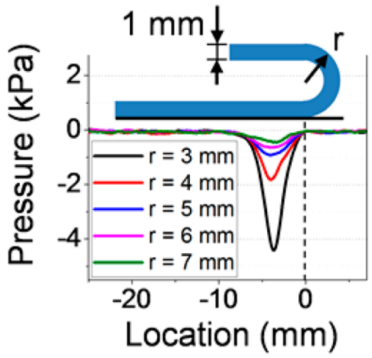

(b) Release pressure created for varying bending radii.

Figure 3.3: Release pressure distributions with varying stamp thicknesses and radii. Measurements are done with micro silicon plates (size - 760× 760 µm; thickness - 7 µm)

thus the membrane deforms, see figure 3.4. Pick-up is achieved by utilizing the interlayer forces. Releasing rigid laminates is achieved by pushing away the laminate and by reducing the contact area. The deformation of the membrane reduces the contact area, which decreases the interaction forces.

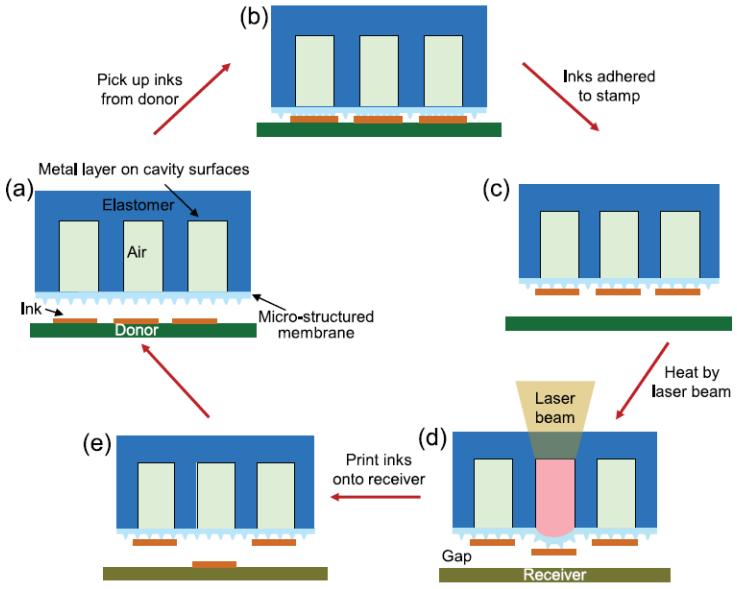

Figure 3.4: Schematic illustration of the laser-driven programmable balloon concept [21].

For flexible laminates, the expansion of the membrane only results in laminate deformation, and thus in-

teraction forces remain dominant, and no release force is exerted. Release of the laminates is achieved by thermal stresses, which are induced by the different expansion rates of the membrane and laminate. As the membrane is heated, thermal expansion occurs, resulting in thermal tangential stresses achieving laminate release. This process requires matching thermal and mechanical properties of the stamp and laminate, e.g. material interface, properties, thickness, and the absorbed laser power [23].
Due to the number of parameters, a large switching force can be created for a multitude of laminates, both flexible and rigid. This results in a versatile concept which allows for a fast and selective switching end-effector.

3.1.3. Contact area: Membrane actuation

This concept is similar to the previous concept, as bi-stable membranes reduce the contact area to either pick up or release the targeted laminate. Laminate pick-up is achieved through interlayer adhesion, and release is done through actuating the membrane to minimize the contact area and by pushing away rigid laminates. Actuation is bi-directional allowing for large displacement which is not dependent on the thermal properties of the membrane and/or laminate [24].
Bi-stable membranes are very energy efficient and reliable. In previous studies, switching is done electrostatically [25–27], electromagnetically [28], thermally [29], or by exciting the device in resonance [30]. In figure 3.5 the ground states are altered with electrical pulses. The displacement of such a membrane is quantified by the following equation.

$$w_0 = \frac{\sqrt{35}}{4} t_m \sqrt{\sigma_0 \frac{1}{\frac{4}{3}\frac{t^2}{R^2}\frac{E}{1-\nu^2}}} \tag{3.2}$$

With w_0 is the initial displacement, t_m is the membrane thickness, R the radius of the membrane, E the Young's modulus and ν is the Poisson ratio of the used material. The initial stress is indicated by σ_0 and must be larger than zero to generate a non-zero value underneath the square root. The minimum value of the initial stress is the critical stress (σ_c) and is quantified with the following equation.

$$\sigma_c = \frac{-4}{3}\frac{t^2}{R^2}\frac{E}{1-\nu^2} \tag{3.3}$$

Figure 3.5: Actuation of a bi-stable membrane to its two states. The edges of the membranes are mounted and thus apply a reaction force unto the membrane [31]. (a) Membrane state during laminate release. (b) Membrane state during laminate pick-up.

3.1.4. Pressure differential: Temperature induced

The concept in figure 3.6 utilizes the thermal expansion of air to create a vacuum. The vacuum is created by contacting the laminate with a pre-heated hollow end-effector and allowing it to cool down. As the temperature within the micro hole reduces, the trapped air is contracting, resulting in a vacuum. Due to the relative low pressure in the hole, a force is created which allows for pick-up of the targeted laminates. Laminate release is achieved by increasing the end-effector temperature.

The end-effector can be heated with several methods, e.g. laser beam, micro heater. However, heating and cooling of the end-effector requires time and must be done uniformly to ensure a uniform force distribution.

The force created with this method is determined with equation (3.4).

$$P_s = P_t(1 - \frac{T_t'}{T_t}) \tag{3.4}$$

Here P_s is the suction pressure generated, S is the contact area of the micro hole, P_t is the atmospheric pressure, T_t is the temperature before contact in Kelvin and T_t' is the temperature after contact in Kelvin. Equation (3.4) indicates that the pressure created is limited by the service temperature of the target laminates. In the case of TPU the service temperature (353 °K [32]) limits the created pressure differential to 17.2 kPa.

The final force of the end-effector depends on the coverage area of the micro holes. A sufficiently large coverage is required to overcome gravity and the interaction forces. The force created requires excellent sealing performance between the end-effector and laminate to achieve the pressurization and to maintain it over time.

Temperature changes also result in stress between the laminate and the end-effector. For example, if the gold plated end-effector is pick-and-placing a TPU laminate (size: 20 µmx1010 cm), the corresponding thermal stress is 42 kPa ($\Delta T = 80° K$). This stress is well below the yield stress of TPU 45 MPa [33]. Thermal stresses need to be considered with this concept, but do not form any large complications at the set laminate dimensions.
The thermal stress is determined by running a FEM analysis [34] with the following coefficients of thermal expansion (CTE): Silicon - $2-3.2\times10^{-6}$ Strain/°K [32], TPU - of $1.6-1.65\times10^{-4}$ Strain/°K.

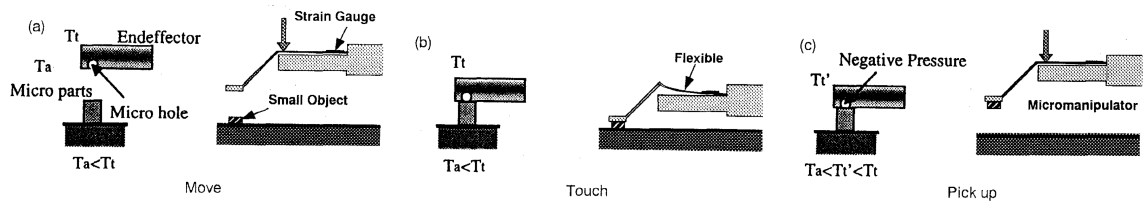

Figure 3.6: Micro manipulator pick-and-place process as a result of induced temperature changes. [35] (a) Heated end-effector contacts object. (b) Temperature reduces, contracting the air and creating a vacuum in hole. (c) Vacuum is used to pick-up object.

3.1.5. Pressure differential: Speed induced

The speed induced end-effector utilizes an elastomeric stamp which is manipulated swiftly to alter the adhesion strength [36, 37], see figure 3.7. By pushing the stamp onto the laminate, the stamp collapses, increasing its contact area. The stamp is then retracted rapidly, resulting in a pressure difference creating a large force. Due to the elastomeric nature of the stamp, the collapsed state is reversed, reducing the interaction force between end-effector and laminate. Subsequently, the laminate is released onto the build plate due to the reduced interaction forces. This system results in an end-effector with reversible generalized adhesion with ratios higher than 1000. The distributed load achievable is 100 kPa, which is remarkably high compared to the previous concepts [36].

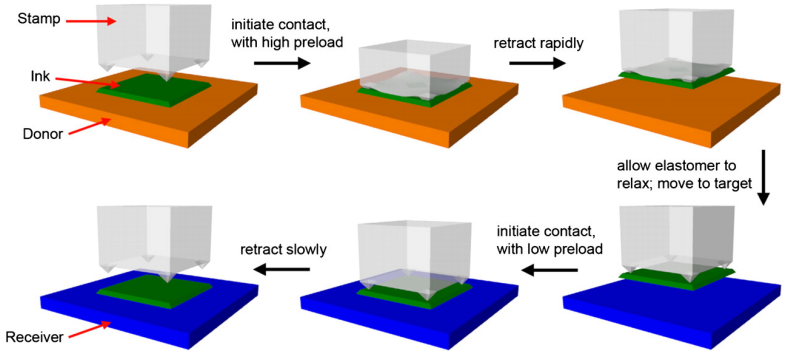

Figure 3.7: Schematic image of the pick-and-place process utilizing a stamp to create a speed induced pressure differential [36].

3.1.6. Pressure differential: Membrane induced

In figure 3.8 a bio-inspired octopus vacuum gripper is shown. The idea is similar to the temperature induced concept (section 3.1.4), but the pressure differences in the holes/suction cups are controlled by a vacuum pump. In the top chamber of the end-effector, a vacuum is created. This vacuum pulls up the membranes, operating an array of suction cups. The actuation of these membranes creates a pressure difference between

the end-effector and the laminate, resulting in an attraction force grasping the laminate. However, as seen in the temperature induced concept, sealing performance is crucial to achieve and maintain the pressurization of the chamber.
The presence of membranes on the suction cups is to ensure all holes are covered to maintain the induced pressure applied on the end-effector. This feature is significant as it allows for the pickup of complex shaped laminates, while maintaining the induced pressure applied upon the suction cups.

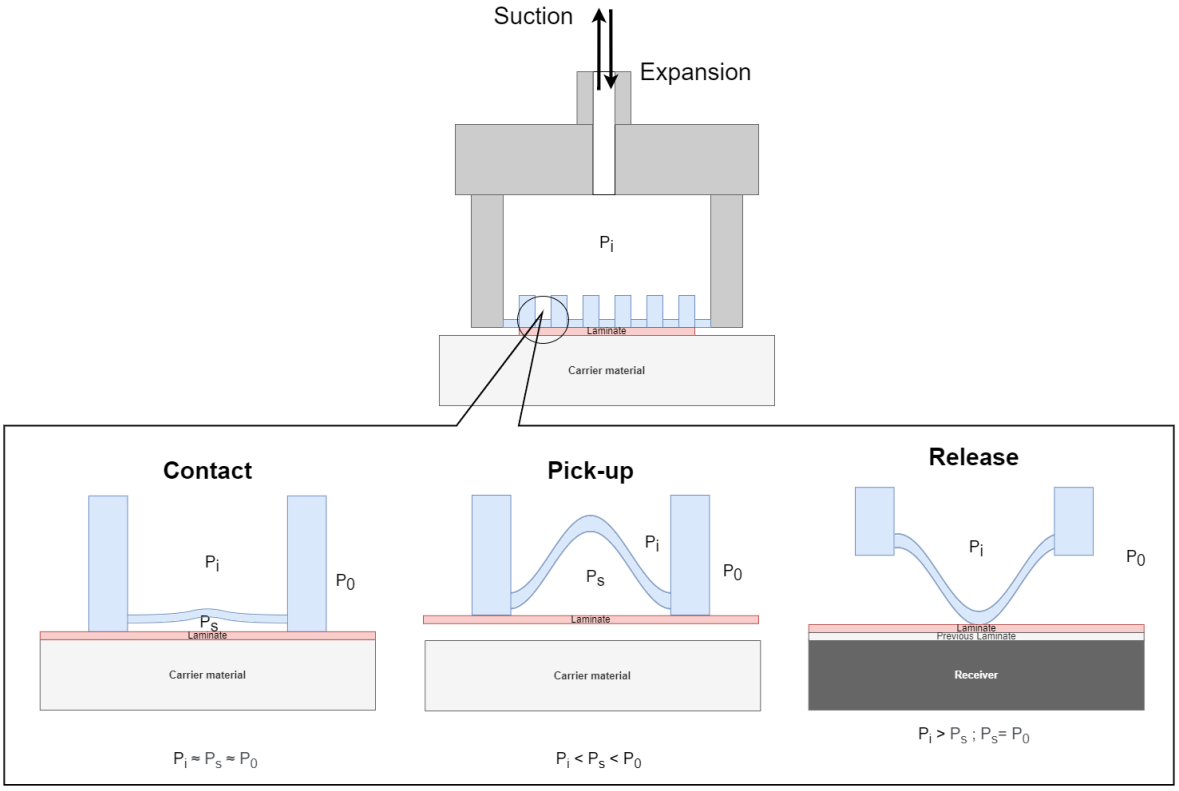

Figure 3.8: Schematic drawing of the membrane induced concept with the three different stages in which it operates. [38].

The membranes can be used bi-directionally, to create a large switching force. During laminate pick-up the membranes are deformed to create a suction force and during laminate release the expanding membrane ejects the laminate upon the build plate. Due to the large range of switching force that can be created, a large variety of laminates can be pick-and-placed.

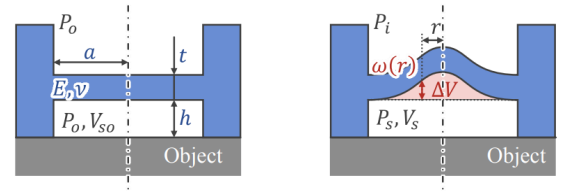

Figure 3.9: Theoretical model of a singular suction cup within the membrane induced end-effector.

The theoretical model of the concept is visualized in figure 3.9. The corresponding forces created by this concept are defined with the following equations.

$$\Delta V = \int_0^{\omega_{max}} \omega(r), dz \tag{3.5}$$

Where the pressure differential ΔV is a function of the deflection of the membrane ω and its diameter r. The suction pressure is determined by using Boyles-Charle's Law, leading to equation (3.6), assuming that the suction pressure (P_s) and the induced pressure (P_i) remain constant.

$$P_s = \frac{16 E t_m^3 h}{(1-\nu^2) a^4} \tag{3.6}$$

With the variables E, t_m, ν are Young's modulus, thickness of membrane and Poisson's ratio, respectively. Here P_s is the suction pressure generated and h is the initial height difference between the laminate and the membrane. The derivative of this equation is described in the appendix equation (E.5) [39].

The equations show that the suction pressure can be tuned through multiple variables, resulting in a large range of suction pressures to correspond with the various laminates.

3.2. Concept selection

In this section, the various concepts are assessed based on a set of concept criteria, see appendix C.1. The concept selection is qualitative, and done by assessing the concepts in a table with positive and negative signs. The table is utilized to highlight the individual features of the concepts to finally select the most promising concept. The limitations and benefits of the concepts are seen in table 3.1. The three vital criteria of the table are: material diversity, geometric capability and delicate handling. Further argumentation of the selection procedure is found in appendix C.

	Contact area: Peeling	**Contact area: Expanding membrane**	**Contact area: Membrane actuation**	**Pressure differential: Temperature induced**	**Pressure differential: Speed induced**	**Pressure differential: Membrane induced**
Material diversity	+	- -	+ -	+ -	+ +	+ +
Geometric capability	+ +	+ -	+	+ -	-	+ -
Delicacy	- -	+ +	+	+	- -	+ +
Throughput	+ +	+ +	+	-	+ +	+
Force generation	+	+	-	+ -	+ +	+

Table 3.1: Qualitative selection table with the various concepts and criteria.

Based on the qualitative assessment, the most promising concept is the membrane induced pressure differential, see table 3.1. This is mainly because of its geometric capability, delicacy and bi-directional force application.

The end-effector is very compatible for a large variation of materials, as the peak force is not material dependent. The force is achieved by membrane deflection, which is initiated by the induced pressure within the end-effector. By using membranes, the induced pressure (P_s) remains constant as any pressure drops within the end-effector itself are mitigated. This way, the suction cups can be actuated consistently, allowing for handling of geometrically complex laminates.

The force created by the end-effector can be varied effortlessly by altering the induced pressure. The induced pressure can also be larger than the atmospheric pressure, thus expanding the membrane and deceasing the layer interaction forces and allowing for delicate release of the laminate. Thus, the concept creates a large suction force and can release laminates delicately.
The most vital drawback of the concept is the required sealing performance. Insufficient sealing performance impedes the generation of a pressure differential and thus limits the force generation. This problem is countered by using a very flexible PDMS membrane, which deforms easily, sealing any defect between the end-effector and the laminate. Additionally, any minor imperfections left preventing a perfect seal has little influence on the initial pressure. Therefore, the force is sufficient to overcome the interaction force. Additionally, laminate placing is achieved rapidly, therefore the initial force does not need to be maintained over a long period of time.

The membrane induced concept has one additional feature, which is its capability to pick-and-place 3D laminates. If required, the end-effector can be designed flexible, to achieve proper adhesion regardless of the topography of the sheets. This feature is not further used in the design process, but the concept does provide more freedom in the shape of the laminates.

Based on its geometric capability, delicacy and bi-directional force application, the choice is made to further pursue the membrane induced octopus concept.

4. Modelling mechanical behavior

This chapter analyses the mechanical properties of the suction cups within the octopus concept with a numerical model. The numerical model shows the mechanical behavior of the membrane and is used to optimize the suction pressure. In figure 4.1 the simulation strategy is shown. The four design variables (a, h, t_m, E), and the operating variable (P_i), have a direct impact on the suction pressure (P_s). The suction pressure impacts the deformation (ω) and the stress (σ_y) in the membrane and laminate. The deformation is used to predict membrane movement and influences the suction pressure, and the stresses are used as a boundary condition to mitigate material failure.

The next sections analyze the impact of the four design variables and the induced pressure (P_i) on the suction pressure (P_s), deformation (ω) and max stress (σ_y). At the end of the chapter, the concept is modified based on the numerical findings. The influence of the contact area (p), is analyzed in chapter 5, as it is independent of the performance variables and is determined by the production method. The code of the applied numerical model is represented in appendix I and is verified by experiments conducted in chapter 6.

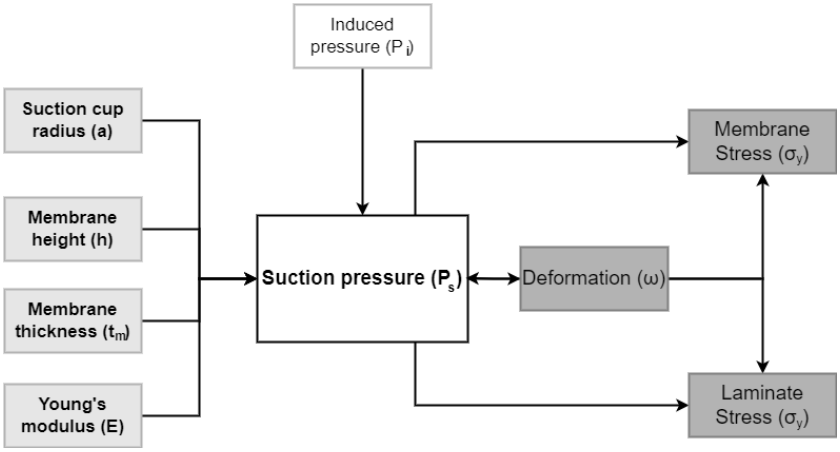

Figure 4.1: Simulation structure. Performance variable: Suction pressure, Operating variable: Induced pressure, Design variables: light gray boxes, Boundary condition: membrane/laminate stress, Dependent: Deformation

Before diving into the various numerical results, there are general conditions that are applied to the numerical model. The first condition is to apply the end-effector in a non-controlled environment. This means that the surrounding pressure is the atmospheric pressure and that variations in humidity must be considered. Thus, at normal office conditions with a relative humidity of $40-60\%$ the system must remain operational [40]. This goal is to ensure the robustness of the design and to decrease cost, since ensuring a controlled climate is costly.

Lastly, all numerical results are for the case that laminates are picked up of a surface with negligible interaction forces. Such surface can be achieved with a special coating and/or by applying a precise surface roughness. The numerical results for laminate release are very similar to pick-up and are shown in appendix F. For the membrane it is preferable to choose a material which is hydrophobic, has a low modulus of elasticity and has a great yield strength ensuring membrane integrity [38, 39, 41]. A material that meets these preferred features is PDMS, which is commonly used for delicate manipulation. These material properties are used throughout the numerical analyses [8]. Depending on the materials available for the membrane and the production method of the end-effector, the dimensions and materials are determined, see chapter 5.

Variable	Symbol	Variable type
Atmospheric pressure	P_0	Control
Induced pressure by vacuum pump	P_i	Operational variable
Radius of suction cups	a	Independent/Design
Initial height of sealing space (Initial volume)	h (V_0)	Independent/Design
Membrane thickness	t_m	Independent/Design
Modulus of elasticity of membrane	E	Independent/Design
Contact area (wall thickness of studs around suction cup)	p	Independent/Design
Suction pressure	P_s	Performance variable
Deformation	ω	Dependent variable
Max stress	$\sigma_{y_{max}}$	Boundary condition

Table 4.1: Overview of the main variables of one suction cup.

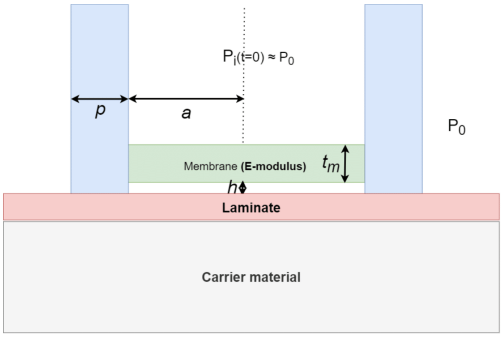

Figure 4.2: An indication of the independent design variables.

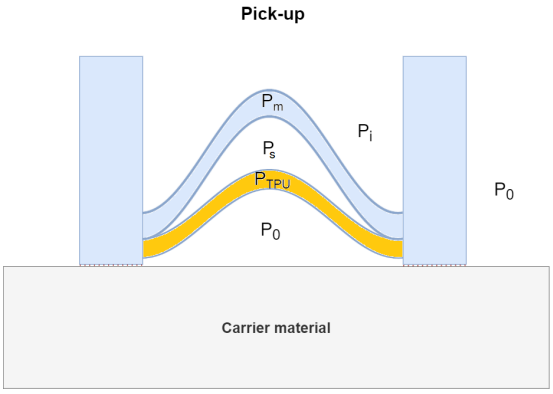

Figure 4.3: Pressure distribution in a suction cup during pick-up of a TPU laminate (flexible laminate). The pressure underneath the laminate is the atmospheric pressure (P_0) due to the surface roughness of the carrier surface. ($Pi < Ps < P0$)

4.1. Suction pressure (P_s)

4.1.1. Pressure equations

The suction cup membrane experiences various pressure distributions during pick-up, which are initiated by the induced pressure (P_i). The membrane absorbs an amount of energy, which is dependent on the volume change. In the case of a singular suction cup with an infinitely stiff laminate, the energy balance is constructed as follows.

$$P_i \Delta V = P_m \Delta V + P_s \Delta V \tag{4.1}$$

Where P_i is the induced pressure, P_m is the pressure drop as a result of the membrane and P_s is the suction pressure as a result of the pressure distribution. The equation shows that the induced pressure (P_i) is directly correlated to the suction pressure (P_s) as a result of the pressure drop.
The suction pressure is defined in equation (4.2) and depends on the induced pressure, membrane thickness (t_m), the initial height (h) and the radius of the suction cup (a). The derivation of this equation can be seen in appendix E.

$$P_s = \frac{P_i}{2} + \frac{\sqrt{\left(P_i + \frac{16\,\mathrm{E}\,h\,t_m^3}{a^4\left(\nu^2-1\right)}\right)^2 - \frac{64\,\mathrm{E}\,P_0\,h\,t_m^3}{a^4\left(\nu^2-1\right)}}}{2} + \frac{8\,\mathrm{E}\,h\,t_m^3}{a^4\left(\nu^2-1\right)} \tag{4.2}$$

The corresponding force is defined by equation (4.3), where F_s is the suction force created by a singular suction cup and P_0 is the atmospheric pressure (101.3 kPa [42]). The formula indicates that a small value for P_s is favorable, as this results in a larger pressure differential relative to the atmosphere pressure and thus creates a larger force.

$$F_s = (P_0 - P_s) * a^2 * \pi \tag{4.3}$$

Equation (4.2) is valid under the condition of a perfectly rigid laminate [39]. For flexible laminates, the deformation results in a pressure drop, resulting in a pressure distribution as seen in figure 4.3. Due to the deformation of the laminate, the volume between the laminate and membrane is altered, and thus, equation (4.2) only indicates the pressure at start ($t = 0$), as the laminate has not yet deformed. At that moment, the membrane and laminate experience peak stress due to the momentarily large pressure variation. Therefore, the value is significant to test the robustness of the membrane and to determine its relation to the other design variables.
For the final deformation of the membrane and laminate the converging pressure must be used, thus the pressure at $P_s(t = \infty)$ must be determined. This is done using Boyle's law, as shown in equation (4.5). The change in volume is directly dependent on the deformation and pressure, therefore the system of equations can be iteratively solved to find the converging solution. This solution is the equilibrium position and determines the final deformation.

$$\begin{gathered} P_s(t=0) * \Delta V(t=0) = C \\ P_0 * V_0 = P_s(t=\infty) * \Delta V(t=\infty) = C \end{gathered} \tag{4.4}$$

$$\Delta V(P_s) \propto \omega(P_s) \tag{4.5}$$

In the case of a laminate with a low modulus of elasticity or very thin thickness, the deformation increases. Due to the much larger deformation of the laminate, the initial volume (V_0) between the laminate and the membrane increases minimally ($V_0 \approx \Delta V(t = \infty)$). Due to Boyle's law, a near constant volume results in a near zero change in suction pressure, and thus remains close to the atmospheric pressure. This results in a minimal force created, impeding successful laminate transportation. Thus, a laminate which deforms easily, results in a smaller change in volume and therefore a minimal pressure differential is created, limiting the force generated by the end-effector. A clear example is the deformation of a TPU laminate seen in section 4.5 figure 4.10.

4.1.2. Variable relations

Radius of suction cups (a)
The radius of the suction cup has an enormous influence on the created suction pressure. In figure 4.4a it can be seen that the suction pressure depends strongly on this variable. The model indicates that a smaller radius converges to the atmospheric pressure ($P_0 \approx 101$ kPa) and thus a smaller pressure differential is present. It is favorable to choose a sufficiently large radius in the converged region ($P_i \approx P_s$) to maximize the pressure differential. The radius at which this drop occurs can be altered with the other design variables. Additionally, it can be seen that the suction pressure converges to the induced pressure. This trend can also be seen when looking at the limit of the equation (4.2) if a is set to infinity.

Initial height of sealing space (h)
The change in membrane height (initial volume) is detrimental for the force created upon the laminates. The initial volume impacts the mechanical behavior of the membrane and the target laminates. The initial volume is dependent on the suction cup height ($V_0 = h * \pi * a^2$).

In figure 4.4b it can be seen that the suction pressure (P_s) converges to the atmospheric pressure when increasing the suction cup height. This is the effect of a relatively small volume change, compared to the increased initial volume, resulting in a near zero pressure change, see equation (4.6). Thus, a minimal initial volume results in a larger pressure differential. Therefore, the smaller the suction height, the larger the force acting upon the laminate.

$$P_i V_0 = P_s(V_0 + \Delta V) \text{if } \Delta V << V_0; P_s \approx P_0 \tag{4.6}$$

Membrane thickness (t_m)
The membrane thickness influences the amount of pressure created in the suction cup due to the change in energy it absorbs, see equation (4.1). Therefore, in figure 4.4c it can be seen that with a thicker membrane, the suction pressure converges to atmospheric pressure. The nature of this curve indicates that minimizing the membrane thickness is favorable for the creation of a large suction pressure. However, smaller membrane thicknesses results in larger stresses.

Modulus of elasticity (E)
The curve of figure 4.4d converges to the atmospheric pressure. This is as a stronger membrane does absorb more energy and therefore reducing the pressure differential. With an infinitely large Young's modulus, no deformation would occur, and thus no suction pressure is achieved.

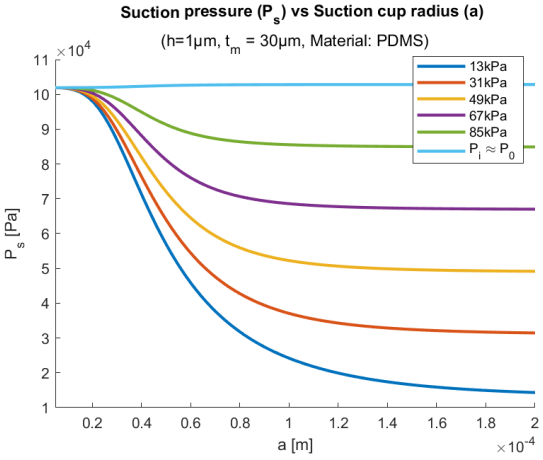

(a) Suction pressure (P_s) vs Suction cup radius (a).

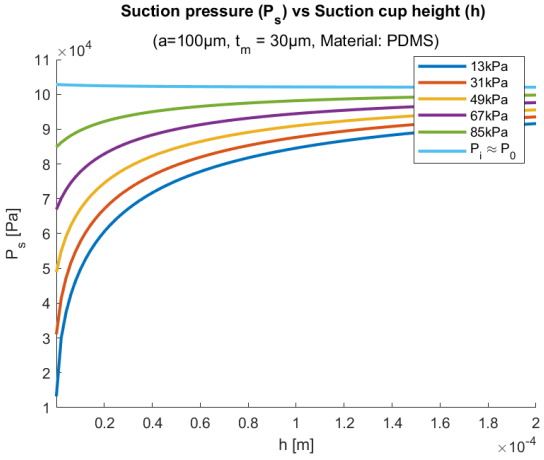

(b) Suction pressure (P_s) vs Suction cup height (h).

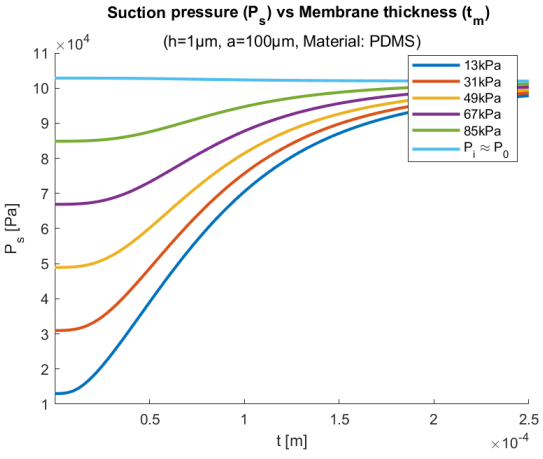

(c) Suction pressure (P_s) vs membrane thickness (t_m).

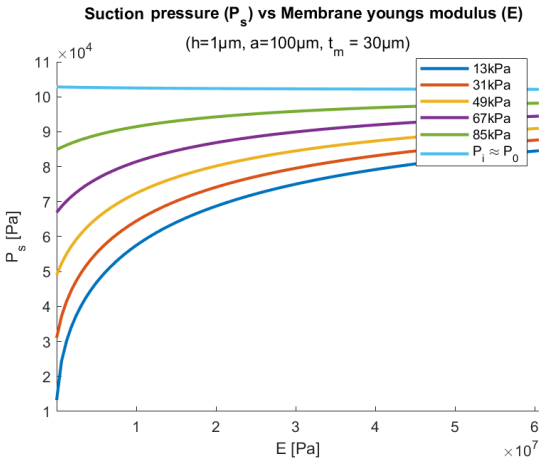

(d) Suction pressure (P_s) vs Modulus of elasticity (E).

Figure 4.4: Indication of the influence of the independent design variables on the suction pressure. The variating lines are various induced pressures applied. Atmospheric pressure: $P_0 \approx 101\,\text{kPa}$

4.2. Deformation (ω)

4.2.1. Deformation equation

Deformation of the membrane is modeled with equation (4.7) [38, 39]. Within this equation, it can be seen that the pressure difference acting upon a sheet is crucial to determine sheet deformation, as stated in equation (4.7).

$$\omega = \frac{\pi\left(1-\nu^2\right)\left(P_s - P_i\right)\left(a^2 - r\left(k\right)^2\right)^2}{16\,\mathrm{E}\,t_{mat}^3} \tag{4.7}$$

Where v is the Poisson factor, P_i is the induced pressure acting onto the surface, P_s is the suction pressure as defined in equation (4.2), $r(k)$ is the cross-section of the suction cup, a is the radius, E is the Young's modulus and t_{mat} is the thickness of the deformed material, which is the thickness of either the membrane or the laminate in question.

The deformations in a suction cup must be seen as a sequential event. The pressure induced on the membrane results in a suction pressure upon the laminate, as depicted in figure 4.3. As stated in section 4.1, the converging pressure is used to estimate the final deformation.

4.2.2. Variable relations

Radius of suction cups

Membrane deflection differs for various radii and has a characteristic deformation curve. In figure 4.5a the cross section of a PDMS membrane is shown, where it is seen that the maximum deformation occurs at the center of each suction cup. Furthermore, the change in pressure has a linear effect on the maximum deformation, and the slopes at which this is reached differs depending on the induced pressure.
The max deformation increases rapidly when increasing the radius. This is due to its significant influence on the suction pressure and deformation, see equation (4.2) and equation (4.7).

Initial height of sealing space

Increasing the initial height reduces the membrane deformation exponentially. This is due to the reduction in created suction pressure, as a result of the increase in initial volume, see figure 4.4b.

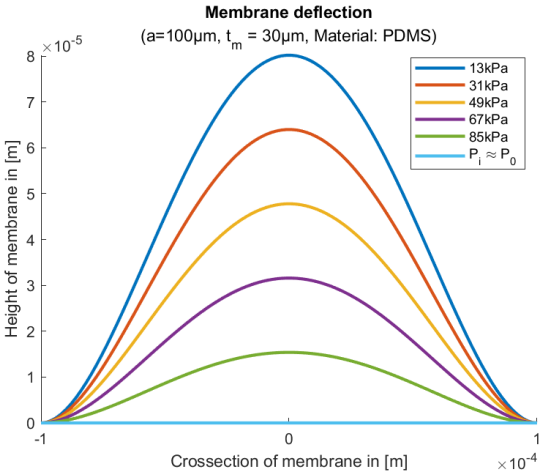

(a) PDMS membrane cross-section of deflection.

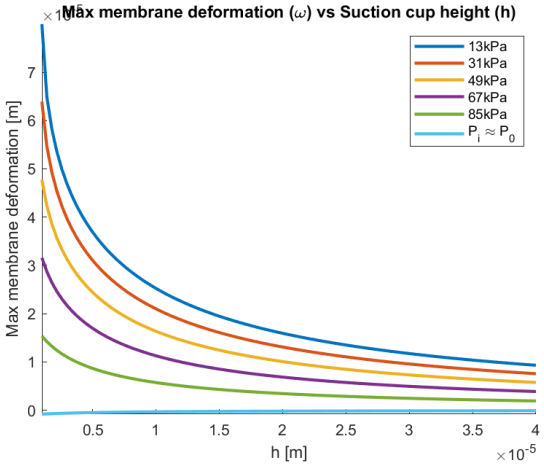

(b) Max deformation (ω) vs Suction cup height (h).

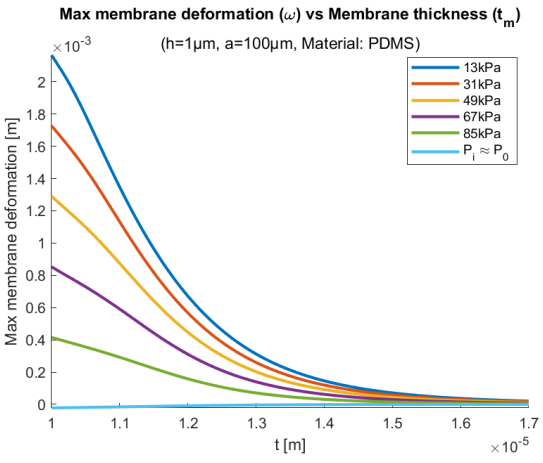

(c) Max deformation (ω) vs membrane thickness (t_m).

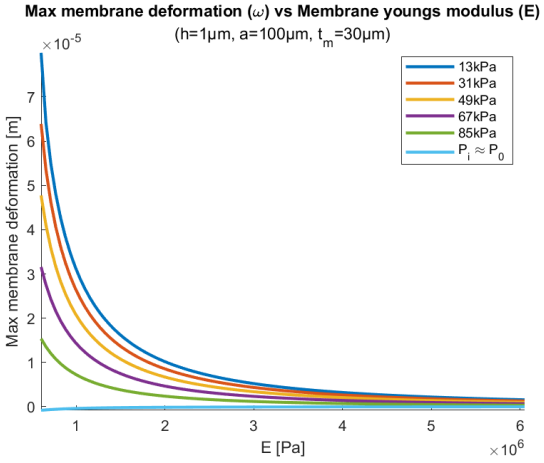

(d) Max deformation (ω) vs Modulus of elasticity (E).

Figure 4.5: Indication of the influence of the independent design variables on the yield stress. The variating lines are various induced pressures applied. Atmospheric pressure: $P_0 \approx 101\,\text{kPa}$[42]

Membrane thickness
Figure 4.5c indicates that increasing the thickness reduces the deformation exponentially. This is due to the reduction in suction pressure figure 4.4c and the quadratic influence of the membrane thickness on the deformation, see equation (4.7). Therefore, increasing the thickness rapidly declines the deformation until near zero deformation is achieved.

Modulus of elasticity
Figure 4.5d shows that minimizing the Young's modulus results in more deformation, which is an intuitive result. A membrane with a small Young's modulus absorbs less energy, resulting in a larger pressure differential and an increase in membrane deformation.

4.3. Maximum Stress ($\sigma_{y_{max}}$)

4.3.1. Stress equation

The stress analysis of membranes is generally more complex than beams, as membranes are two-dimensional in nature [43]. In this concept, the membrane is loaded by a uniformly distributed pressure. In the case of a circular membrane which is clamped on the edge, the maximum stress is defined by

$$\sigma_{y_{max}} = \frac{0.75 * P_{material} * a^2}{t_{mat}^2} \tag{4.8}$$

where a is the radius, t_{mat} is the material thickness and $P_{material}$ is the pressure drop over the material. The maximum stress occurs at the edge of the membrane where it is clamped. To insure laminate integrity, the maximum stress must be well below the yield stress.
The maximum stress is an important metric to ensure that the system does not fail. In the following figures, various design variables are changed and their impact on the maximum stress is investigated.

4.3.2. Variable relations

Radius of suction cups
In figure 4.6a it can be seen that increasing the radius results in larger maximum stresses in the laminate. This is a logical consequence, as a larger radius results in an increase in max stress, as seen in equation (4.8). Additionally, as the radius increase the pressure differential grows, therefore initially resulting in an exponential increase in maximum stress.
The membrane, on the other hand, experiences much lower stresses as the pressure differential is based on the induced pressure and the suction pressure. As the suction pressure converges at large radii, figure 4.4a, the pressure differential is reduced, resulting in small stresses. The most stress is experienced by the membrane when it is uncovered. This stress, is then only dependent on the membrane thickness and must not exceed its Young's modulus.

Initial height of sealing space
In figure 4.6b the stresses are graphed against the suction height. Looking at the membrane, a larger initial volume results in an increase in perceived stress, as the membrane perceives a larger pressure differential due to the induced pressure (P_i) and the suction pressure (P_s). Initially, as the volume increases so does the suction pressure and therefore the pressure differential increases resulting in larger stresses.

For the laminate, the inverse curve is visible. This is, as the pressures acting upon it are the atmospheric pressure ($P_0 \approx 101\,\text{kPa}$) and the suction pressure (P_s). Thus, an increase in the initial volume results in an increase in suction pressure and thus a decrease in pressure differential.

Membrane thickness
Equation (4.8) states that a larger membrane thickness reduces the suction pressure, see figure 4.4c, and reduces the stress, see equation (4.8). In figure 4.6c it can be seen that the initial stress is stable, as for small membrane thicknesses the suction pressure is approximately equal to the induced pressure. This is because nearly no energy is stored in the membrane, as stated in section 4.1.2.
Increasing the membrane thickness, decreases the suction pressure and therefore increasing the stress experienced by the membrane. Further, increasing the thickness results in an eventually constant pressure differential, resulting in its peak stress. Thereafter, further increasing the membrane thickness results in an

exponential decrease in maximum stress, see equation (4.8). Both laminate and membrane converge to a near zero maximum stress when increasing the membrane thickness.

Modulus of elasticity

The curves indicating the influence of the modulus of elasticity (figure 4.6b) are visually similar to the curves indicated in figure 4.6b. This is due to their similar impact on the suction pressure when increasing the corresponding value. Increasing the Young's modulus results in a convergence of the suction pressure (figure 4.4d) and therefore resulting in a decrease in pressure differential. A very stiff membrane results therefore in an increase in pressure differential upon the membrane and a decrease in pressure differential upon the laminate, resulting in the graph in figure 4.6d.

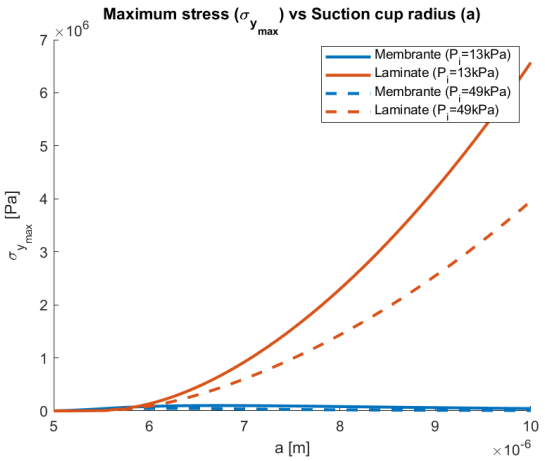

(a) Suction pressure (P_s) vs Suction cup radius (a).

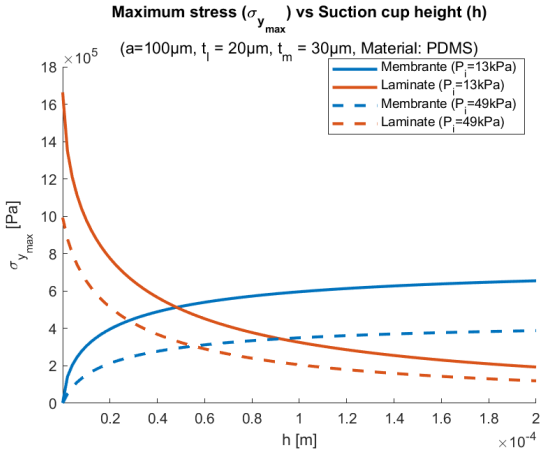

(b) Suction pressure (P_s) vs Suction cup height (h).

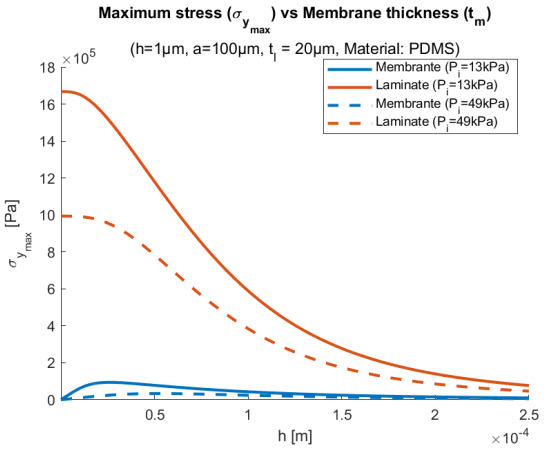

(c) Suction pressure (P_s) vs membrane thickness (t_m).

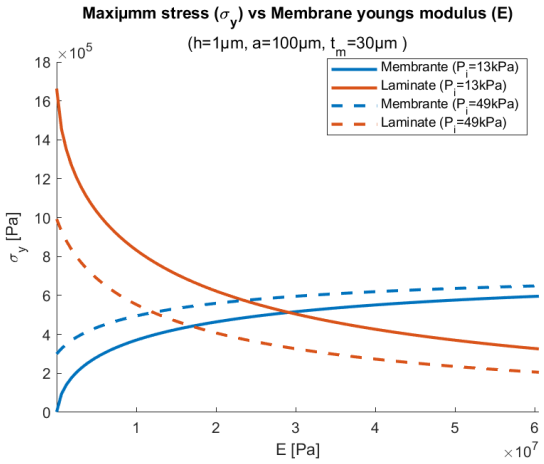

(d) Suction pressure (P_s) vs Modulus of elasticity (E).

Figure 4.6: Indication of the influence of the independent design variables on the yield stress. The variating lines are various induced pressures applied. Atmospheric pressure: $P_0 \approx 101\,\text{kPa}$

4.4. Design trade offs

In the previous three sections, certain theoretical trends became apparent, such as the maximization of the radius. However, in reality, there are certain limitations that need to be considered for all variables.

Radius of suction cups

The radius of the suction cups is a very influential variable of this concept. These numerical results indicate that a maximization of the radius results in the convergence of the pressure differentials acting upon the laminates. The maximum pressure differential achieved is then $P_0 - P_i$, thus decreasing the induced pressure further also increases the pressure differential upon the membrane.
However, increasing the pressure differential results in the exponential rise of the stresses, which must remain

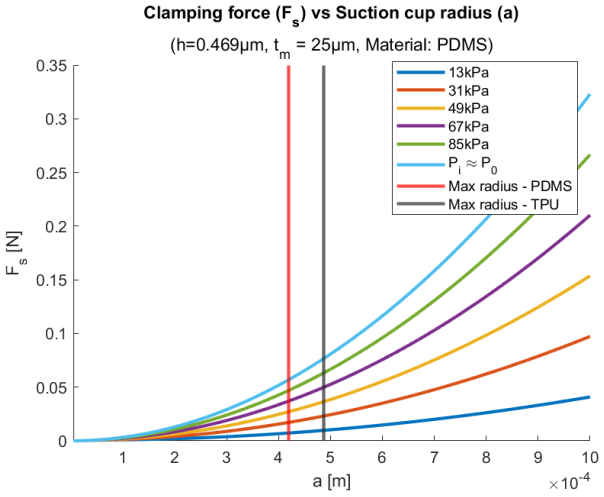

Figure 4.7: Force created per suction cup. The vertical lines indicate the maximum radius until yield stress is reached.

below the yield stress of both membrane and laminate, as seen in figure 4.7. In this case, the membrane is the limiting factor, reducing the stress can be achieved by increasing the membrane thickness, larger Young's modulus and/or by increasing the applied induced pressure. The maximum radius can be limited by the TPU yield stress, thus limiting the laminate thickness and/or maximum radius size.

Additionally, large suction cups restrict the end-effector to apply a uniform force for geometrically complex laminates, as large suction cups have a higher chance to not achieve a complete seal.
As an example figure 4.8 is constructed. This figure shows that the larger suction cups realizes full coverage once and cannot support the smaller features of the star shaped laminate. Additionally, large suction cups restrict the end-effector to apply a uniform force for geometrically complex laminates, as large suction cups have a higher chance to not achieve a complete seal. Meanwhile, the smaller suction cups make contact more often and thus supports the intricate shape better. Thus resulting in a more uniform load and in total a larger force. Thus, for a more uniform force distribution and compatibility with intricate geometrical shapes, smaller suction cup radius are preferable. In conclusion, a balance must be found between the pressure force and geometric compatibility while remaining below the yield stress of the materials.

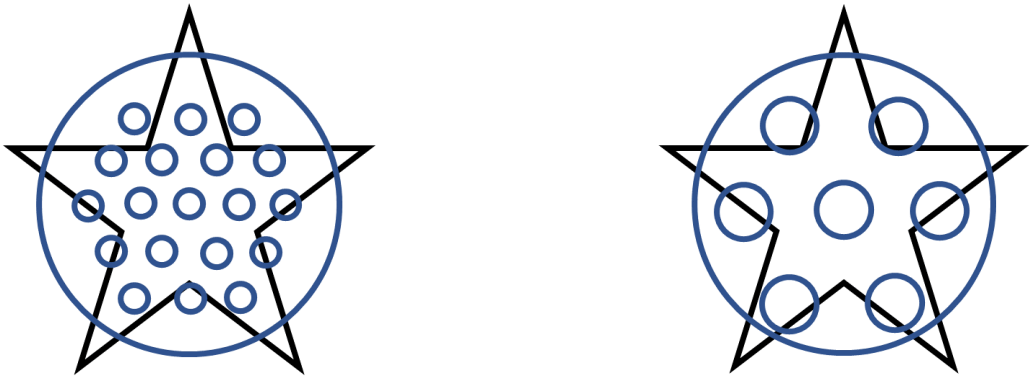

Figure 4.8: Example of the tradeoff in the radius size of the suction cups. The total area covered by the suction cups remains equal in both images.

Initial height of sealing space

The initial suction cup height can be minimized to a certain extent, as starting with no initial volume would result in stiction, thus impeding the suction pressure created. Therefore, the choice is made to minimize the pre-deflection according to the capillary condense distance at a relative extreme humidity of 99.9%. This distance is defined with equation (B.2). This results in equation (4.9).

$$h_{min} = d_{cap_{max}} \approx \frac{2\gamma(T = 20\,°\text{C})\nu_{water}\cos(\theta_{membrane})}{RT\log(H_r)} \tag{4.9}$$

With h_min being the minimum mean distance, $d_{cap_{max}}$ the maximum distance over which capillary forces have effect, γ is the surface tension of water (at 20 °C: 72.75×10^{-3} N/m) [44], ν is the liquid molar volume of water (18 ml/mol) [45], R is the gas constant (8.314 $JK^{-1}mol^{-1}$) [46], T is the absolute temperature in Kelvin and H_r is the relative humidity.

Membrane thickness & Modulus of elasticity
Both the membrane thickness and material are ideally as small as possible to achieve the maximum suction pressure. However, reducing these values results in larger stresses and deformation, which could result in failure of either material. Therefore, the yield stress of these materials must be considered to mitigate end-effector failure.
Furthermore, there are production limitations to achieve membranes which are very thin and elastic. Such membranes are very hard to acquire, and therefore the focus is put on the thinnest membrane available, as the thickness impacts the suction pressure more than the yield stress, see equation (4.2).

4.5. Concept simplification

A change in suction cup height results in a change in the initial volume, see equation (4.6) . However, this dimension is crucial and needs to be exact and is the smallest feature size of the concept. This complicates the production of the design. Therefore, the choice is made to create the initial height by inducing a pressure before contacting the laminate for pick-up, see figure 4.9. Thus, at contact, the membrane is already deformed and its volume is equal to the volume created by the height offset of the suction cups.

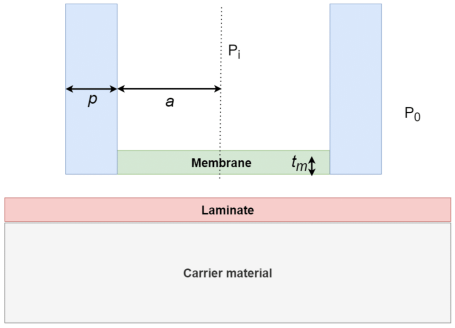

(a) Simplified end-effector concept, as h is set to zero.

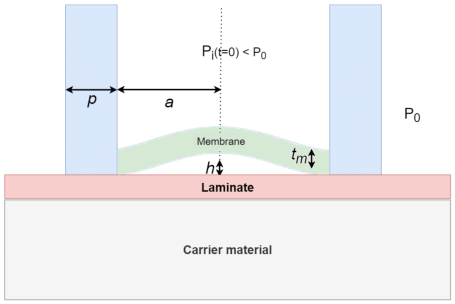

(b) Pre-deflection applied moments before contact. Pressure below membrane is now equal to P_0 and decreases as the induced pressure decreases.

Figure 4.9: Indication of the independent design variables with the applied concept simplification. In this case, an initial pressure is required within the suction cup ($P_i < P_0$).

With this design simplification, the physical suction cup height is reduced to zero during production, which simplifies production significantly. As no complicated overhang structures must be made to create the suction cup and application of the membrane can be done directly unto a surface. Additionally, this method does not limit the mean height distance of the membrane, enlarging the design freedom. The initial volume is defined by equation (4.11).

$$\int_0^{\omega_{max}} \pi * r^2(w_{V_0}, P_i)\, d\omega_{V_0} = \pi a^2 h = V_0 \tag{4.10}$$

$$r(\omega_{V_0}, P_i) = \sqrt{\sqrt{\frac{\omega_{V_0} 16 E t^3}{\pi(1-\nu^2)(P_0 - P_i)}} + a^2} \tag{4.11}$$

$$\omega_{max} = \frac{\pi\left(1-\nu^2\right)(P_0 - P_i)\, a^4}{16\, E\, t^3} \tag{4.12}$$

The integral indicates that the volume caused by the deformation must be equal to the volume achieved by the suction cup height, the algebraic solution of the integral is written in appendix E.1.1. Solving this integral

numerically results in the induced pressure to create the desired initial volume. The corresponding deflection is seen in figure 4.10a. An additional benefit is that there is no need to blow up the membrane to push away the laminate, as normalizing the pressure back to atmospheric pressure results in the same effect due to pre-suction of the membrane.

This concept simplification has a few drawbacks which must be considered. As the minimal induced pressure is limited, the pressure required for the pre-deflection limits the pressure variations induced upon the membrane. Furthermore, as the membrane is pre-deformed before contact, an initial stress is already present. Therefore, at minimum induced pressure, the pressure variation experienced by the membrane is larger, which results in larger experienced maximum stresses. Both effects can be reduced by minimizing the initial volume and/or increasing the membrane thickness. Final dimensions are determined in next chapter.

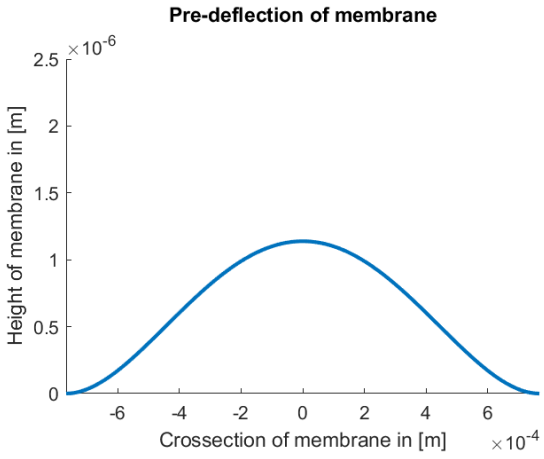

(a) Initial deflection with an initial induced pressure of $P_i \approx 94\,\text{kPa}$.

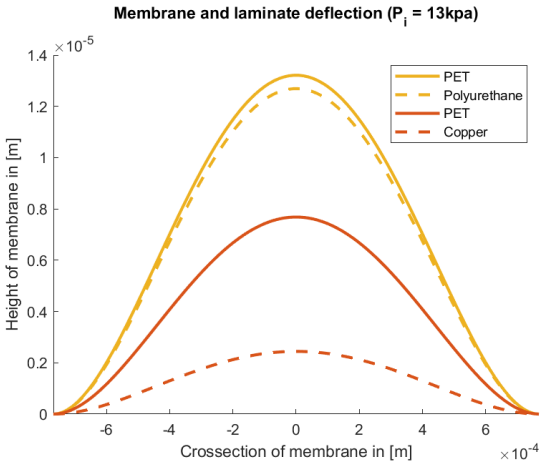

(b) Membrane and laminate deflection at laminate pick-up ($P_i = 13\,\text{kPa}$).

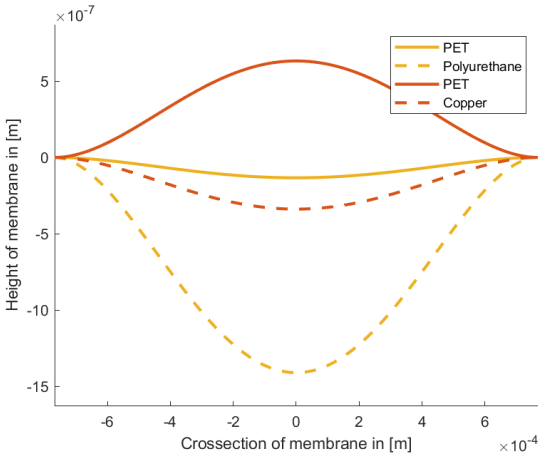

(c) Membrane and laminate deflection at laminate release ($P_i = P_0$).

Figure 4.10: Membrane and laminate deflection initiated based on the induced pressure after pre-deflection, with $a = 50\,\mu\text{m}$, $t_m = 30\,\mu\text{m}$, $P_i = 13\,\text{kPa}$ and with a PET membrane 3M 8991 of table 5.1. Volume under curve is equal to the surface achieved with $h = 0.469\,\mu\text{m}$, $V_0 = 2\pi h\,\mu\text{m}$.

In the numerical model, the difference between a rigid (Copper) and a flexible (TPU) laminate is clear, see figure 4.10. For the final deformation of the membrane and laminate, the converging suction pressure must be determined ($P_s(t = \infty)$). This is done using Boyle's law, as shown earlier in equation (4.5). Based on the numerical convergence results, the final suction pressure during pick-up of the respective laminates are: Copper - 64.7 kPa ($\Delta P = 37.2\,\text{kPa}$) , TPU - 101 295 Pa ($\Delta P = 4.8\,\text{Pa}$). These values clearly indicate that the pressure differential decreases over time and that a more rigid laminate can create much larger suction forces. The suction force on the TPU is minimal and is theoretically just enough to achieve laminate pick-up. The same trend can be seen during release of the laminates: Copper - 107.1 kPa ($\Delta P = 5.1\,\text{kPa}$) , TPU - 101 300.5 Pa ($\Delta P = 0.5\,\text{Pa}$).

5. Production & Dimensioning

In this chapter, the production of the end-effector is described. After explanation of the chosen production method of the complete end-effector, the corresponding material choice is made. Based on these final materials, the end-effector is dimensionalised and produced.

5.1. End-effector production

In the following subsections, the end-effector production method is explained based on the concept simplification indicated in section 4.5. This concept alteration simplifies production as the smallest feature size of the end-effector is mitigated. The final end-effector consists of nine parts with the four main parts being: membrane, membrane scaffold, the vacuum casing and the carrier surface. The assembly of the end-effector can be seen in figure 5.1. The carrier surface is the substrate of which laminates are picked-up. The membrane is relatively thin and is directly attached to the membrane scaffold. The final dimensions of the end-effector can be found in table 5.2 and appendix G.

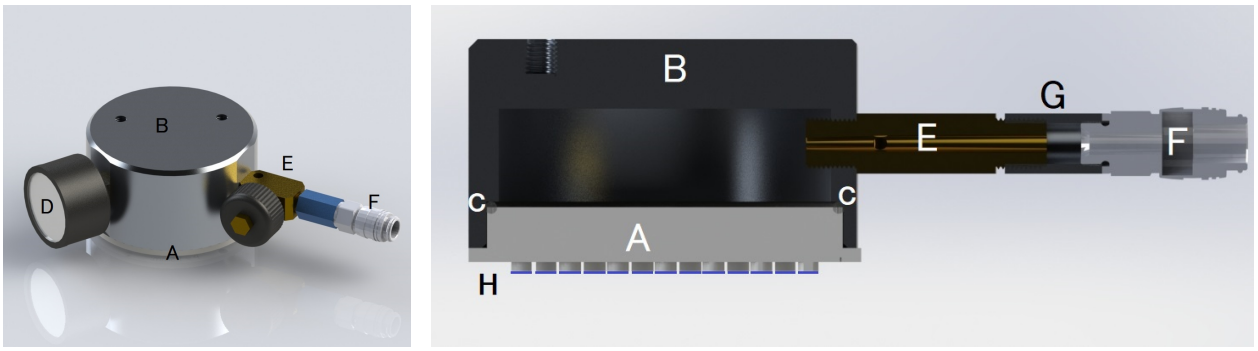

(a) Isometric view of only the end-effector.

(b) Cross-section of the end-effector.

Figure 5.1: End-effector design. Part A: Membrane scaffold; Part B: Vacuum casing; Part C: O-rings; Part D: Pressure Gauge; Part E: Pressure release valve; Part F: Quick connect coupling; Part G: Aluminum coupling; Part H: Membrane (Blue line which is directly attached to the membrane scaffold).

5.1.1. Membrane

The membrane is the most vital part of the end-effector. In the previous chapters, the model has been made with a PDMS membrane, as it is an excellent material for this application due to its high hydrophobicity and

Figure 5.2: Final production sample of the end-effector.

low modulus of elasticity. However, acquiring this material and applying this in production is a very complex endeavor, due to the fact the PDMS membrane must be cured, have a uniform height and must be adhered to the membrane scaffold. As the goal of this thesis is to create a proof of concept, the choice is made to use prefabricated tapes as membranes. These tapes can be adhered to the scaffold, allowing for consistent and simple fabrication. To ensure that only the suction cups are covered, the tape is cut to size with a hollow punch. The tapes utilized are shown in table 5.1. These tapes are far from ideal, as they have a larger modulus of elasticity, are less hydrophobic and have a pre-determined thickness. The increase in the modulus of elasticity means that the membrane is less ductile, which impedes the contact interface between the membrane and the laminate. This can result in leaking suction cups, thus nullifying the suction force generated. Additionally, the lower contact angle means that the material is less hydrophobic and thus capillary forces will be effective over a larger distance, see section 2.2. An increase in thickness is not devastating; however, it does limit the applicable design parameters. Therefore, the thickness will be compensated for by optimizing the radius and minimizing the initial volume.

Specification	**H-old 12.SL** [47]	**3M 8991** [48]
Backing type	PET	PET
Adhesive type	Silicone	Silicone
Total thickness	80 µm	61 µm
Backing thickness	50 µm	25 µm
Total measured thickness	≈ 85 µm	≈ 50 µm
Width	50 mm	50 mm
Tensile strength	87.5 MPa	83.3 MPa
Young's modulus PET	3.7 GPa [49]	
Young's modulus Silicon	4.5 MPa [50]	
Yield stress	138 MPa [49]	
Poisson ratio	0.48 [49]	
Contact angle	78.9° ± 0.14° [51]	

Table 5.1: Overview of material properties of the membrane. Membrane thickness is measured, and the results are seen in appendix H.2.

5.1.2. Membrane scaffold

The membrane scaffold is fabricated using digital light processing printing (DLP) on a Prusa SL1 resin printer. Each sample is cleaned thoroughly to ensure no debris created by the supporting structure of the DLP printer is present. In figure 5.3 the design of the membrane scaffold is seen. In the center of each suction cup, a hole is present, over which the membrane is attached. The membrane is attached in three steps. First, the membrane scaffold is cleaned to remove any support material impeding the final shape. Second, the membrane is attached by applying pressure through a flat surface. Third, the membrane is cut to shape using a hollow punch, creating the image seen in figure 5.3b.
The end-effector is designed such that the scaffolds are interchangeable. The interchangeability of the scaffold is very helpful to simplify the troubleshooting process and allows for variating scaffold samples to validate the measurements. When printing the membrane scaffold, its orientation is vital to ensure a smooth surface finish of the suction cup. Additionally, it must be as flat as possible to ensure proper contact with the target laminate. This is necessary to create an air tight seal between the laminate and the membrane to ensure laminate pick-up.

The vacuum casing is pressurized, which deforms the membrane, creating the desired suction pressure. On the side of the top surface of each membrane scaffold, text is added to distinguish the variations of the created scaffolds. The five countersunk holes on the side mounts the scaffold to the vacuum casing and ensures a proper seal during operation of the end-effector.

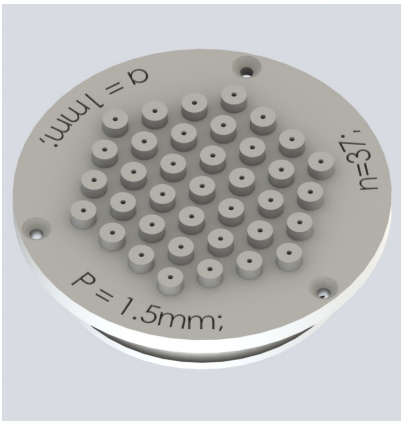

(a) Membrane scaffold CAD design. Suction cup diameter: 1 mm

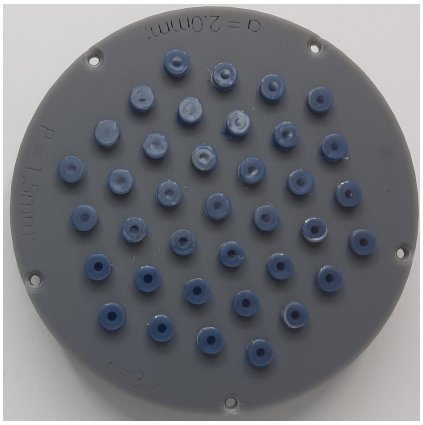

(b) Membrane scaffold produced sample. The blue layer is the PET membrane (3m 8991). Suction cup diameter: 2 mm

Figure 5.3: Top view of membrane scaffolds. Suction cup amount: 37; wall thickness: 1.5 mm,

5.1.3. Vacuum casing

The vacuum casing is the interface which brings the membrane, membrane scaffold and vacuum pump together. The casing is made of aluminum, allowing for a singular casing which is compatible with a multitude of membrane scaffolds. The casing has three interfaces which correspond to four different parts.

The first and main interface is with the membrane scaffold. The membrane scaffold is attached to the vacuum casing with five countersunk m2 screws and an O-ring. The O-ring has an internal diameter of 72.7 mm and a width of 2.62 mm. The O-ring is compressed 0.7 mm in the casing by the five mounting screws to ensure a good seal according to the specifications provided by Eriks sealing technology [52]. A chamfer is added to the interface to allow for smooth insertion of the membrane scaffold.

The second interface is with the vacuum pump. The vacuum casing is connected to the vacuum pump with a quick connect coupling, which allows for simple attachment and detachment while maintaining the induced pressure. This quick connect coupling is attached to a pressure release valve. The pressure release valve is added to the vacuum casing to control the pressure of the system. Additionally, the valve allows for controlled pressurization, allowing for experiments of the end-effector at specific pressure's.

Lastly, a pressure gauge is added to monitor the induced pressure during measurements. The pressure gauge is crucial to pressurize the membrane precisely and to have values which can be inserted into the numerical model. The quick connect coupling and pressure gauge are attached to the vacuum casing with threads according to the BSPP standard (British standard piper parallel). The complete casing is produced by milling and turning stock aluminum. The blueprint of which can be found in appendix G.1.

All interfaces are checked for leaks by attaching a sealed membrane scaffold. Thus, the various interfaces can be tested of over an extended period of time to ensure that the system remains pressurized. The experiments conducted showed a pressure change of 30 kPa after 72 hours. Therefore, the assumption can be safely made that the pressure within the vacuum casing remains constant during the experiments performed in chapter 6.

5.1.4. Carrier surface

Each laminate that is picked up must be detached from the carrier surface. The carrier surface is dependent on the laminate creation method, but a certain surface quality is required to urge laminate pick-up. The surface quality is crucial as it must minimize the forces with the laminate to ensure an upward resultant force allowing for the transportation of the laminate. The two main forces that must be prevented are: minimization of the interaction forces and vacuum prevention between the carrier surface and the laminate. Both forces can be mitigated by adding a surface roughness to the carrier surface. The carrier material is milled out of aluminum and thereafter polished to ensure the desired surface roughness is achieved.

Minimization of the interaction forces is mainly achieved by increasing the roughness until it exceeds the capillary adhesion distance, as capillary adhesion is the largest of the three interaction forces as stated in section 2.2. Thus, for minimization of the capillary interaction force, the surface roughness must be larger

than the capillary distance of the material, resulting in the following condition.

$$d_{cap} << R_a \tag{5.1}$$

The capillary condensation distance for aluminum, copper and TPU is calculated to find the maximum required surface roughness of the carrier material. The maximum capillary distance is dependent on the contact angle, which are respectively, 97°, 86° and 99.5° for Aluminum, [53], Copper [54] and TPU [55]. Therefore, the maximum capillary condensation distance is achieved for TPU, which results in the following equation.

$$d_{cap_{max}} \approx \frac{2\gamma(T = 20\,°\text{C})v_{water}\cos(\theta_{TPU})}{RT\log(H_r)} = 0.41\,\mu\text{m} \tag{5.2}$$

Thus, a surface roughness significantly larger than 0.41 µm impedes the capillary interaction forces.

To mitigate the creation of vacuum between the laminate and the carrier surface, a surface roughness larger than 0.3 µm would suffice [56]. Thus, a surface roughness of $R_a = 3.2\,\mu$m is more than sufficient. This surface roughness is chosen as it is the industry standard commercial finishing grade of milling surfaces [57].

5.2. Design variable values

As seen in table 4.1 there are 5 independent variables. In this chapter, the various variables are determined based on the final material choice made. The final values are seen in table 5.2.

5.2.1. Minimum induced pressure

The minimum induced pressure is determined by the pump. The vacuum pump used is a 350 W SPS pump capable of reaching a minimum pressure of 13 kPa.

5.2.2. Initial height/volume

As stated in section 4.4, this value must be minimized for maximum suction pressure. Minimization is only limited by the capillary distance between the laminate and the membrane. This distance is determined to be at 0.469 µm at an extreme relative humidity of 99.9% according to equation (4.9). Thus, applying this distance as the mean distance of the pre-deformed state should ensure minimal stiction within the opening of the suction cups. The corresponding initial volume is then dependent on the radius, as stated in equation (4.12).

5.2.3. Membrane thickness and material

The membrane thickness is a variable which is predetermined by material availability. As stated before, the preferred material is PDMS; however, the material is very hard to come by. Therefore, the choice is made to release this ambition and search for a membrane with a thickness of approximately 30 µm, has a minimal surface roughness and has an adhesive backing. This resulted in either Teflon or PET tapes. Due to manufacturing problems at 3M with Teflon tapes, only PET tapes were available. Within the PET tapes, the choice is made for the membranes stated in table 5.1. Both membranes consist of PET backing and with a silicon adhesive, and thus the membranes are a composite material. Even though the materials of the membranes are known, the final Young's modulus is not. Therefore, the rule of mixture is applied to estimate the Young's modulus of the composite membrane [58].

$$E_c = fE_{PET} + (1 - f)E_{SI} \tag{5.3}$$

$$f = \frac{h_{PET}}{h_{PET} + h_{SI}} \tag{5.4}$$

Using equation (5.4) results in an estimate Young's modulus for the 3M 8991 tape at 1.531 GPa (t= 61 µm) and 2.332 GPa (t= 80 µm) for the H-old 12.SL. These estimations are then tested by putting both membranes in a tensile tester to precisely determine the Young's modulus. These tests are done three times per membrane and the mean value is selected. The measurement results are seen in figure 5.4, additional data is seen in appendix H.1.

With these measurements, the young's modulus can be determined by looking at the linear region and applying equation (5.5).

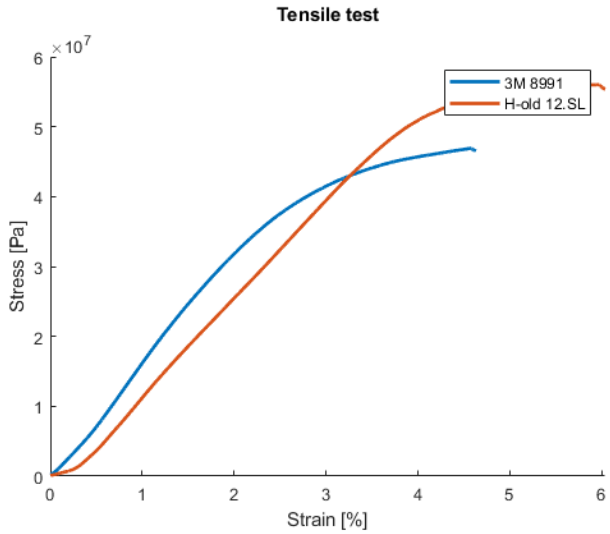

Figure 5.4: Tensile test measurements of the two means. Samples are pieces of membrane attached to the tensile tester, each with a width of 50 mm.

$$E = \frac{\sigma}{\epsilon} = \frac{\frac{F}{A}}{\epsilon} \tag{5.5}$$

Where σ is the stress, ϵ is the strain, F is the force exerted and A is the cross-section of the sample. With the data in figure 5.4 and the measurements on the thickness of the membranes, the Young's modulus is accurately determined. Based on these measurements, the Young's modulus of the tapes are:

- 3M 8991 - 1.28 GPa
- H-old 12.SL - 1.34 GPa

These results do not differ much from the estimations, as the Young's modulus of both PET and silicon have a wide range. This results in the differences seen between the estimated values and the values from the experiments.

Finally, the choice is made to design the system using the 3m 8991 tape because of its thinner membrane and lower modulus of elongation. This results in lower forces required, which allows for smaller suction cup radii, resulting in more design freedom, and reduces the initial pressure required to achieve the initially desired mean height.

5.2.4. Wall thickness of suction cup

As stated in section 4.1, the clamping pressure must overcome the interaction force and gravity. Thus, to ensure laminate pick-up, the following system of equations must hold, as seen in chapter 2.

$$F_G + F_{CL} + F_E \geq 0 \tag{5.6}$$
$$F_G = A * t * \rho * g \tag{5.7}$$
$$F_{CL} = F_{Ca} + F_{vdW} + F_{Cs} \tag{5.8}$$
$$F_E = P_s(t = \infty) * a^2 * \pi * N \tag{5.9}$$

The interaction forces are dependent on the surface roughness, surface material and the surface area with which they interact. The contact area with the end-effector is determined by the wall thickness of the suction cup (p). The wall thickness impacts the amount of suction cups, as a large side wall reduces the amount of suction cups that can be placed. The walls cannot be non-zero as a surface is required to attach the membrane as stated in section 5.1.1.

As the carrier material has large surface roughness, the interaction forces with this surface are reduced enormously. Therefore, for pick-up, the largest force that needs to be overcome is gravity.

Variable	Symbol	Value
Minimum induced vacuum	P_i	13 kPa
Initial mean height	h	0.469 µm
Young's module membrane	E_m	1.28 GPa
Membrane thickness	t	25 µm
Wall thickness of suction cup	p	∞
Radius	a	0.7 µm

Table 5.2: Dimensions of the end-effector variables.

Theoretically, an end-effector with complete flat surfaces increases the interaction forces created by the end-effector and thus increasing the base force it can create. This increases, its compatibility for very thin materials with a very low modulus of elasticity as the forces created by the suction cups decreases for very ductile materials as stated in section 4.2. When laminate deposition is required, gravity and the inter laminate interaction force would result in releases. The suction cups itself would add a small switchable force generation to ensure pick-up and release.

For thicker laminates (<100 µm) with a large modulus of elasticity, the suction pressure becomes much more dominant. So dominant in fact that the interaction forces are nearly negligible, as stated in section 4.2. This allows for enough force to be created to ensure pick-up and release. Thus, the thickness of the walls does not impede its performance negatively for these laminates.

Therefore, the choice is made to choose for a completely flat surface for the pick-up of micro laminates. For thicker laminates with large modulus of elasticity, the wall thickness is close to irrelevant. These findings are also experimentally validated in chapter 7.

5.2.5. Radius

As stated in figure 4.4a, increasing the radius results in a theoretical larger pressure differential. However, increasing the radius limits the delicacy and geometric complexity of the laminates that are picked-up. Therefore, the choice is made to minimize the radius to push the boundaries of the system and to achieve the most uniform force distribution. Minimizing the radius is limited by production limitations, and the corresponding radius is 0.7 mm. This radius is chosen based on the accuracy of the DLP printer, which has a resolution of 100 microns in X/Y and has a minimum layer height of 25 µm. In table 5.2 the final dimensions of the membrane scaffold are shown.

6. Experiment methods

The numerical model results shown in chapter 4 are an estimation of the reality and need to be validated. In this chapter, the experimental approach and the corresponding test-setups are depicted. The results of these experiments are then compared to the numerical results to assess the prototype performance based on the numerical model. The results are depicted and discussed in chapter 7.

6.1. Experiments

Three main experiments are conducted. The first experiment focuses on the deformation of the membrane at different induced pressures. The second experiment focuses on the amount of force created by the suction cups when using a rigid laminate. In the third experiment, various laminates are pick-and-placed. This experiment validates the entire application of the end-effector. All experiments validate a certain aspect of the numerical model, in the following paragraphs the methods of these experiments are elaborated.

6.1.1. Experiment 1: Deformation

The deformation experiment is prepared by first placing the membrane onto the membrane scaffold and pressurizing the vacuum casing. The pressurized case is then decoupled from the vacuum pump and placed on its back under the Keyence VHX6000 microscope [59]. Under the microscope, the 3D measurement capability of the VHX6000 is utilized to measure the deformation of the membrane, which is done for three random suction cups. Gravity has negligible influence on this experiment.

The deformation of each of the three random suction cups is measured at four pressures: $P_0 (\approx 101\,\text{kPa}), 70\,\text{kPa}, 40\,\text{kPa}$ and 13 kPa. These pressures are obtained by carefully opening the pressure release valve until the desired pressure is reached. The measurement at $\approx 101\,\text{kPa}$ is the baseline, as this is the pre-deformation at atmospheric pressure. The deformation is measured by taking the average of the two heights at the edges of the suction cups. The measured deformation is subtracted by the deformation present at atmospheric pressure to counter any initial offsets. In the end, every measurement consists of four separate measurements. The first two measurements are done at the opposite edges of each suction cup and the average of its height is determined. The third measurement is done at the center to determine the maximum deformation of the membrane. The fourth measurement is done at the edges and at the center at atmospheric pressure to determine the initial condition with which the deformation is offset by. Thus, in total 48 data points are collected, four pressures at three random suction cups each consisting of four measurements.
The VHX6000 outputs the cross section of the membrane, and thus deformation is manually measured, resulting in errors. Each suction cup radius is measured to consider the production inaccuracies of the DLP printer. The measurement setup is shown in figure 6.1.

6.1.2. Experiment 2: Force generation

The suction force of the end-effector is measured by applying a force upon a rigid surface instead of a fragile laminate. This rigid surface is attached to a sensor, which is then attached to the main plate as seen in figure 6.2. This rigid surface consists of a silicone sheet (1.5 mm thick) attached to a flat glass surface. A silicone surface is chosen to prevent leaks, as it is relatively ductile ($E \approx 5\,\text{MPa}$ [32]) compared to the membrane ($E = 1.56\,\text{GPa}$). Additionally, a pre-load is applied to deform the silicone to further reduce leakage.
For all measurements, the same surface is used to ensure a constant surface interface. The experiment can validate the behavior of the membrane for the application with a rigid laminate. The forces created this way are much larger compared to a flexible laminate, as the silicone surface does not deform significantly, figure 4.4d. As forces are large for rigid laminates, the interaction forces can be neglected.

The force created is measured for various radii to validate the correlation between the suction pressure and the suction cup radius. The radii chosen are: 0.7, 1, 1.3 and 3 mm. These radii are chosen based on the results of the model, as stated in appendix G. Every radius is measured 4 times. To ensure a proper seal, a pre-load of 50 N is applied. After initial clamping, the induced pressure is applied and the change in perceived force

is measured. During these measurements, a Futek sensor is used, which has a precision of 0.05 N and all measurements are directly digitally stored onto a computer.

With the same setup, the correlation between force and time is investigated. As the surface roughness is vital as the model assumes that the interface between the suction cup and laminate is airtight. However, this assumption does not hold in the real world and leaks are probably present. As this occurs, the force created decreases. The rate at which this occurs depends on the sealing performance of the suction cup. During this experiment, the force is measured over time for the various radii.

Figure 6.1: Experiment 1: Setup to visually determine the deformation. The microscope used is a Keyence VHX-6000 [59].

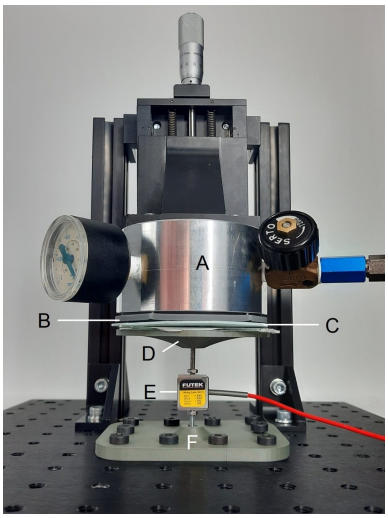

Figure 6.2: Experiment 2: Setup to measure the forces created by the end-effector. Part A: Vacuum casing; Part B: Membrane scaffold; Part C: Silicon surface; Part D: Build plate to sensor mount; Part E: Sensor; Part F: Sensor to laminate mount.

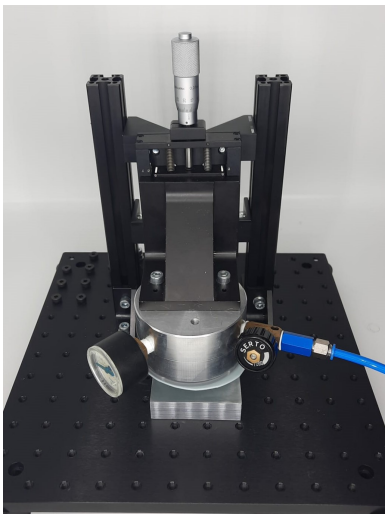

Figure 6.3: Experiment 3: Setup to pick and place laminates. Under the end-effector is a polished aluminum billet for laminate deposition.

6.1.3. Experiment 3: Pick-and-place

The final experiment is the entire application of the end-effector. The setup is built such that a laminate is placed unto the carrier surface, which is then picked-up by the end-effector. Thereafter, the carrier surface is swapped for a polished surface ($R_a < 0.2\,\mu m$) which has a TPU laminate adhered to it. The covered TPU billet is chosen to simulate the placement of a laminate for the creation of a multi-material metamaterial. This experiment is done with a TPU and aluminum laminate due to the limited access to copper laminates. This experiment is done three times for both an aluminum laminate and a TPU laminate. The setup of the experiment is seen in figure 6.3.

7. Results & Discussion

7.1. Experiment 1: Deformation

The measurements performed on the membranes result in images as seen in figure 7.1 created with the VHX 6000 [59]. These images show the cross-section with their corresponding relation to the suction cup. In this image, measurement lines are drawn to indicate various aspects seen in the cross-section. The white line indicates the diameter of the hole and the red line indicates the actual diameter over which the membrane is suspended, see section 7.1.1. At the edge, between the red and the white line, a drop is seen which stagnates at the diameter of the hole (1430 µm). Outside the red line, an increase of approximate 25 µm is measured until the deformation stabilizes.

In figure 7.2 the final, measurements are seen of the maximum membrane deflection at various pressures, considering the pre-deflection at atmospheric pressure. The deflection has a linear correlation to the suction pressure, as seen in equation (4.7). Furthermore, it can be seen that the error is highest at larger pressures, as the deformation is smaller and the present production inaccuracies impact it more.
The deformation results of figure 7.2 do not match the numerical results, as the measurements are far off. This mismatch is mainly caused by production inaccuracies in the membrane scaffold, which can be solved by polishing its surface. In the following two sections, these inaccuracies are further elaborated, followed by the impact of polishing the membrane scaffold.

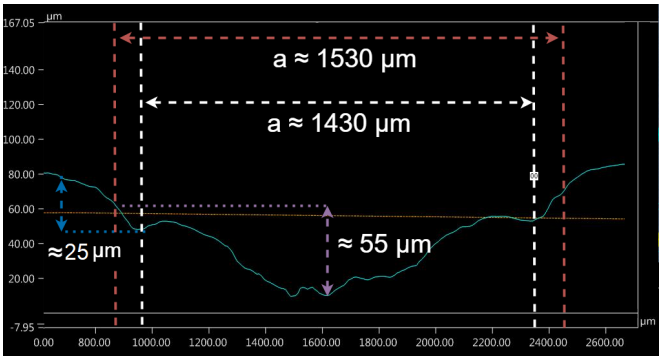

Figure 7.1: Cross sectional image of a suction cup membrane. Membrane: 3M 8991; Design diameter: 1400 µm; Set pressure: 13 kPa; With added markers: White: Actual hole radius; Red: Outer edge radius; Purple: Membrane deflection radius; Blue: Edge drop until hole.

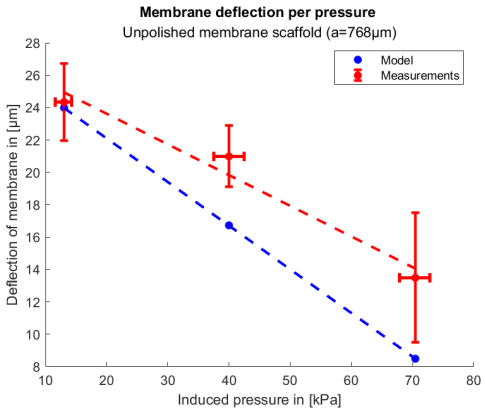

Figure 7.2: Deformation of membrane on raw scaffold at various pressures. Slight inaccuracies in pressure are present due to manual approximation (±3 kPa). Atmospheric pressure: $P_0 \approx 101 kPa$

7.1.1. Production inaccuracies

The inaccuracies of the DLP printer are considered by measuring the radius of the suction cups and applying these values as input in the numerical model to create results similar to the real-world conditions. During the analysis of the suction cups, two vital inaccuracies were detected. First, the radius of the suction cup was larger than designed. In figure 7.3 it can be seen that the inner radius is ≈ 717 µm instead of the designed 700 µm which increases membrane deformation.

The second inaccuracy was found on the edge of the suction cup. In figure 7.4 it can be seen that the DLP printer cannot produce a perfectly straight edge. It instead produces an edge with a fillet with a significant radius. This results in the second outer diameter seen in figure 7.3. This inaccuracy alters the deformation, as the actual radius over which the membrane is suspended is ≈ 770 µm. Additionally, the fillet results in an edge which can adhere to the adhesive layer of the membrane when fully deformed. This results in a drop which then stagnates, see figure 7.1 between the white and red line. At atmospheric pressure, the adherence

of the membrane onto the edge fillet is seen, figure 7.5. At the edges, the height is clearly lower compared to the surrounding surface indicating the adhesion of the membrane to the edge fillet, see the two downward spikes in figure 7.5. Thus, this production inaccuracy impedes the proper deformation of the membrane and impacts these results negatively.

Lastly, a height decline of ≈ 25µm is seen outside the edge in figure 7.1. This is due to the deformation of the silicone adhesion layer, which is much softer (E=4.5 MPa) and is probably compressed during application and/or pressurizing the membrane. The deformation is plastic, as the deformation remains present at atmospheric pressure, see downward slope leading towards the two spikes in figure 7.5.

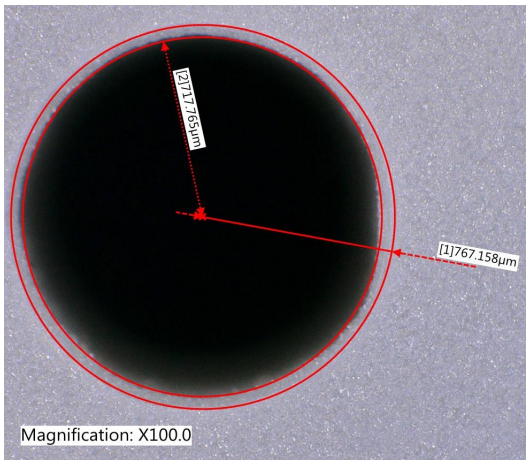

Figure 7.3: Measurements on the DLP printed membrane scaffold hole. The inner red circle indicates the hole radius, the outer red circle indicates the edge radius.

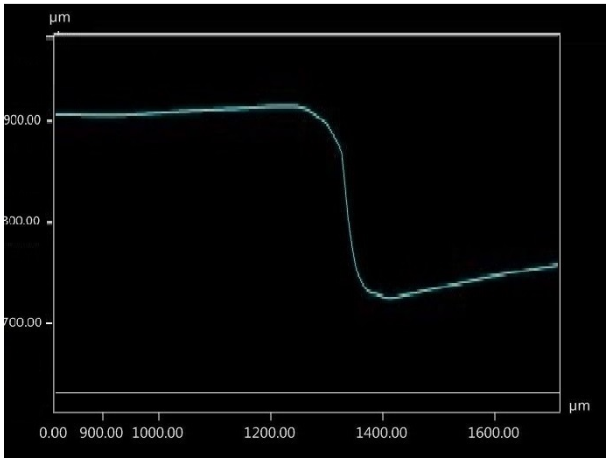

Figure 7.4: Cross section of the membrane scaffold edge. Cross section through the center of the suction cups. Note: depth of hole is inaccurate and irrelevant due to absence of light.

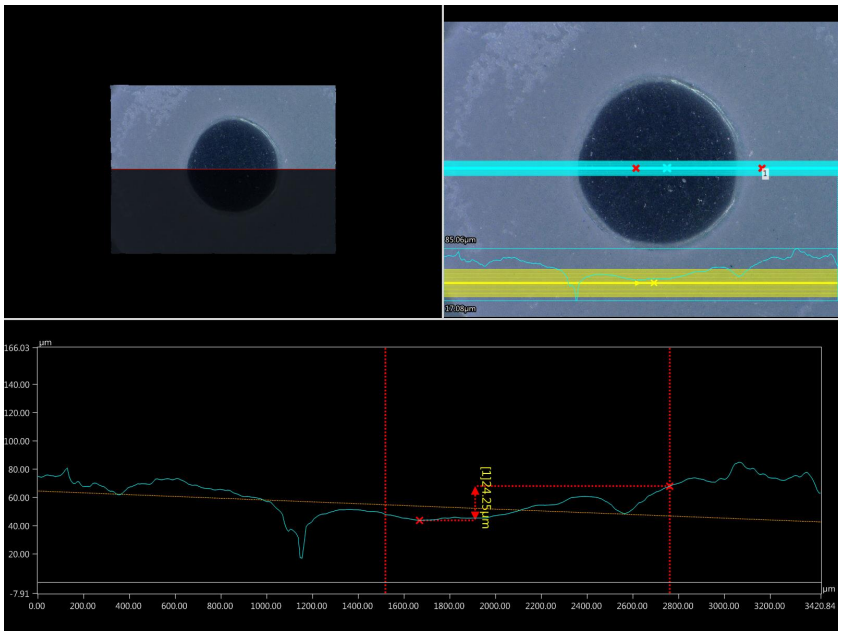

Figure 7.5: Base deformation at atmospheric pressure. Membrane: 3M 8991; Design diameter: 1400 µm; Set pressure: ≈ 101 kPa;

7.1.2. Polishing of membrane scaffold

To counter the inaccuracies caused by the edge, an extra production step is applied. After cleaning the membrane scaffold, the surface is polished to remove the top layer to achieve a more square edge before the membrane is applied.The surface is polished with a 2mu polishing agent, resulting in a slimmer and more square edge, as seen in appendix H.3.1 figure H.5b.

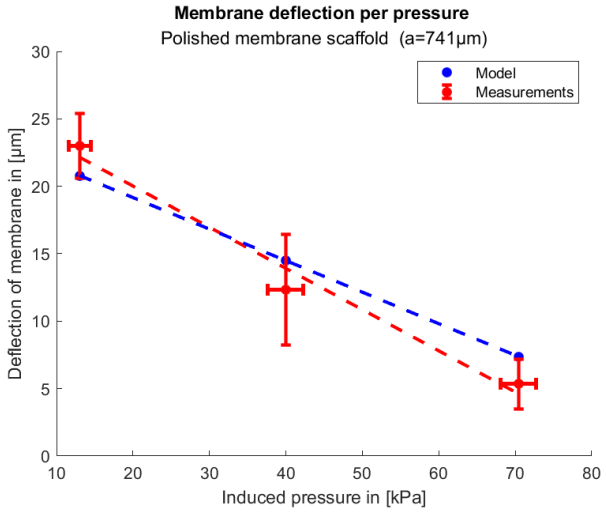

Figure 7.6: Deformation of membrane on polished scaffold at various pressures. Slight inaccuracies in pressure are present due to manual approximation (±3 kPa) Atmospheric pressure: $P_0 \approx 101 kPa$

In figure 7.6, the observed trend line is much closer to the modelled trend line in contrast to the unpolished sample of figure 7.2. These results show that the polished sample resembles the model much better. This is because the polished edge alters deformation less and results in fewer unpredictable errors, improving the results.

In all measurements, relatively large error bars can be seen. The error bars in the measurements consist out of three parts. The most present error are mechanical errors, which are probably the result of inaccuracies in the assembly due to production. The second very influential error is the reading error. Due to the often laborious and repetitive nature of the measurements, reading errors occur, which will result in a large cumulative error. This error has been approximated to about 1.5 µm due to the display accuracy of the VHX 6000 microscope. The third error is due to the machinery itself. The error of the microscope itself is at 0.1 µm [59], which is substantially lower than the other errors.

These results indicate that the model does predict the membrane deformation accurately. However, many parameters impact the deformation negatively, resulting in a large standard error and a large reading error.
The standard error can be countered effectively by improving the production method of the complete assembly. The current production method has two main factors which impact the measurements negatively. Firstly, the usage of a DLP printer results in no precise radii and creates large fillets at the edges. This problem is increased by the adhesive backing of the membrane, adhering the membrane unto the fillet. Secondly, the assembly does not ensure parallelity, and thus the membrane is being measured at an angle under the microscope, impacting the measurements. Using a more precise production technique to produce the membrane solves many issues, as both the radius and the edge would resemble the initial design more. There are many production techniques that can be applied to achieve this, for example micro machining [60, 61], injection molding [62], and two photon polymerization (nanoscribe) [63, 64]. Parallelity can be countered by machining the vacuum casing more accurately. Furthermore, the O-ring compression method can be done at the side of the membrane scaffold, and therefore the mounting pressure does not impede the parallelity. Lastly, an improved manufacturing technique for the membrane scaffold also improves parallelity, as the manual polishing would not be required.
The reading error can be countered effectively by increasing the sample size of the measurements and by using a white light interferometer to measure the depth of each suction cup. The usage of a white light interferometer takes away numerous manual measurements, resulting in smaller errors. Additionally, the time per measurement is decreased drastically, allowing for a much larger sample size.

In conclusion, the deformation experiment shows that the model gives an accurate representation of the deflection of the membrane. The accuracy of the model can be better determined by increasing the sample size of the measurements and applying a more accurate measurement method. Additionally, production limitations result in errors, which impede the deformation of the membrane and thus the perceived model accuracy and precision.

7.2. Experiment 2: Force generation

The force experiments have been applied with a pre-load of 50 N. The force is measured in graphs as seen in figure 7.7, where the peaks indicate the force created by the end-effector when turning on the vacuum pump. The measurement peaks show a slight upward drift, which is probably due to mechanical play within the test setup. With the applied pre-load no significant force change were measured over a substantial period of time (> 5 min). The exact time is not relevant for this research, as the laminate transportation is done in a much shorter time-frame.

The experimental results of the first three radii show a clear resemblance to the numerical model, figure 7.8. An increase in radius resulted in an increase in force. However, discrepancies are apparent, especially at larger radii, which are discussed in section 7.2.2. These discrepancies are due to the following two aspects which need to be considered: the initial volume of the membrane, and the sealing capability of the suction cups. In the following two sections, these aspects are investigated. Additional graphs of the force experiments are shown in appendix H.4.

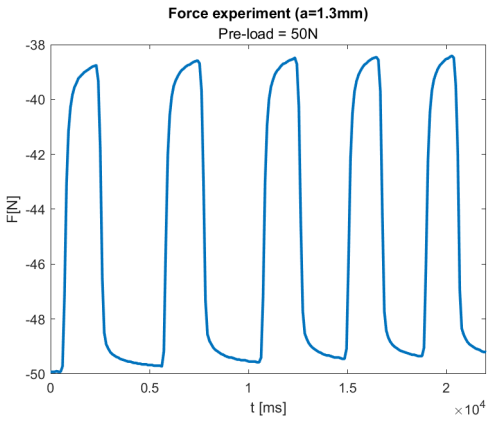

Figure 7.7: Results from the force experiments for $a = 1.3$ mm with a pre-load of 50 N. The spikes indicate the force generated.

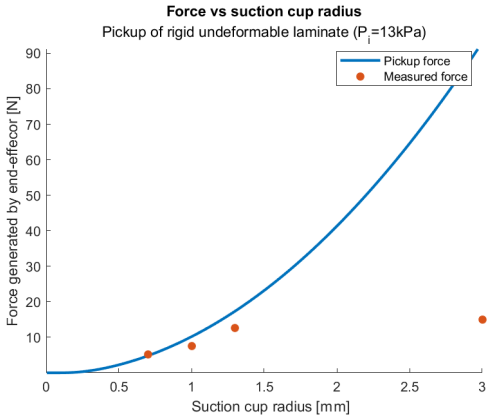

Figure 7.8: Numerical model and experimental results with a pre-load of 50 N.

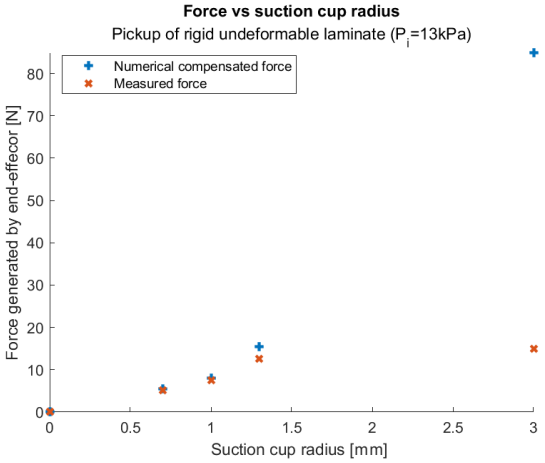

Figure 7.9: Compensated numerical results due to changes in initial volume versus the measured experimental results. The results are compensated by considering the initial volume and radius of the various suction cups.

7.2.1. Initial volume

The initial volume in this experiment is influenced by 1) the initial membrane deflection, and 2) the deformation of the silicon carrier surface, resulting in a change in initial volume. The effects of the change in initial volume is used as input of the numerical model. These results indicate that the experimental values for the radii, 0.7, 1.0 and 1.3 mm are close to the compensated numerical values, see figure 7.9. Additionally, the impact of the change in initial volume is relatively limited, as the values are only slightly below the original

numerical results of figure 7.8. In the following two subsections, the cause and impacts of these aspects are investigated.

Initial membrane deformation

As seen in the previous experiment, it was apparent that the suction cups have an initial deformation and impacts the generated force. Therefore, the initial deformation is measured accurately to determine the mean membrane height of the various suction cups. Additionally, the corresponding radius is measured to consider production inaccuracies. This has been done for four random suction cups for each sample, see figure 7.10 and table 7.1.

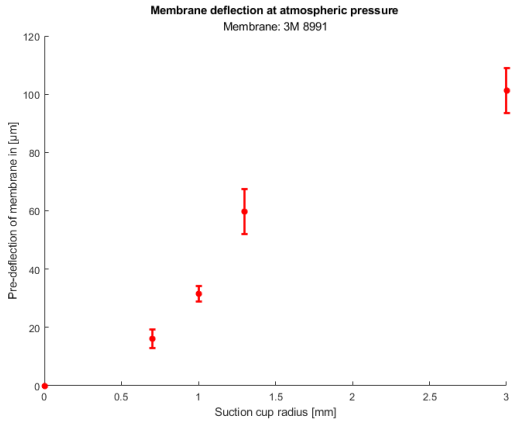

Figure 7.10: Initial deformation of the four samples. Measurements performed with the VHX-600 and the full measurements are in table H.3.

Design radius	**Actual radius**	**Mean pre-deflection** (at P_0))
700 µm	731 µm	8.4 µm
1000 µm	946 µm	16.6 µm
1300 µm	1268 µm	31.6 µm
3000 µm	2897 µm	53.6 µm

Table 7.1: Initial conditions of maximum membrane pre-deflection of different suction cup radii.

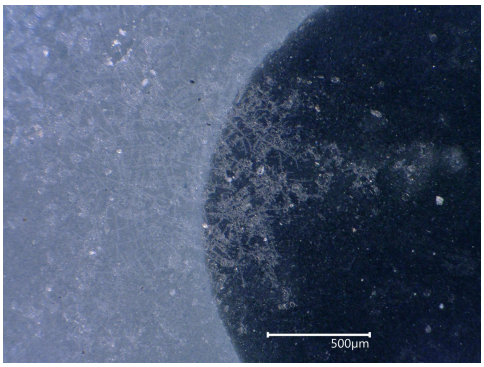

Figure 7.11: Deformation of the adhesive. (a=1.3 mm)

These results indicate an initial exponential relation between the initial maximum deflection and the suction cup radius, which eventually stagnates. The reason for the deformation is twofold.
Firstly, the fillet on the suction cup edge and the adhesive nature of the membrane results in the membrane sticking and therefore having an initial deformation as stated in the first experiment. This problem is countered by polishing the membrane scaffold and/or changing the production method of the membrane scaffold.

Secondly, the adhesive layer appears to deform, resulting in a change in initial deformation. The adhesive backing has a significant lower yield stress than PET (Adhesive: ≈ 2.77 MPa [65]; ≈ PET 138 MPa [49]), resulting in the compression of the adhesive. Additionally, it appears that at larger radius the forces acting upon the radius result in shear stresses which exceed the yield stress of the material resulting in visible alterations underneath the membrane, see figure 7.11. The plastic deformation of the adhesive results in a permanent increase in initial deformation of the membrane. The shear stress increases when increasing the suction cup radius, and can be countered by altering the production method and/or by increasing the suction wall thickness. Therefore, for this production method, a larger wall thickness is preferable to ensure proper adhesion of the membrane.

Thus, the initial deformation which occurs due to the membrane scaffold and the adhesive layer of the membrane result in a reduction of the pressure differential at increasing radii. These effects mainly affect the edges of the suction cups and therefore at larger radii these effects stagnate.

Indentation of carrier surface
The pre-load applied results in the compression of the silicone surface. Thus, the surface over which the membrane is suspended is pushed into the suction cup, decreasing the initial membrane height before the pressurization of the end-effector. The amount of indentation is determined by creating a FEM-simulation [34], as seen in figure 7.12. The resulting indentation of the suction cups are shown in figure 7.13.

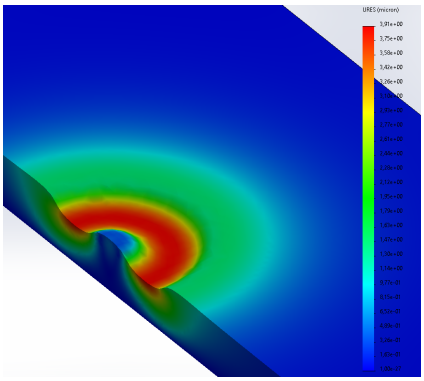

Figure 7.12: Indentation due to the applied pre-load for a=0.7 mm. Total pre-load: 15 N; Per suction cup: 0.41 N. Other FEM results are seen in appendix H.4.3.

Pre-load	**a**=0.7 mm	**a**=1.0 mm	**a**=1.3 mm	**a**=3.0 mm
5 N	1.3 µm	1.1 µm	0.9 µm	0.5 µm
10 N	2.6 µm	2.2 µm	1.8 µm	1.0 µm
15 N	3.9 µm	3.2 µm	2.8 µm	1.5 µm
20 N	5.2 µm	4.3 µm	3.7 µm	2.0 µm
30 N	7.8 µm	6.4 µm	5.5 µm	2.9 µm
45 N	11.7 µm	7.5 µm	6.4 µm	3.4 µm
50 N	13.1 µm	10.8 µm	9.2 µm	4.9 µm

Figure 7.13: Expected deflection due to the various pre-loads.

The amount of silicone indentation alters at various radii, due to the change in area of the suction cup walls. The largest indentation is seen at a radius of 0.7 mm. As the suction cup wall thickness remains constant, the area of the suction cup is smaller. Thus, the distributed load applied upon the silicone surface is increased, resulting in larger indentations. The amount of indentation is subtracted off the mean initial deformation of the membrane to determine the mean initial height/volume.

7.2.2. Sealing performance

The most impactful inaccuracy is the sealing performance of the suction cups. The end-effector consists out of 37 suction cups, each requiring certain conditions to achieve suction pressure. The sealing performance is impacted negatively by contaminates, parallelity issues and surface roughness, resulting in small and large leaks.

These small leaks are only initially present as the force created remains constant. Thus, as the suction cup is pressurizing, the vacuum below the membrane increases. During this increase, the force between the suction-cup wall and the silicone increases, improving its sealing performance. But until this end-condition is reached, air is being sucked into the chamber, reducing the pressure differential and thus the force.
This is proved by applying the force experiment at varying pre-load, figure 7.14. These results indicate that increasing the pre-load improves the sealing performance until convergence is reached, indicating that nearly no small leaks are present. Thus, the compressive flexibility of the silicone seals the small leaks as pre-load is applied. The stagnating nature of figure 7.14 proves that initial leaks are present at lower pre-loads due to less silicone compression, which results in a decrease in end-effector force.

The large leaks are mainly the result of parallelity issues, which result in suction cups not pressurizing. The results from figure 7.14 indicate that the sealing performance is worse for larger radii. This is because larger suction cups are more prone to parallelity issues due to their shear surface size. Additionally, the large wall surface area results in a smaller distributed load resulting in less indentation of the silicone and thus the sealing of large leaks is more improbable. The presence of large leaks is visually confirmed, as at a radius of 3.0 mm and a pre-load of 50 N approximately 8 suction cups seal, which is only 20% of the total amount, see appendix H.4.2. These discrepancies are mitigated by improving the parallelity of the end-effector and by increasing the applied pre-load.

Thus, the discrepancies between the adjusted numerical results and the experiments shown in figure 7.9 are

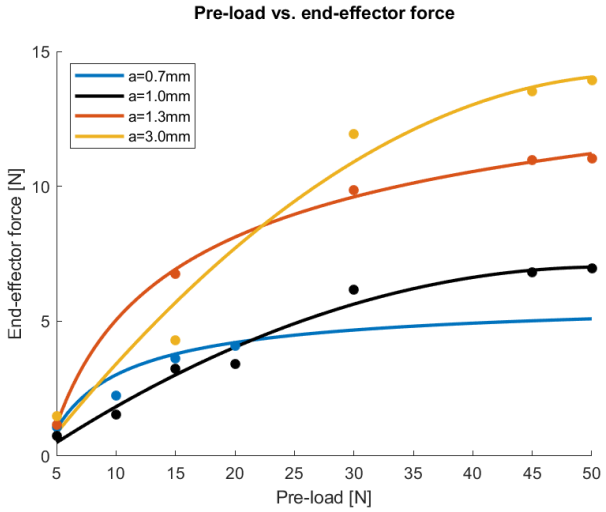

Figure 7.14: Force generated at various pre-loads. Results based on the values in appendix H.4.2, table H.4. The pre-load at $a = 0.7$ mm is stopped at 20 N as to maintain a buffer between the indentation of the silicone and the mean pre-deflection value of the membrane.

mainly due to suction cups not sealing at all and due to small leaks remaining ever so present. The probability of suction cups not sealing increases at larger radii.

7.3. Experiment 3: Pick-up of laminate

The final experiment investigates the ability of the end-effector to pick and place thin laminates. This is done for a flexible laminate (TPU: t = 20 µm) and a more rigid laminate (Aluminum: t = 20 µm). From these experiments, it became apparent that the sealing performance of the end-effector with a PET membrane is insufficient to pick-and-place flexible thin laminates due to parallelity issues. However, the end-effector is capable of pick-and-placing thick ductile laminates as compression is required to improve sealing performance (e.g. silicon and rubber laminates), see figure 7.15.
The parallelity issues, require the addition of a compressible layer and a larger pre-load to improve sealing performance. The compressible layer can either be the laminate itself, or the membrane, however this does impede the design flexibility heavily. Therefore, the current prototype is limited to thicker laminates with a low young's modulus to achieve sufficient compressibility to improve the sealing performance. Thus, to increase laminate compatibility, the sealing performance must be excellent.

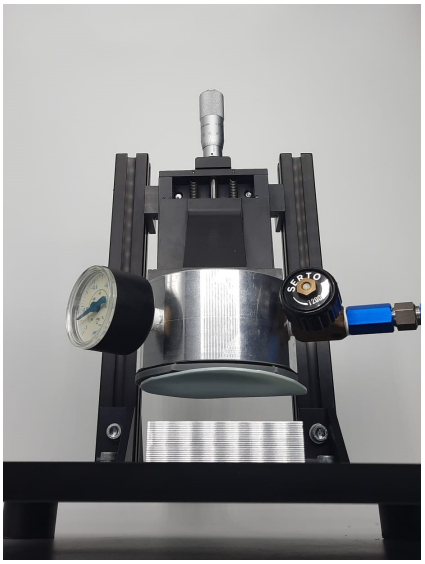

Figure 7.15: Pick-up of a silicone laminate. Laminate thickness: 1.5 mm, Young's modulus: ≈ 5 MPa [32]

8. Design guidelines

From the numerical and experimental results, certain guidelines for the design variables can be set up depending on the laminate type that is to be pick-and-placed. The laminate types are characterized based on the intricate shape and the rigidness (thickness and/or Young's modulus), resulting in four application groups, as seen in table 8.1. In the following four paragraphs, the four types are further elaborated.
These guidelines assume that parallelity issues are solved to ensure proper sealing performance.

	Rigid laminate + Simple shape	**Rigid laminate + Intricate shape**	**Flexible laminate + Simple shape**	**Flexible laminate + Intricate shape**
Radius	Large radius* ($a > 1.3\,\text{mm}$)	Small radius, depends on the features of the laminate	Large radius* ($a > 1.3\,\text{mm}$)	Small radius, depends on the features of the laminate
Membrane height	$h \approx 500\,\mu\text{m}$	$h < 500\,\mu\text{m}$	As small as possible (cappillary condensation distance)**	As small as possible (cappillary condensation distance)**
Membrane thickness	Thin ($t_m \approx 100\,\mu\text{m}$)	Thin ($t_m < 100\,\mu\text{m}$)	As thin as possbile	As thin as possbile
Youngs modulus	Flexible ($E \approx 1\,\text{GPa}$)	Flexible ($E < 1\,\text{GPa}$)	As small as possbile	As small as possbile
Wall thickness (contact area)	$p > 3\,\text{mm}$	$p > 1.5\,\text{mm}$	As large as possible	As large as possible

Table 8.1: Design guidelines for various laminates.
*Large radii are more susceptible to large leaks, thus excellent parallelity is needed to be combined with a larger pre-load. Large radii result in larger stresses, and thus the maximum radius is limited by the yield stress of the membrane and laminate.
**Minimizing the membrane height until the capillary condensation distance results in the preference for hydrophobic materials.

8.1. Rigid laminate + Simple shape

A rigid laminate with a simple shape is the easiest type to pick-and-place. Larger radii may be applied, simplifying the production of the end-effector. However, for larger radii, the stress must not exceed the yield stress of either the membrane or the laminate. Additionally, parallelity must be ensured to prevent any large leaks. The effect of the initial volume/membrane height on the end-effector force is relatively small, however, its impact is not non-zero and must be considered. For all use cases, a thin and flexible membrane is preferred to increase the end-effector force and to improve the sealing performance. Additionally, ductile laminates absorb less energy and therefore the induced pressure required to achieve the desired mean height is minimal. For rigid laminates, this is not crucial and can be accounted for by a slightly larger radius and by increasing the pre-load. As the laminate is rigid, interaction forces are negligible. Therefore, the wall thickness may be of any size, and can be determined based on production requirements.

8.2. Rigid laminate + Intricate shape

This laminate type is very similar to the previous laminate, however, the radii size is limited and depends on the feature size of the laminate. This limits the force created within a singular suction cups. To counter this, simply more suction cups can be added, as the wall thickness can be reduced accordingly. Additionally, the membrane height, thickness, and young's modulus can be decreased to further improve the performance.

8.3. Flexible laminate + Simple shape

A flexible laminate with a simple shape can have larger radii to simplify the production of the end-effector. For flexible laminates, the force that can be generated is reduced enormously. This is due to their large deflection, resulting in a decrease in suction force. Therefore, it is important to generate as much force as possible over the entire surface of the end-effector. This is achieved by minimizing the membrane height, thickness, and young's modulus. The membrane height can be reduced to the capillary condensation distance, which is decreased by utilizing a hydrophobic membrane and by reducing the relative humidity of the end-effector environment. The young's modulus of the membrane is vital, as it must ensure that the suction cups have an excellent sealing performance with a pre-load. As interaction forces have an important effect, it is favorable to utilize them in favor of the end-effector. Thus, the wall thickness of the suction cups may be as large as possible to increase the interaction forces between the membrane and the laminate to overcome gravity.

8.4. Flexible laminate + Intricate shape

This laminate type is similar to the previous laminate, but it is limited in the radii that can be applied. The minimization of the membrane height, thickness, and Young's modulus also means that the maximum pressure differential is reached at smaller radii. This, combined with more suction cups, results in enough force to achieve successful pick-up and release. Improving these three parameters allows for even smaller radii, and thus more complex shapes can be pick-and-placed.

9. Conclusion

The goal of the thesis was to create an end-effector to pick-and-place laminates of various materials for the creation of multi-material architectures. The chosen end-effector design induces a pressure differential with a membrane, and is capable to achieve a large switching force at a high throughput for delicate and geometric complex laminates. The experiments and numerical model accurately illustrate membrane deformation, and show that force switching is achieved for pick-and-place. Additionally, the numerical model and the experimental results show that the suction forces can vary enormously depending on the target laminate. For the pick-and-place of ductile laminates with an intricate shape, it is preferable to minimize the membrane height, membrane thickness and Young's modulus to create enough force. The radius size must be chosen according to the required features sizes of the target laminates to ensure suction cups seal. The created prototype is capable of manipulating rigid, intricate laminates, as the membrane material must be more ductile.

Analysis of the experimental results illustrated the sensitivity of the prototype to the following inaccuracies that should be mitigated 1) production inaccuracies of the end-effector, and 2) ductility and application of membrane material. When producing the membrane scaffold, the DLP printer with which it is created has large inaccuracies in the x/y plane, resulting in unpredictable suction-cup radii and edge fillets. Additionally, the current end-effector assembly cannot ensure parallelity, resulting in suction cups leaking.
The membrane material (PET) is chosen for its thickness and adhesive backing. However, the adherence method of membrane resulted in large initial deformations, limiting the application of the end-effector to only rigid laminates. Additionally, it is preferable to choose a more ductile membrane (e.g. PDMS) to improve the end-effector forces and its sealing performance.

In conclusion, an end-effector based on the membrane induced pressure differential is a design path which is worth investigating further for the creation of multi-material metamaterials. Depending on the application and thus the target laminates, certain design guidelines are set up. These can be used for further research. Additionally, further research is required to reduce production inaccuracies and allow for the application of more ductile membranes without adhesives impeding the end-effector performance.

Bibliography

[1] Da Chen and Xiaoyu Zheng. Multi-material additive manufacturing of metamaterials with giant, tailorable negative poisson's ratios. Scientific Reports, 8(1):9139, Jun 2018.

[2] Tao Chen, Suyan Li, and Hui Sun. Metamaterials application in sensing. Sensors, 12(3):2742–2765, 2012.

[3] Lee Fok, Muralidhar Ambati, and Xiang Zhang. Acoustic metamaterials. MRS Bulletin, 33(10):931–934, 2008.

[4] Mirka A. Lewinska, J.A.W. (Hans) van Dommelen, Varvara G. Kouznetsova, and Marc G.D. Geers. Broadening the attenuation range of acoustic metafoams through graded microstructures. Journal of Sound and Vibration, 483, September 2020.

[5] M.A. Lewińska, J.A.W. van Dommelen, V.G. Kouznetsova, and M.G.D. Geers. Towards acoustic metafoams: The enhanced performance of a poroelastic material with local resonators. Journal of the Mechanics and Physics of Solids, 124:189–205, 2019.

[6] Meisam Askari, David A. Hutchins, Peter J. Thomas, Lorenzo Astolfi, Richard L. Watson, Meisam Abdi, Marco Ricci, Stefano Laureti, Luzhen Nie, Steven Freear, Ricky Wildman, Christopher Tuck, Matt Clarke, Emma Woods, and Adam T. Clare. Additive manufacturing of metamaterials: A review. Additive Manufacturing, 36:101562, 2020.

[7] Xin Wu, Yutai Su, and Jing Shi. Perspective of additive manufacturing for metamaterials development. Smart Materials and Structures, 28(9):093001, aug 2019.

[8] Filippus Hulsman. Developing a novel production process for the creation of multi-material architectures, 2021.

[9] T. P. Russell. Surface-responsive materials. Science, 297(5583):964–967, 2002.

[10] A. Hamza, V.A. Pham, T. Matsuura, and J.P. Santerre. Development of membranes with low surface energy to reduce the fouling in ultrafiltration applications. Journal of Membrane Science, 131(1):217–227, 1997.

[11] Lingbo Zhu, Jianwen Xu, Zhuqing Zhang, D.W. Hess, and C.P. Wong. Lotus effect surface for prevention of microelectromechanical system (mems) stiction. In Proceedings Electronic Components and Technology, 2005. ECTC '05., pages 1798–1801 Vol. 2, 2005.

[12] W.Robert Ashurst, C Carraro, R Maboudian, and W Frey. Wafer level anti-stiction coatings for mems. Sensors and Actuators A: Physical, 104(3):213–221, 2003. Selected papers based on contributions revised from the Technical Digest of the 2002 Solid-State Sensors, Actuators and Microsystems workshop.

[13] Zhi-You Zhou, Na Tian, Jun-Tao Li, Ian Broadwell, and Shi-Gang Sun. Nanomaterials of high surface energy with exceptional properties in catalysis and energy storage. Chem. Soc. Rev., 40:4167–4185, 2011.

[14] Vladimir S Bagotsky. Fundamentals of electrochemistry, volume 44. John Wiley & Sons, 2005.

[15] Niels Tas, Tonny Sonnenberg, Henri Jansen, Rob Legtenberg, and Miko Elwenspoek. Stiction in surface micromachining. Journal of Micromechanics and Microengineering, 6(4):385, 1996.

[16] Koninklijke Nederlandse Meteorologisch Instituut. Klimaatviewer, 2020.

[17] Sungbum Cho, Namyun Kim, Kwangsun Song, and Jongho Lee. Adhesiveless transfer printing of ultrathin microscale semiconductor materials by controlling the bending radius of an elastomeric stamp. Langmuir, 32(31):7951–7957, 2016.

[18] Matthew A. Meitl, Zheng-Tao Zhu, Vipan Kumar, Keon Jae Lee, Xue Feng, Yonggang Y. Huang, Ilesanmi Adesida, Ralph G. Nuzzo, and John A. Rogers. Transfer printing by kinetic control of adhesion to an elastomeric stamp. Nature Materials, 5(1):33–38, Jan 2006.

[19] Xue Feng, Matthew A. Meitl, Audrey M. Bowen, Yonggang Huang, Ralph G. Nuzzo, and John A. Rogers. Competing fracture in kinetically controlled transfer printing. Langmuir, 23(25):12555–12560, Dec 2007.

[20] Andrew Carlson, Audrey M. Bowen, Yonggang Huang, Ralph G. Nuzzo, and John A. Rogers. Transfer printing techniques for materials assembly and micro/nanodevice fabrication. Advanced Materials, 24(39):5284–5318, 2012.

[21] Hongyu Luo, Chengjun Wang, Changhong Linghu, Kaixin Yu, Chao Wang, and Jizhou Song. Laser-driven programmable non-contact transfer printing of objects onto arbitrary receivers via an active elastomeric microstructured stamp. National Science Review, 7(2):296–304, Feb 2020.

[22] Rui Li, Yuhang Li, Chaofeng Lü, Jizhou Song, Reza Saeidpouraza, Bo Fang, Yang Zhong, Placid M. Ferreira, John A. Rogers, and Yonggang Huang. Thermo-mechanical modeling of laser-driven non-contact transfer printing: two-dimensional analysis. Soft Matter, 8:7122–7127, 2012.

[23] Rui Li, Yuhang Li, Chaofeng Lu, Jizhou Song, Reza Saeidpourazar, Bo Fang, Yang Zhong, Placid Ferreira, John Rogers, and Yonggang Huang. Axisymmetric thermo-mechanical analysis of laser-driven non-contact transfer printing. International Journal of Fracture, 176, 08 2012.

[24] Dung-An Wang, Huy-Tuan Pham, and Yi-Han Hsieh. Dynamical switching of an electromagnetically driven compliant bistable mechanism. Sensors and Actuators A-physical, 149:143–151, 2009.

[25] Slava Krylov, Bojan R Ilic, David Schreiber, Shimon Seretensky, and Harold Craighead. The pull-in behavior of electrostatically actuated bistable microstructures. Journal of Micromechanics and Microengineering, 18(5):055026, apr 2008.

[26] Slava Krylov, Bojan R. Ilic, and Stella Lulinsky. Bistability of curved microbeams actuated by fringing electrostatic fields. Nonlinear Dynamics, 66(3):403, Apr 2011.

[27] Mario Versaci and Francesco Carlo Morabito. Electrostatic circular membrane mems: An approach to the optimal control. Computation, 9(4), 2021.

[28] Jukka-Pekka Uusitalo, Ville Ahola, Lasse Soederlund, Matti Linjama, Maarit Juhola, and Lauri Kettunen. Novel bistable hammer valve for digital hydraulics. International Journal of Fluid Power, 11(3):35–44, 2010.

[29] Jin Qiu, Jeffrey H. Lang, Alexander H. Slocum, and Alexis Christian Weber. A bulk-micromachined bistable relay with u-shaped thermal actuators. Journal of Microelectromechanical Systems, 14:1099–1109, 2005.

[30] Jasmina Casals-Terre, Andreu Fargas-Marques, and Andrei M. Shkel. Snap-action bistable micromechanisms actuated by nonlinear resonance. Journal of Microelectromechanical Systems, 17(5):1082–1093, 2008.

[31] Manuel Dorfmeister, Bernhard Kössl, Michael Schneider, and Ulrich Schmid. A novel bi-stable mems membrane concept based on a piezoelectric thin film actuator for integrated switching. Proceedings, 2(13), 2018.

[32] Ansys. Granta edupack, 2019.

[33] Dr. Marcus Bluemel (Laboratory Manager); BASF. Production of thermoplastic polyurethane, 2022.

[34] Dassault Systems. Solidworks cad software, 2021.

[35] F. Arai and T. Fukuda. Adhesion-type micro end effector for micromanipulation. In Proceedings of International Conference on Robotics and Automation, volume 2, pages 1472–1477 vol.2, 1997.

[36] Seok Kim, Jian Wu, Andrew Carlson, Sung Hun Jin, Anton Kovalsky, Paul Glass, Zhuangjian Liu, Numair Ahmed, Steven L. Elgan, Weiqiu Chen, Placid M. Ferreira, Metin Sitti, Yonggang Huang, and John A. Rogers. Microstructured elastomeric surfaces with reversible adhesion and examples of their use in deterministic assembly by transfer printing. Proceedings of the National Academy of Sciences, 107(40):17095–17100, 2010.

[37] Seok Kim, Andrew Carlson, Huanyu Cheng, Seungwoo Lee, Jung-Ki Park, Yonggang Huang, and John A. Rogers. Enhanced adhesion with pedestal-shaped elastomeric stamps for transfer printing. Applied Physics Letters, 100(17):171909, 2012.

[38] Tomokazu Takahashi, Masato Suzuki, and Seiji Aoyagi. suctionpus bioinspired vacuum gripper with micro bumps. In 2016 IEEE 11th Annual International Conference on Nano/Micro Engineered and Molecular Systems (NEMS), pages 508–511, 2016.

[39] T. Tomokazu, S. Kikuchi, M. Suzuki, and S. Aoyagi. Vacuum gripper imitated octopus sucker-effect of liquid membrane for absorption-. In 2015 IEEE/RSJ International Conference on Intelligent Robots and Systems (IROS), pages 2929–2936, 2015.

[40] Condair. What are acceptable humidity levels in office buildings, and why?, 2019.

[41] Massachusetts Institute of Technology: MIT. Material: Pdms (polydimethylsiloxane), 2002.

[42] KNMI. Van lage druk naar hoge druk, 2017.

[43] Chang Liu. Foundations of MEMS. Pearson Education, 2012.

[44] Milton J Rosen and Joy T Kunjappu. Surfactants and interfacial phenomena. John Wiley & Sons, 2012.

[45] Frank Weinhold. Quantum cluster equilibrium theory of liquids: Illustrative application to water. The Journal of Chemical Physics, 109:373–384, 07 1998.

[46] William B. Jensen. The universal gas constant r. Journal of Chemical Education, 80(7):731, Jul 2003.

[47] Saint-Gobain Tape Solutions. 12.sl polyester film tape, 2021.

[48] 3M. 3m™ polyester tape 8991/8991l, 2015.

[49] MatWeb. Overview of materials for polyester film, 2022.

[50] B. van Lancker, W. de Corte, and J. Belis. Material properties of a structureal silicone for linear adhesive glass-metal connections. Conference on Architectural and Structural Applications of Glass, 2016.

[51] Maie A. Fadel, Nagwa A. Kamel, Mirhane M. Darwish, Salwa L. Abd El-Messieh, Kamal N. Abd-El-Nour, and Wafaa A. Khalil. Preparation and characterization of polyethylene terephthalate-chamomile oil blends with enhanced hydrophilicity and anticoagulant properties. Progress in biomaterials, 9(3):97–106, Sep 2020. 32566967[pmid].

[52] Eriks Sealing Technology. Technical manual for sealing elements, 2022.

[53] Sarina Bao, Kai Tang, Anne Kvithyld, Merete Tangstad, and Abel Engh. Wettability of aluminum on alumina. Metallurgical and Materials Transactions B, 42:1358–1366, 06 2011.

[54] Evgeniya Orlova, Dmitriy Feoktistov, and Geniy Kuznetsov. Investigation of drop dynamic contact angle on copper surface. EPJ Web of Conferences, 82:01053, 01 2015.

[55] Timothy Douglas and Håvard Haugen. Coating of polyurethane scaffolds with collagen: Comparison of coating and cross-linking techniques. Journal of materials science. Materials in medicine, 19:2713–9, 08 2008.

[56] Eclipse engineering inc. How surface finish affects sealing performance, 2022.

[57] Xometry - Manufacturing on demand. Selecting right surface roughness for cnc machining, 2022.

[58] G Marom, S Fischer, FR Tuler, and HD Wagner. Hybrid effects in composites: conditions for positive or negative effects versus rule-of-mixtures behaviour. Journal of Materials Science, 13(7):1419–1426, 1978.

[59] Keyence. Vhx-6000 series brochure, 2022.

[60] Xizhi Sun and Kai Cheng. Micro-/nano-machining through mechanical cutting. Micro-Manufacturing Engineering and Technology, pages 24–38, 12 2010.

[61] Sabino Azcarate, Luis Uriarte, Samuel Bigot, Pieter Jan Bolt, Lutz Staemmler, Guido Tosello, Stephan Roth, and Andreas Schoth. Hybrid tooling: A review of process chains for tooling microfabrication within 4m. In Proceedings of 2nd International Conference on Multi-Material Micro Manufacture (4M), pages 305–308, United Kingdom, 2006. Elsevier. 2nd International Conference on Multi-Material Micro Manufacturing, 4M2006 ; Conference date: 20-09-2006 Through 22-09-2006.

[62] V Piotter, W Bauer, T Benzler, and A Emde. Injection molding of components for microsystems. Microsystem Technologies, 7(3):99–102, 2001.

[63] Ada-Ioana Bunea, Nuria del Castillo Iniesta, Ariadni Droumpali, Alexandre Emmanuel Wetzel, Einstom Engay, and Rafael Taboryski. Micro 3d printing by two-photon polymerization: configurations and parameters for the nanoscribe system. In Micro, volume 1, pages 164–180. MDPI, 2021.

[64] Nanoscribe. Photonic professional gt2, 2022.

[65] MatWeb. Overview of materials for silicone, rtv, adhesive/sealant grade, 2022.

[66] Civen metal. High-precision ra copper foil, 2022.

[67] Xin Gen. Pu film, 2022.

[68] Xiang-Qian Yin, Li-Jun Peng, Saif Kayani, Lei Cheng, Jian-Wei Wang, Wei Xiao, Li-Gen Wang, and Guo-Jie Huang. Mechanical properties and microstructure of rolled and electrodeposited thin copper foil. Rare Metals, 35(12):909–914, Dec 2016.

[69] Copper development association Inc. C11000, 2022.

[70] Igor Sokolov, Quy K. Ong, Hasan Shodiev, Nina Chechik, David James, and Mike Oliver. Afm study of forces between silica, silicon nitride and polyurethane pads. Journal of Colloid and Interface Science, 300(2):475–481, 2006.

[71] Hiroyuki Ohshima. Chapter 1 - interaction of colloidal particles. In Hiroyuki Ohshima and Kimiko Makino, editors, Colloid and Interface Science in Pharmaceutical Research and Development, pages 1–28. Elsevier, Amsterdam, 2014.

[72] Barton Dahneke. The influence of flattening on the adhesion of particles. Journal of Colloid and Interface Science, 40(1):1–13, 1972.

[73] AZO materials. Electrolytic tough pitch copper (uns c11000), 2012.

[74] Xiyong Wang, Xuefeng Liu, Laixin Shi, Jingkun Li, and Jianxin Xie. Characteristic and formation mechanism of matt surface of double-rolled copper foil. Journal of Materials Processing Technology, 216:463–471, 2015.

[75] Huan Li, Tridib K. Sinha, Jinho Lee, Jeong Seok Oh, Youngjoon Ahn, and Jin Kuk Kim. Melt-compounded keratin-tpu self-assembled composite film as bioinspired e-skin. Advanced Materials Interfaces, 5(19):1800635, 2018.

[76] ASTM international. Temper designations for copper and copper alloys—wrought and cast, 2002.

[77] Inc. Smooth-On. Durometer shore hardness scale, 2022.

[78] Roya Maboudian and Roger T. Howe. Critical review: Adhesion in surface micromechanical structures. Journal of Vacuum Science & Technology B: Microelectronics and Nanometer Structures Processing, Measurement, and Phenomena, 15(1):1–20, 1997.

[79] William M Haynes, David R Lide, and Thomas J Bruno. CRC handbook of chemistry and physics. CRC press, 2016.

[80] W Merlijn van Spengen, Robert Puers, and Ingrid De Wolf. A physical model to predict stiction in MEMS. Journal of Micromechanics and Microengineering, 12(5):702–713, aug 2002.

[81] Frank Philip Bowden, Frank Philip Bowden, and David Tabor. The friction and lubrication of solids, volume 1. Oxford university press, 2001.

[82] Zhao Yapu. Stiction and anti-stiction in mems and nems. Acta Mechanica Sinica, 19(1):1–10, Feb 2003.

[83] Steven K Lamoreaux. The casimir force: background, experiments, and applications. Reports on Progress in Physics, 68(1):201–236, dec 2004.

[84] M. Bordag, U. Mohideen, and V.M. Mostepanenko. New developments in the casimir effect. Physics Reports, 353(1):1–205, 2001.

[85] R. Hausbrand, M. Stratmann, and M. Rohwerder. The physical meaning of electrode potentials at metal surfaces and polymer/metal interfaces: Consequences for delamination. Journal of The Electrochemical Society, 155(7):C369, 2008.

[86] James A Greenwood and JB Pl Williamson. Contact of nominally flat surfaces. Proceedings of the royal society of London. Series A. Mathematical and physical sciences, 295(1442):300–319, 1966.

[87] Chengwei Wu and Linqing Zheng. A general expression for plasticity index. Wear, 121(2):161–172, 1988.

[88] A. Santiago-Alvarado, Angel Cruz-Felix, Fernando Iturbide, and Brenda Licona-Morán. Physical-chemical properties of pdms samples used in tunable lenses. International Journal of Engineering Science and Innovative Technology, 3:563–571, 03 2014.

[89] Alex CM Kuo. Poly (dimethylsiloxane). Polymer data handbook, pages 411–435, 1999.

A. Material properties

Material properties	Symbol	(Thermoplastic) Polyurethane	Copper - C11000*
Production process	-	Thin nozzle or Blow molding [33]	Electro-deposited & rolled [66]
Thickness	T	20 μm [67]	9 μm [66]
Area	S	100 cm^2	100 cm^2
Density	ρ	1.12×10^3 kg/m^3 [33]	8.89×10^3 kg/m^3
Fracture toughness	K_c	$0,192 - 1,29$ MPa [32]	223 – 318 MPa [68]
Youngs modulus	E	$2,5 - 30$ MPa [32]	115 – 117 GPa
Yield strength	σ_y	40 – 51 MPa	206 Mpa [69]
Coefficient of thermal expansion (CTE) [32]	α	$1.6 - 1.65 \times 10^{-4}$ Strain/°C	$1.68 - 1.69 \times 10^{-5}$ Strain/°C
Hamaker constant	A_{HAM}	$\approx 1.3 \times 10^{-20}$ J [70, 71]	$\approx 28.3 \times 10^{-20}$ J [72]
Poisson ratio	ν	$0,47 - 0,49$ [32]	$0,34$ [73]
Effective hardness	H	87** [33]	40 *** [73]
Contact angle	c_A	99.5° [55]	87° [54]
Mean distance (surface roughness)****	$\bar{z}$	≈ 45 nm [74]	≈ 47 nm [75]

Table A.1: Material properties of case. *Cold-Worked and Precipitation Heat-treated which is 1/2 Hard [76]. **Shore hardness A measurement (DIN ISO 48-4 (3s)) the hardness scale measures the hardness of flexible mold rubbers [77]. ***Rockwell F Scale.****Mean distances are estimated based on literature and considering the corresponding production technique.

B. Surface interaction forces

B.1. Capillary condensation

The largest stiction force is capillary condensation. Bowden and Tabor investigated experimentally the stiction force as a result of the liquid tension of water. They found an experimental dependency of the capillary force regarding the relative humidity, as shown in figure B.1. The humidity of the environment has a tremendous effect on the capillary-based stiction force. For two perfectly flat surfaces near each other, the capillary surface interaction energy is quantified according to the Young–Laplace equation [78].

$$\begin{aligned} e_{cap}(z) &= \gamma(\theta_1 - \theta_2)|_{z \leq d_{cap}} \\ e_{cap}(z) &= 0|_{z > d_{cap}} \end{aligned} \tag{B.1}$$

In equation (B.1) γ is the surface tension of water (at 20 °C: 72.75×10^{-3} N/m) [44], θ is the contact angle of water on the surface and d_{cap} is the characteristic distance between the two plates. If the distance is smaller than d_{cap} water will, capillary condense and gives rise to a stiction force. This characteristic distance is dependent on the materials and humidity of the environment, as indicated in equation (B.2).

$$d_{cap} \approx \frac{2\gamma(T)v\cos\theta}{RT\log(H_r)} \tag{B.2}$$

In which v is the liquid molar volume of water, R is the gas constant ($8.314\,\mathrm{JK^{-1}mol^{-1}}$) [46], T is the absolute temperature in Kelvin and H_r is the relative humidity. With these two formulas, the surface interaction as a result of the humidity of the experimental room can be calculated. In both formulas, surface tension is indicated as a function which is dependent on the temperature. This effect is not large but does occur and is material dependent [79]. For this, a fit is created as seen in equation (B.3) [80]. This fit is not perfect but does approach the reality very close and its discrepancy is negligible.

$$\gamma(T) = (75.6 - 0.167T) \times 10^{-3}\mathrm{Jm^{-2}} \tag{B.3}$$

The formula indicates that the surface tension of water decreases when temperatures increase. In general, if water is present, the capillary force will dominate all other forces and surface interaction energies, which will be discussed in the following paragraphs.

B.2. Van der Waals

The van der Waals force between molecules becomes larger as the intermittent distance between the surfaces reduces. The adhesion behavior occurs in absence of water and are not dependent on the environment. However, it is dependent on the surface roughness and in the case of exceptionally smooth surfaces, the surface energy due to van der Waals interactions are

$$e_{vdW} = \frac{A_{HAM}}{12\pi z^2}|_{z > d_{co}} \tag{B.4}$$

with e_{vdW} being the surface energy due in $\mathrm{J/m^2}$, A_{HAM} is the Hamaker constant in Joule, z the distance between the two surfaces [80]. However, this distance only results in a surface energy in a specific domain. If the plates are far away from each other, the van der Waals surface energy is negligible. If the two plates come to close to each other, the van der Waals force will become negative and will become a repulsive force between the plates. This is due to electron shell deformation, which results in a cut-off distance and is universally determined at $d_{co} = 0.165\,\mathrm{nm}$ which is slightly less than the inter-atomic distance.

B.3. Casimir

Compared to the van der Waals force, the Casimir force takes effect at larger gap distances, as demonstrated in figure B.2 [82]. The Casimir force is the result of a very unintuitive consequence of quantum electrodynamics. The force between two parallel uncharged plates as a result of the Casimir force is quantified by equation (B.5).

$$E(z) = \frac{\pi^2 hc}{2 * \pi * 720 z^3} \qquad S >> z^2 \tag{B.5}$$

Where z is yet again the distance between the plates and S being the surface of the plates. This formula is only applicable if $S >> z^2$. This condition is met as the surface of the sheets is about $100\,\mathrm{cm^2}$.
This equation can be derived by assigning a zero-point energy of $\frac{1}{2}hc$ to each electromagnetic mode (photon). As Lamoreaux explains it so nicely [83]: "The change in total energy density between the plates due to modification of the mode structure compared with free space, as a function of the separation, d, leads to the force of attraction." Thus, the Casimir force is a fundamental force which is independent of material and humidity.

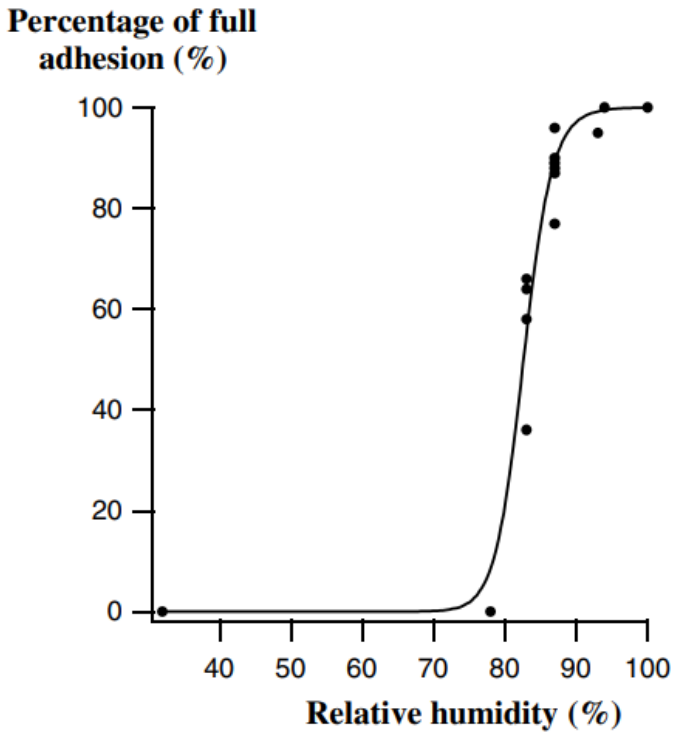

Figure B.1: Adhesion as function of the humidity. [81]

B.4. Electrostatic

An Electrostatic force is not only due to an applied charge but can be the result of a contact potential difference. The Coulomb interaction between the two surfaces can be described with the following formula.

$$F_c = \frac{\epsilon V^2}{2z^2} \tag{B.6}$$

Here F_c is the force, V is the potential difference and z is the distance between the plates. In this case, no voltage is induced, however a potential may arise due to contact and/or tribocharging. Contact potential is the difference in electrostatic potential between two metals, which does not occur in the process [14]. However, the electrode potentials at the interface between metal and organic coating can be of real electrochemical significance [85]. Tribocharging is caused by rubbing surfaces, which may introduce a potential. In general, the electrostatic force will not be a significant force during laminate transfer.

B.5. Gravitational forces

During the process, the weight of the various laminates needs to be considered. These forces are relatively small compared to the interaction forces and can sometimes be neglected. In this case, there are added as the sheets cover a substantial area. To make the comparison easier, the gravitational force is quantified as a distribution force.

$$P_g = \frac{F_g}{S} = g * \rho * t \tag{B.7}$$

With P_g being the gravitational distributed load, F_g is the gravitational force, S is the total surface of the to be manipulated laminates, g is the gravitational acceleration, ρ is the density of the laminate and t is the corresponding laminate thickness. In the case of copper and polyurethane, the forces are seen in table B.1.

	TPU	**Copper**
P_g	1.74 Pa	0.22 Pa
F_g	17.4 mN	2.2 mN

Table B.1: Gravity induced forces and pressures.

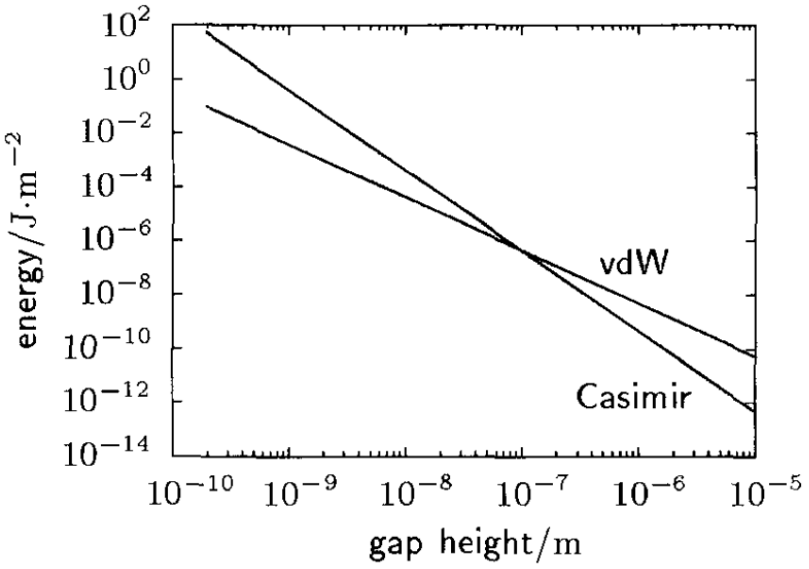

Figure B.2: Force comparison of van der Waals and Casimir forces for tick gold films. [84]

C. Concept assessment

C.1. Selection criteria

In section 3.1 six different concepts are described. It is evident that the different concepts have their specific properties, with their advantages and disadvantages. In the following sections, the selection criteria are described and applied to assess the concepts. These are used to select a concept in section 3.2.

The limitations and characteristics of the different concepts are investigated with a set of criteria. These criteria are based on the expected required characteristics of multi-material metamaterials.

C.1.1. Material diversity

The first criterion is the extent to which an end-effector concept allows application of multiple materials.
The concepts are analyzed based on the range of the Young's modulus of the materials that are applicable within a single concept. Additionally, it analyses other mechanical properties restricting certain material groups, such as thermal properties, conductivity and hardness.

C.1.2. Geometric capability

Another important criterion is the capability to handle laminates with diverse shapes. The end-effector must handle such laminates and therefore is required to create a uniform-force despite these geometric irregularities.
The concepts are analyzed based on the distribution with which a force is generated and its dependency on laminate surface quality.

C.1.3. Delicacy

The end-effector must pick up the laminate delicately and release it onto the previous laminate without destroying the previous stack.
The concepts are analyzed based on the method and range of force application method. For example: A large force generation only during laminate release is not preferable during stacking of a complex and delicate stack.

C.1.4. Throughput

An end-effector with high throughput capabilities has the potential to deliver consistency and increase accessibility. Due to consistent production, research can be compared accurately, enabling further development.
The concepts are analyzed based on the speed of the expected end-effector force switching.

C.1.5. Force generation

For the transportation of the laminates, it is important that the force generated is sufficient to create a force to overcome gravity (F_G) and the layer interaction forces (F_{CL}). Additionally, the end-effector must release the layer, which requires the end-effector to create a force variation large enough to release the layer onto the previously stacked laminate.
This criterion is investigated based on the maximum generated switchable force.

C.2. Concept evaluation

The concepts are assessed based on their strengths and weaknesses for each of the criteria, table 3.1. The argumentation of table is written in the sections below.

	Contact area: Peeling	**Contact area: Expanding membrane**	**Contact area: Membrane actuation**	**Pressure differential: Temperature induced**	**Pressure differential: Speed induced**	**Pressure differential: The octopus**
Material diversity	+	- -	+ -	+ -	+ +	+ +
Geometric capability	+ +	+ -	+	+ -	-	+ -
Delicacy	- -	+ +	+	+	- -	+ +
Throughput	+ +	+ +	+	-	+ +	+
Force generation	+	+	-	+ -	+ +	+

Table C.1: Qualitative selection table with the various concepts and criteria.

Contact area: Peeling
Contact peeling utilizes a PDMS stamp which is rolled up. This allows for a wide range of materials which can be applied. However, as a radius is required to pick up and release the laminates, certain flexibility is required. Therefore, this concept is slightly limited to materials with a low modulus of elasticity.

Because the stamp covers the whole surface, it has excellent geometric capabilities. The shape of the laminate does not impede the mechanism, and therefore the geometric shape of the laminate is completely unrestricted.

When depositing the laminate, a large force is exerted unto the underlying structure. If the underlying structure is intricate (e.g.metamaterial), the large force could result in part failure. Therefore, the concept release method is not delicate.

The throughput of the stamp is excellent. As laminates are first rolled unto the stamp and then rolled off, the system can be applied continuously at a high rate. The generated force during pickup is mainly based on the interlayer adhesion, release of the laminate is where a large force is created. Therefore, the force fluctuation is large, but mainly achieved during laminate release.

Contact area: Expanding membrane
The working principle is the thermal match between the membrane and the laminate to ensure de-lamination. The large amount of initial parameters which must match limits the end-effector to certain materials. So in essence it can be designed to manipulate many materials, but it is then not applicable for different materials. This is due to the necessary thermal property match between the laminate and the membrane. This is an unfavorable property for multi-material builds, as a new material laminate consequently means a new end-effector with the corresponding membrane needs to be manufactured and mounted. Therefore, material diversity is not great for this concept.

The addition of many membranes allows for a more uniform force distribution. The more membranes are present in a certain area, the better its performance in both delicate maneuverability and force generation thus minimization of the membrane radius is favorable. However, this decrease in size is limited due to the membrane and the required air pocket for successful thermal expansion of the air. Therefore, the amount of suction cups is limited reducing the feature size over which a uniform force can be distributed reducing its geometric complexity of the shape.

The main working force for pick-up is interlayer adhesion, and for release thermal properties are utilized. As the air is only heated momentarily by lasers, the laminates are not affected. Therefore, this concept can very delicately pick-up and release laminates.

Throughput of the concept is excellent. The concept only requires the energy input for the air pockets which are in contact with the laminate, and therefore lasers can selectively heat the small air pockets, which is achieved very rapidly.

Force generation is dependent on the material combination used. Additionally, as the membrane and air pocket combination requires more complex production methods, the minimum radius achievable is limited. This therefore slightly limits the achievable force generated by the concept.

Contact area: Membrane actuation
Membrane actuation results in large deformations to achieve pick-up and release. This large deformation ensures that the contact area is reduced enormously for material with a large modulus of elasticity. However, for materials with a modulus of elasticity equal or lower than the membrane itself, the deformation would result in the deformation of the laminate and thus the contact area is reduced minimally.
Additionally, the bi-stable mechanism uses contact area reduction to generate its force. To ensure pick-up, the interlayer interaction forces must overcome gravity and thus material properties must match to achieve such interaction forces. Thus, a few limitations do impede the material diversity of the concept.

In this concept to the following statement holds true. The smaller the holes, the more uniform the force distribution, the better its geometric capability. As the bi-stable membranes must be actuated and mounted to an end-effector, production limitations are present. Therefore, the geometric capability of the design is good, but limited by its membrane size.

The membrane itself creates large deformations. Applying the membrane directly onto a laminate would result in large deformations, which could harm the to be manipulated membrane. However, the membrane can also be used to create a pressure differential, as seen in section 3.1.4 & section 3.1.6. This application method is more delicate.

Throughput of the membrane is excellent, as the membranes can be individually electrically actuated. This allows for rapid membrane actuation, enabling the end-effector for rapid pick-up and release.

The bistable membrane is delicate and is limited in the forces it can exert [31]. The switching force created is the result of the large displacement, which thus changes the contact area and thus the layer interaction force. This limits the force generation achievable.

Pressure differential: Temperature induced
The concept fundamentally works by creating a temperature induced pressure differential. Due to the pressure which is directly correlated to the temperature, any temperature limitations would impede the suction pressure. Therefore, for materials with a low service temperature, the suction pressure achievable is limited.

The end-effector concept consists of a solid piece with numerous holes. This design simplifies manufacturing, allowing for the minimization of the hole diameter, and thus more holes can be made. This allows for the pick-up of complex geometric shapes. Additionally, due to their abundance, a relative uniform force distribution can be created, allowing for delicate manipulation.

Throughput of this concept is limited due to the required time to heat and cool the end-effector. If larger forces are required, the temperature fluctuations increase as well which would also impede the throughput capabilities of the concept.

The concept requires a seal to be created between the end-effector and the to be picked-up laminate. Thus surface roughness must be minimized to ensure that a pressurized chamber can be created. The smoother the surface, the better the seal and the longer the suction pressure can be maintained. Additionally, The temperature range in which the end-effector operates must be in the operating

range of the to be moved laminate. Therefore, the force generated is temperature limited by the material that is to be moved. Due to the requirement on the surface quality and the temperature, force generation can be good but is limited.

Pressure differential: Speed induced
The benefit of this method is that the stamp is a single PDMS part that deforms. As the force is created based on the stamp geometry and speed, the forces created can be changed easily, allowing for the manipulation of a wide variety of laminates. Therefore, the material diversity of this concept is excellent.

The stamp collapses to create a larger contact area and pressure differential. However, when reverting to its initial condition, certain contact points must be maintained to keep the laminate attached to the end-effector. This means that every laminate must have certain attaching points, limiting its geometric capability.

The force created by the stamp is mainly created when retracting the stamp. This induces a considerable pressure. The moment the laminate is released of the carrier material, the pressure fluctuation acting upon the laminate is considerable. The release force is created rigorously, thus resulting in a large peak force which could damage the laminate. Due to this rigorous nature, it cannot be used on delicate materials, thus limiting the laminate material and thickness. Therefore, delicacy of the laminate cannot be ensured consistently.

This simple stamp design results in a high-speed and repeatable process. The stamp can create large forces, which enables the release of the laminate of the carrier material in a rapid speed. The high throughput and force generation is favorable, but does influence the delicacy cirterion negatively.

Pressure differential: The octopus
The main working principle is a pressure differential, which is independent of the material on which it is applied. Therefore, it has excellent material diversity.

Similar to the temperature induced concept, the geometric capability is limited by the surface roughness of the laminate. Additionally, because a membrane is suspended over a small hole, fabrication is more complex. Therefore, the suction cups cannot be minimized indefinitely, limiting the geometric complexity it can pick up.

The concept creates a pickup force predominately by the suction pressure created. Additionally, the membrane is expanded to ensure release of the laminate. This continuous two directional actuation method allows for very precise and delicate force generation in both direction. This allows for fine control and thus delicate handling.

The concept has an excellent throughput as the suction cups are controlled with a vacuum pump. The use of a vacuum pump allows for rapid actuation, resulting in a higher throughput. However, the use of a vacuum pump requires additional tubing attached to the end-effector, thus increasing the weight and therefore its maneuverability.

The low-pressure volume in the suction cups (P_s) is preferably as small as possible. A smaller size suction cup allows for a more uniform pressure distribution. As this is slightly limited, so is the force variation that can be achieved. Additionally, the force generated is very dependent on the surface roughness as a proper seal must be ensured to achieve a pressure distribution.

D. Surface roughness: the distance destribution

The precious formula's calculate the force as a function of distance. However, in practice the distance between two planes variate due to surface roughness as seen figure D.1. Therefore, the mean distance needs to be determined based on a model and or measurements. Furthermore, if load is applied the asperities of the layers deform thus altering the distance. This variation must be taken into account.

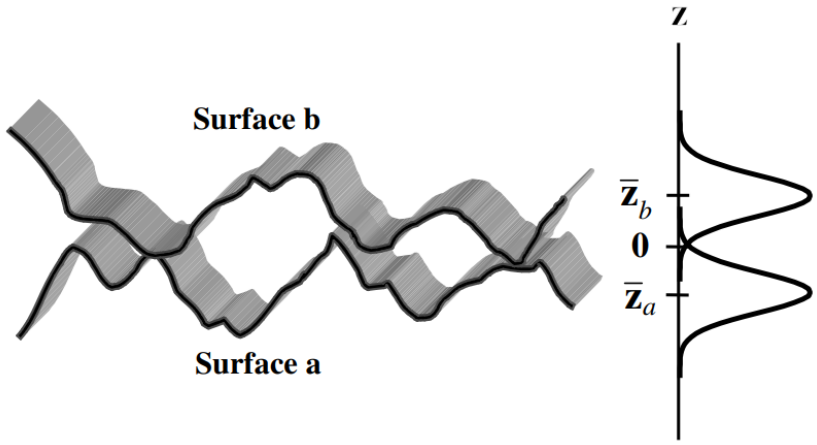

Figure D.1: Modeling surface roughness between two parallel plates. [80]

D.1. Gaussian approximation

With the configuration of figure D.1, the height is modeled as a Gaussian distribution function. This probability function models the surface roughness to quantify the expected distance between the surfaces. This results in a probability function seen in equation (D.1) between the two plates. The formula is equated based on a probability function h_a for surface A, and h_b for surface B. This results in the distribution between the two surfaces.

$$h_{ab}(z, \bar{z}_a + \bar{z}_b) = \frac{1}{\sqrt{2\pi(\sigma_a^2 + \sigma_b^2)}} \, ^{-\frac{(z-(\bar{z}_a+\bar{z}_b))^2}{2(\sigma_a^2+\sigma_b^2)}} \tag{D.1}$$

In this equation σ is the standard deviation of the respective surface, $\bar{z}$ is the mean distance of a surface and the origin of variable z is the mean height of the lower surface. This Gaussian approximation is nothing more than a crude estimate, therefore taking measurements of the actual roughness is always preferred.

D.2. Roughness measurement

When measuring the surface with a better description of the height can be determined. By measuring a set sample of the area, various sample points can be combined to accurately determine the mean distance of a surface. This results in a discrete determination of the height based on the various sample points, which mean result in the height $\bar{z}$. This experimental determination of the height is stated in equation (D.2).

$$\begin{aligned} \bar{z}_a &= \frac{1}{n} \sum_{N=1}^{n} z_{aN} \\ \bar{z}_b &= \frac{1}{n} \sum_{N=1}^{n} z_{bN} \\ \bar{z}_{ab} &= \bar{z}_a + \bar{z}_b \end{aligned} \tag{D.2}$$

In this formula $\bar{z}_{ab}$ is the mean distance between the two plates, z_{aN}&z_{bN} is a sample height of the respective surfaces measured and N is the sample size taken. By measuring the distance, a much more accurate determination can be made between the various surfaces to accurately determine the distances between the plates. These measurements can be done with an Atomic force microscope (AFM). However, this requires an enormous amount of time. Alternatively, a white light interferometer can be applied to measure the roughness of the surfaces.

D.3. Plasticity

When applying a force on the surfaces, the various asperities can deform, thus resulting in a change in distance. Deformation is either elastic or plastic and is material and load dependent as stated in equation (D.3). The plasticity is defined as

$$\Psi = \frac{E'}{H}\sqrt{\frac{\sigma_a}{\beta_a}} \tag{D.3}$$

with E' defined as,

$$\frac{1}{E'} = \frac{1-\nu_a^2}{E_a} + \frac{1-\nu_b^2}{E_b} \tag{D.4}$$

and with Ψ being the plasticity index as defined by Greenwood and Williamson [86], E is the Young's modulus of the material, H is the hardness of the softer material of the two contacting surfaces,ν is the Poisson's ratio of the material, σ is the RMS value of the asperity heights based on the Gaussian distribution and β is the asperity radius [87].
With the AFM the radius can be determined accurately. Additionally, the RMS value of a surface (σ), can be substituted for the mean distance as measured by the AFM. Thus resulting in the following equation.

$$\Psi = \frac{E'}{H}\sqrt{\frac{\bar{z}_{ab}}{\beta}} \tag{D.5}$$

E. Formula's & derivations

E.1. Suction pressure

$$P_s = \frac{-a + \sqrt{A^2 + 4B}}{2} \tag{E.1}$$

$$A = \frac{V_0}{C} - P_i \tag{E.2}$$

$$B = \frac{P_0 v_0}{C} \tag{E.3}$$

$$C = \frac{\pi\left(1-\nu^2\right)a^6}{16Et^3} \tag{E.4}$$

$$\tag{E.5}$$

Combining equation (E.5) results in,

$$P_s(P_i, t, h, a) = \frac{P_i}{2} + \frac{\sqrt{\left(P_i + \frac{16\,\mathrm{E}\,h\,t^3}{a^4\left(\nu^2-1\right)}\right)^2 - \frac{64\,\mathrm{E}\,P_0\,h\,t^3}{a^4\left(\nu^2-1\right)}}}{2} + \frac{8\,\mathrm{E}\,h\,t^3}{a^4\left(\nu^2-1\right)} \tag{E.6}$$

which is equal to equation (4.2). This formula is used for the calculations, as it completely describes the pressure variations as a result of induced pressure changes. Simplifying this equation and assuming P_s and P_i remain constant results into

$$P_s = \frac{V_0}{C} = \frac{16Et^3h}{(1-\nu^2)a^4} \tag{E.7}$$

which is equal to equation (3.6) according to the research of T. Tomokazu [39].

E.1.1. Initial volume

$$\int_0^{\omega_{max}} \pi * r^2(w_{V_0}, P_i)\, d\omega_{V_0} = \pi a^2 h = V_0 \tag{E.8}$$

$$r(\omega_{V_0}, P_i) = \sqrt{\sqrt{\frac{\omega_{V_0} 16Et^3}{\pi(1-\nu^2)(P_0-P_i)}} + a^2} \tag{E.9}$$

$$\omega_{max} = \frac{\pi\left(1-\nu^2\right)\left(P_0-P_i\right)a^4}{16\,E\,t^3} \tag{E.10}$$

$$V_0 = -\frac{a^4\,(\nu-1)\,\pi^2\,(\nu+1)\left(\frac{3a^2}{2} + \sqrt{\frac{(\nu^2-1)(P_0-P_i)a^4}{\nu(P_0-P_i)^2-1}}\right)\left(P_0-P_i\right)}{24t^3E} = \pi a^2 h \tag{E.11}$$

F. Numerical model figures

F.1. Suction pressure - laminate release

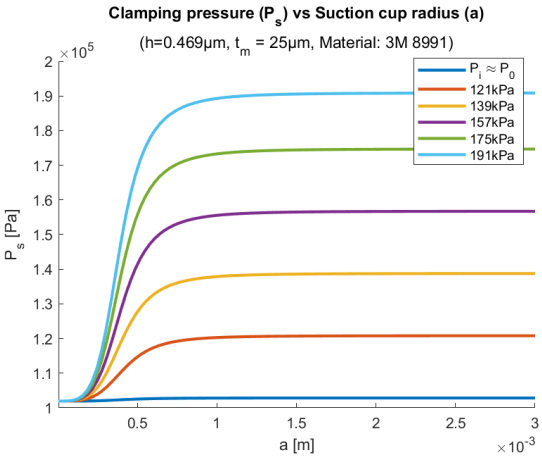

(a) Suction pressure (P_s) vs Suction cup radius (a).

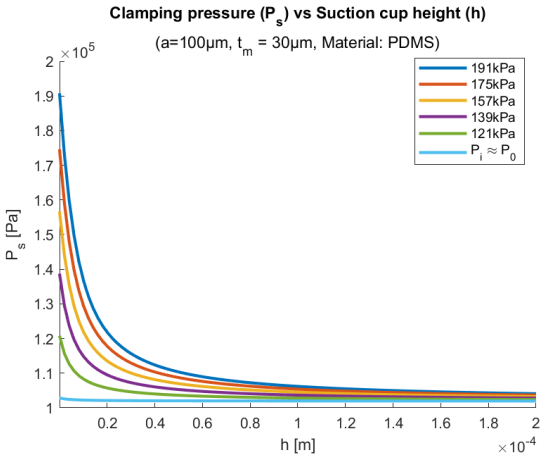

(b) Suction pressure (P_s) vs Suction cup height (h).

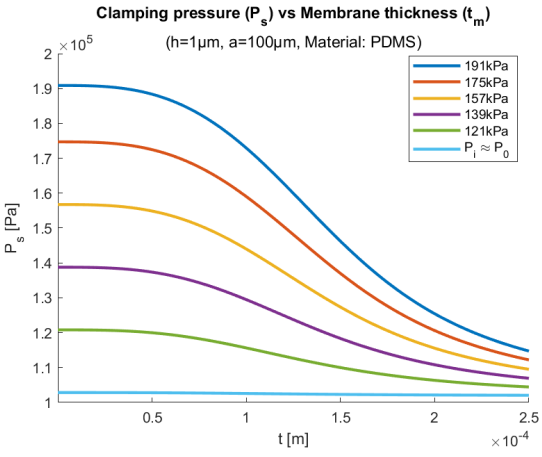

(c) Suction pressure (P_s) vs membrane thickness (t_m).

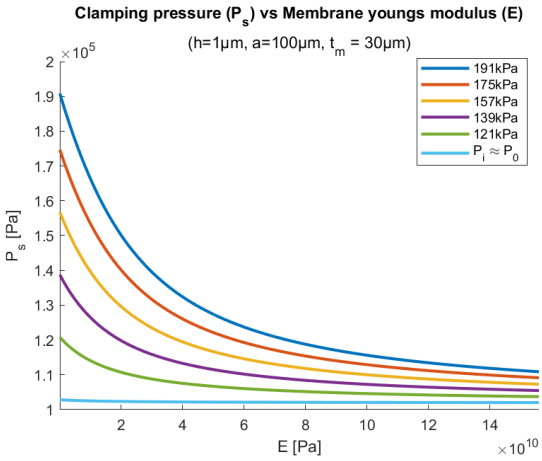

(d) Suction pressure (P_s) vs Modulus of elasticity (E).

Figure F.1: Indication of the influence of the independent design variables on the suction pressure. The variating lines are various induced pressures applied. Atmospheric pressure: $P_0 \approx 102\,\text{kPa}$

F.2. Deformation - laminate release

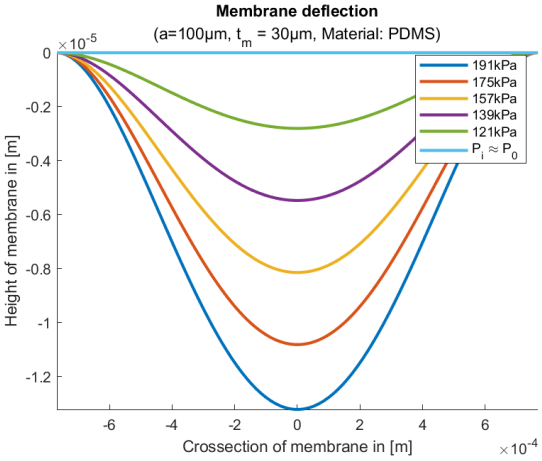

(a) PDMS membrane cross-section of deflection.

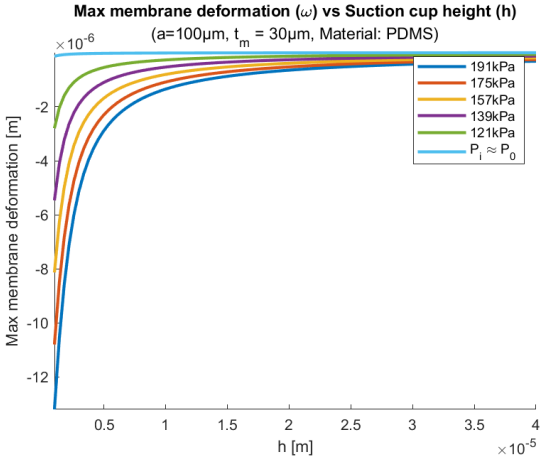

(b) Max deformation (ω) vs Suction cup height (h).

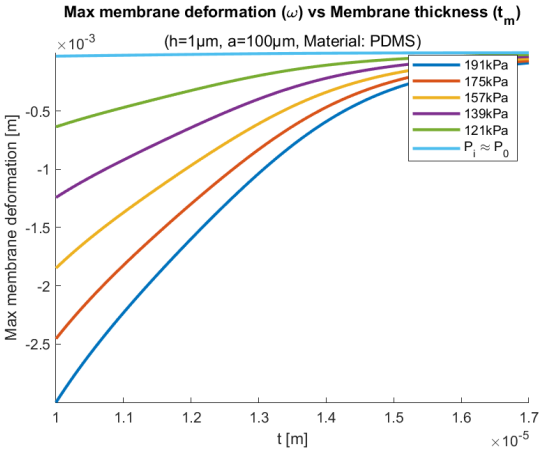

(c) Max deformation (ω) vs membrane thickness (t_m).

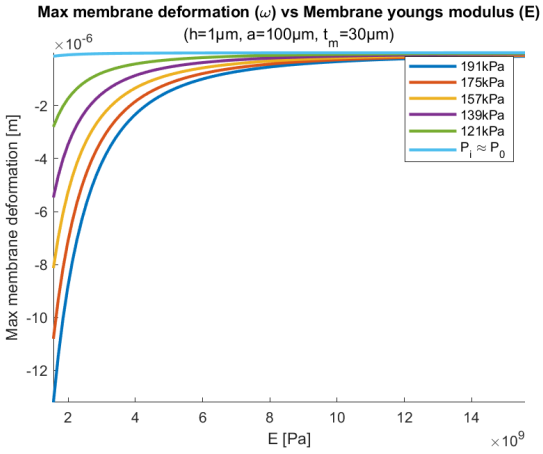

(d) Max deformation (ω) vs Modulus of elasticity (E).

Figure F.2: Indication of the influence of the independent design variables on the yield stress. The variating lines are various induced pressures applied. Atmospheric pressure: $P_0 \approx 102\,\text{kPa}$

F.3. Yield stress - laminate release

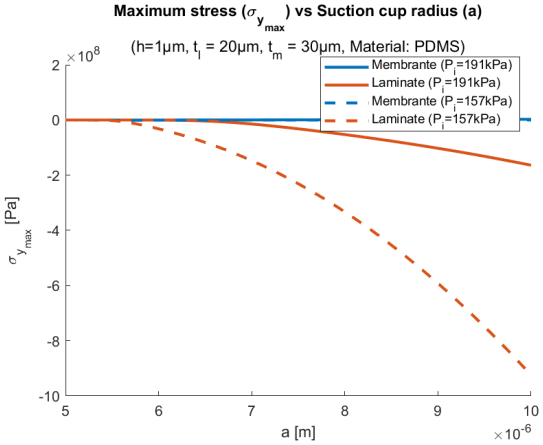

(a) Suction pressure (P_s) vs Suction cup radius (a).

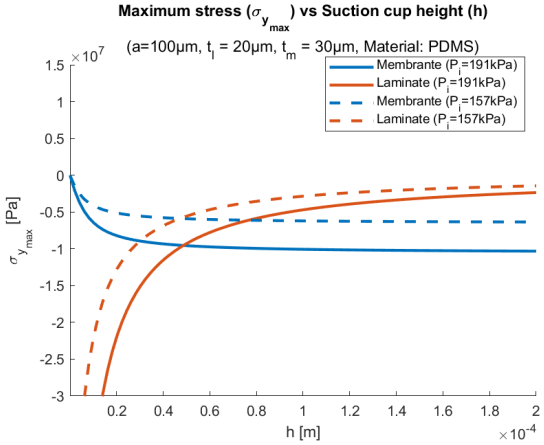

(b) Suction pressure (P_s) vs Suction cup height (h).

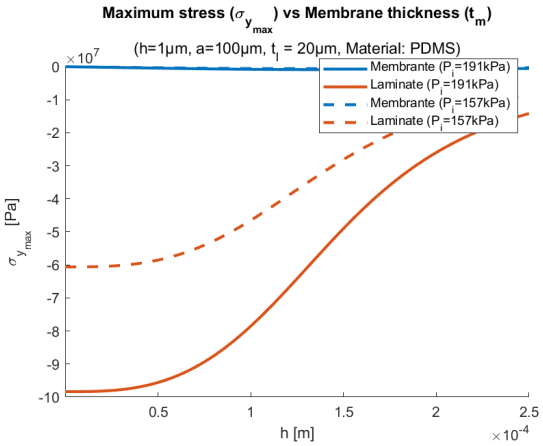

(c) Suction pressure (P_s) vs membrane thickness (t_m).

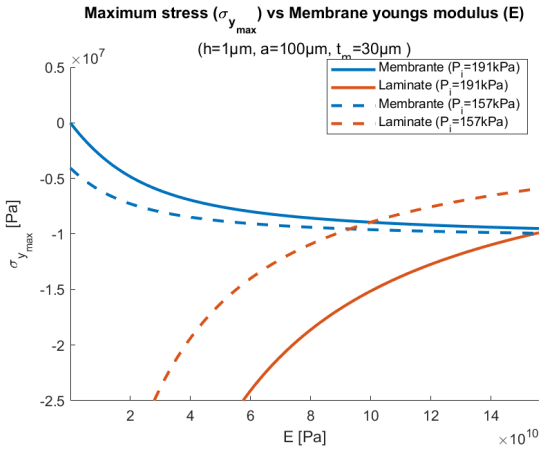

(d) Suction pressure (P_s) vs Modulus of elasticity (E).

Figure F.3: Indication of the influence of the independent design variables on the yield stress. The variating lines are various induced pressures applied. Atmospheric pressure: $P_0 \approx 102\,\text{kPa}$

G. End-effector dimensions

G.1. Vacuum casing

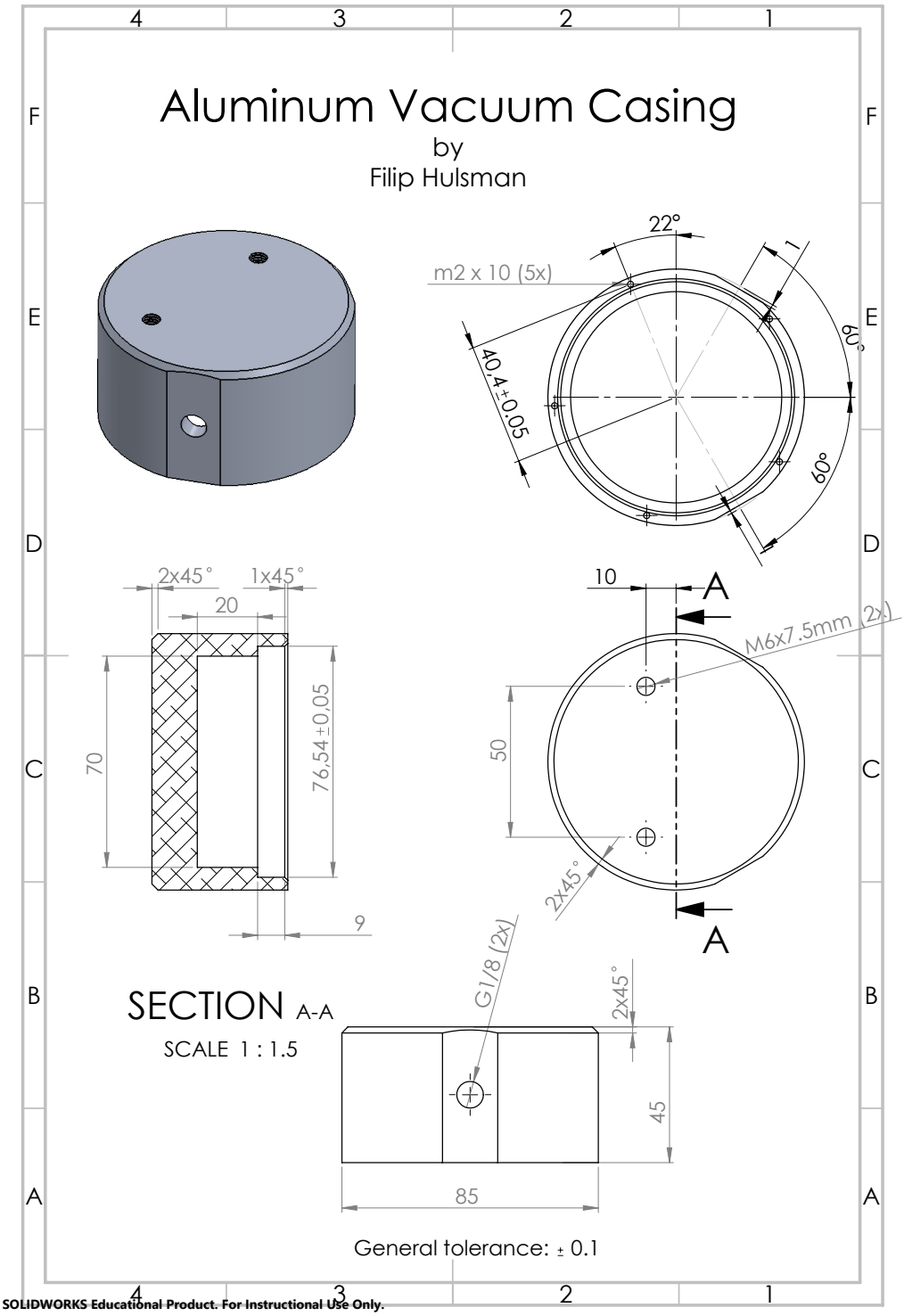

G.2. Membrane scaffold

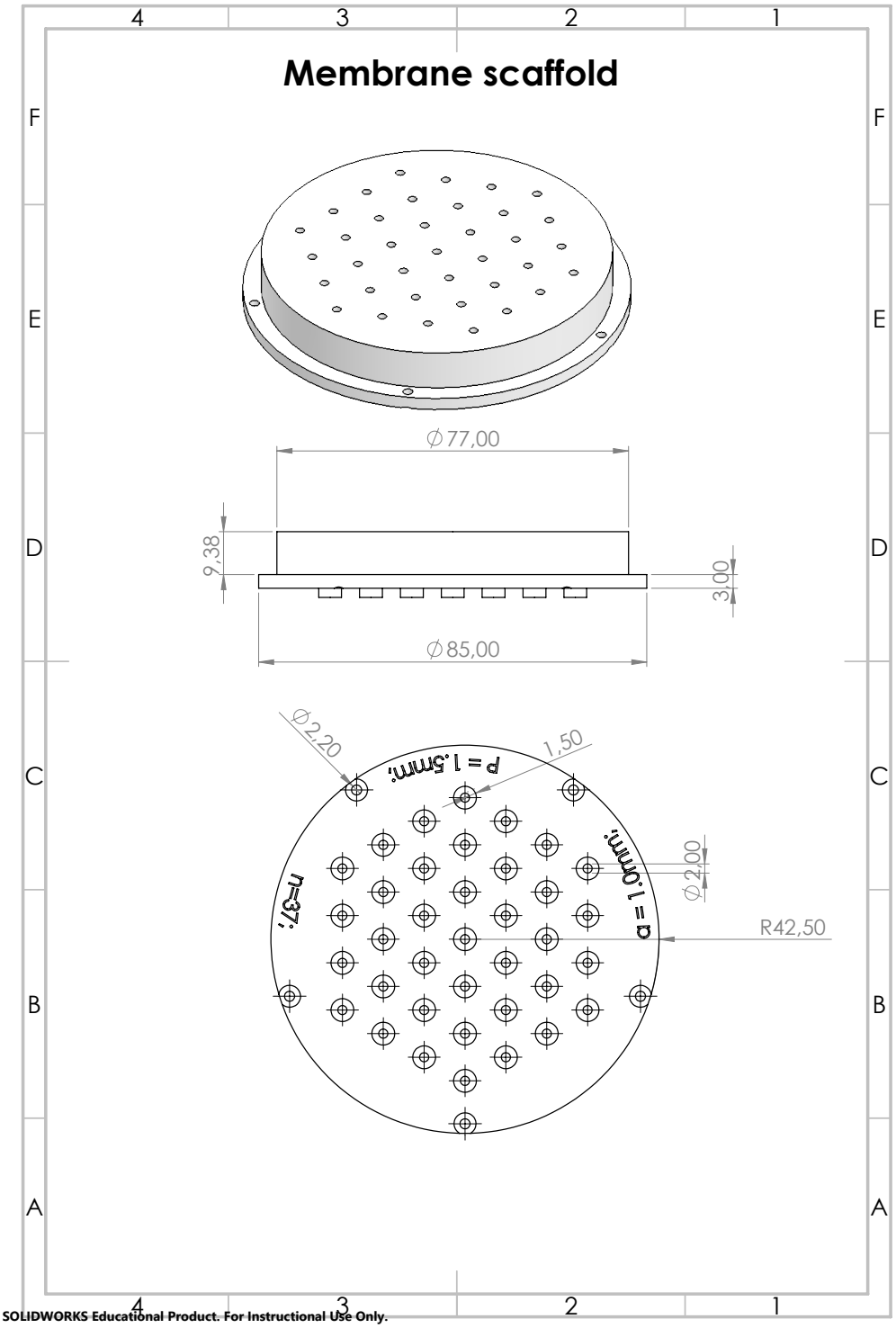

G.3. Preferred membrane

Variable	Symbol	Value
Design variables		
Young's Modulus	E_{PDMS}	360 - 850 kPa [41]
Yield strength	σ_y	700 kPa [88]
Poisson ratio	ν_{PDMS}	0.5 [89]
Density	ρ_{PDMS}	0.97 kg/m^3 [89]
Hydrophobicity	-	Highly hydrophobic contact angle 90-120° [41]

Table G.1: Overviews of the main variables.

H. Experiment Results

H.1. Tensile tests

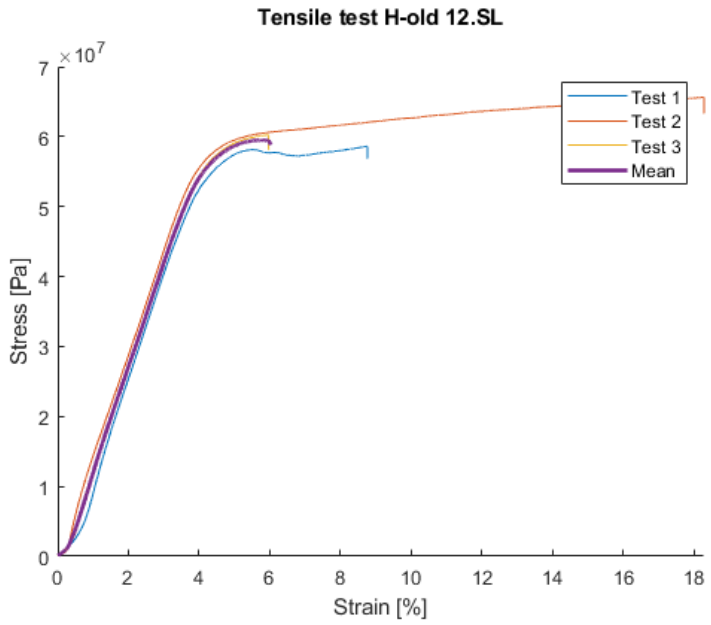

Figure H.1: Tensile test measurements of H-old 12.SL. Samples are pieces of membrane attached to the claw, each with a width of 50 mm.

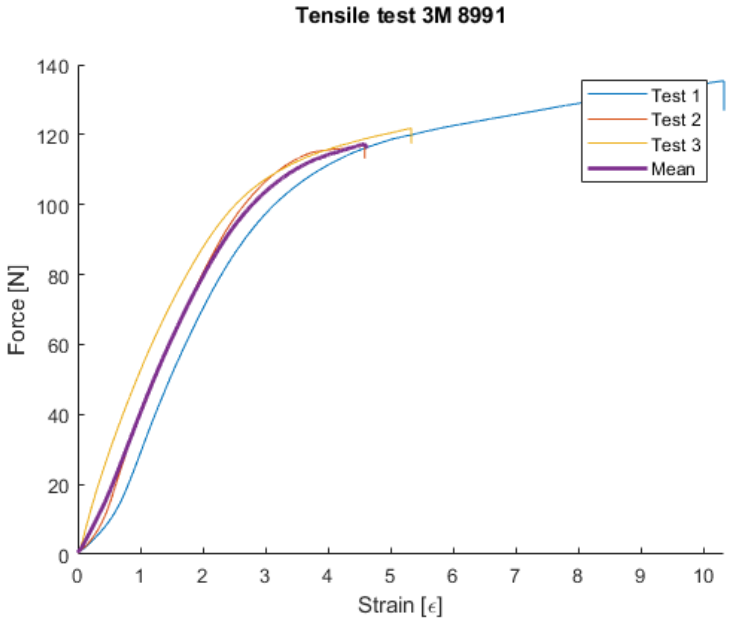

Figure H.2: Tensile test measurements of 3M 8991. Samples are pieces of membrane attached to the claw, each with a width of 50 mm.

H.2. Membrane thickness

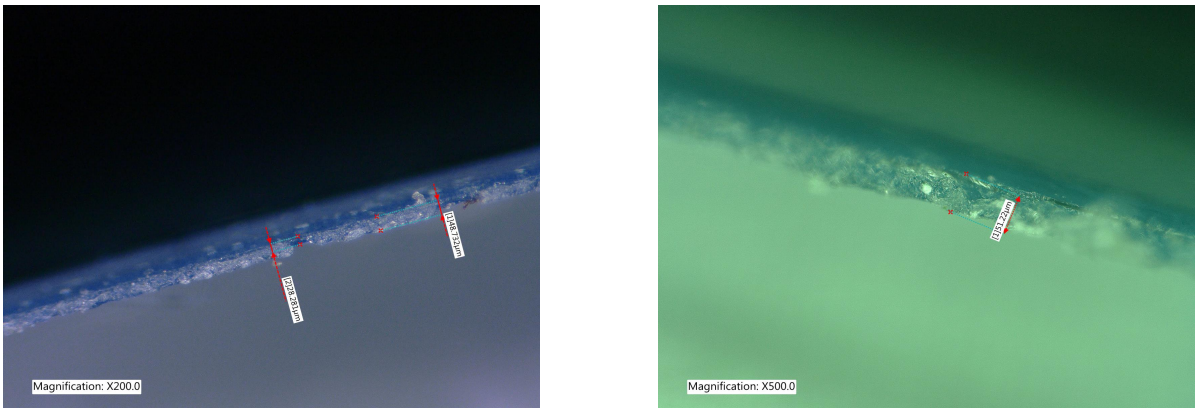

Figure H.3: Keynes VHX 6000 thickness measurement of the 3M 8991 tape.

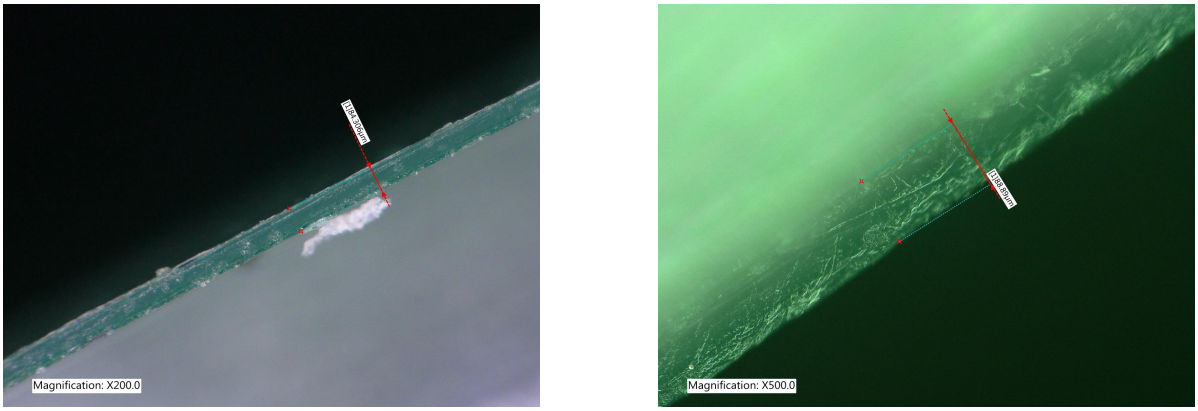

Figure H.4: Keynes VHX 6000 thickness measurement of the H-old 12.SL tape.

H.3. Experiment 1: Deformation

H.3.1. Edge-analysis

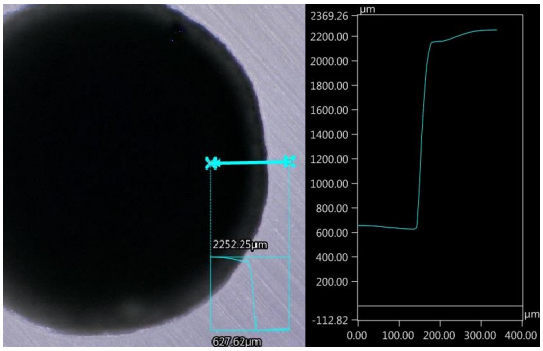

(a) Polished membrane edge radius.

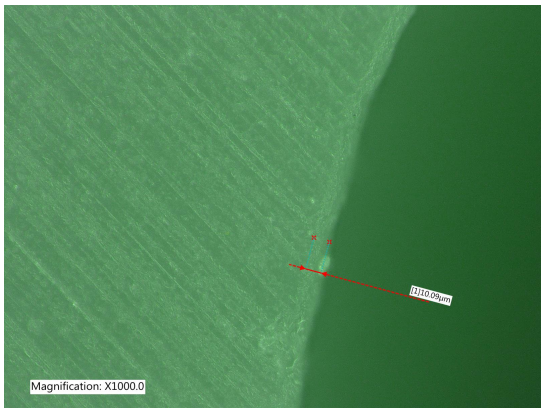

(b) Polished membrane edge width.

Figure H.5: Polished edge of membrane scaffold. Edge width and radius are much smaller compared to the unpolsihed scaffold.

H.3.2. Deformation datasets

Unpolished vs Polished

Experiment	Radius	13 kPa	40 kPa	70 kPa
1	763	24	25	19
2	780	26	21	16
3	760	23	21	11
Average	768	24	21	13
Modelled value	-	24	17	8
Absolute error		0	3	4
Relative error	-	0%	19%	39%

Table H.1: Unpolished deformation results. Deformation is measured with Keynes VHX 6000 microscope [59] and are the deformation created compared to the deformation at P_0.

Experiment	Radius	13 kPa	40 kPa	70 kPa
1	735	21	8	5
2	752	24	12	5
3	735	24	17	6
Average	741	23	12	5
Modelled value	-	21	14	7
Absolute error		2	2	2
Relative error	-	9%	14%	29%

Table H.2: Polished deformation results. Deformation is measured with Keynes VHX 6000 microscope [59] and are the deformation created compared to the deformation at P_0.

H.4. Experiment 2: Force generation

H.4.1. Initial deformation

Radius [µm] / Max deformation [µm]	Measurement: 1	Measurement: 2	Measurement: 3	Measurement: 4
0.7	1436	1462	1464	1484
	20	17	15	12
1.0	1882	1880	1876	1930
	35	31	30	30
1.3	2541	2530	2520	2550
	60	75	44	60
3.0	5823	5801	5786	5769
	89	81	105	130

Table H.3: Initial deformation and radius of suction cups at atmospheric pressure.

H.4.2. Force experiment

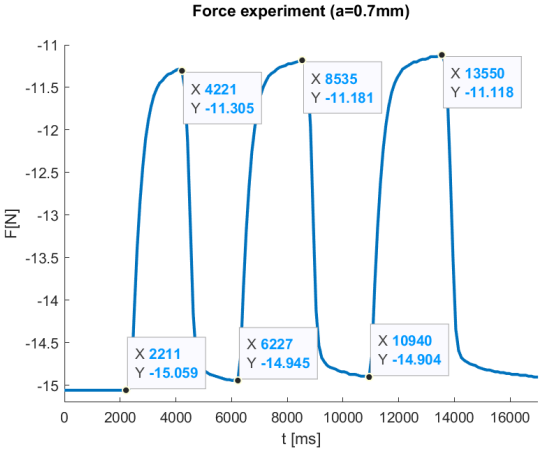

(a) Suction cup radius: a=0.7 mm

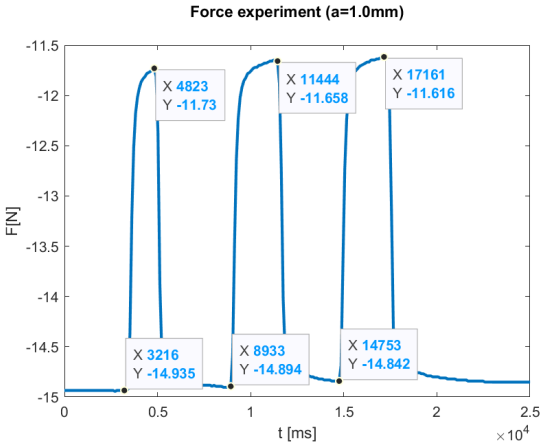

(b) Suction cup radius: a=1.0 mm

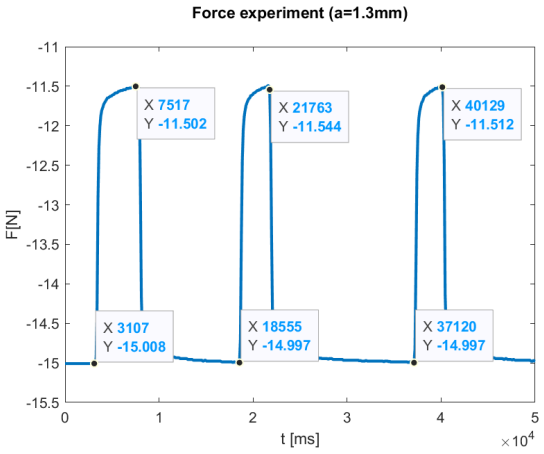

(c) Suction cup radius: a=1.3 mm.

Figure H.6: Force generated with an applied pre-load of 15 N. Load per suction cup: 0.41 N.

	0.7 mm	1.0 mm	1.3 mm	3.0 mm
5 N	1.08 N	0.75 N	1.17 N	1.49 N
10 N	2.25 N	1.55 N	-	-
15 N	3.63 N	3.23 N	6.76 N	4.3 N
20 N	4.08 N	3.42 N	-	-
30 N	Error	6.17 N	9.86 N	11.94 N
45 N	Error	6.81 N	10.96 N	13.53 N
50 N	Error	6.96 N	11.03 N	13.92 N

Table H.4: Force generated for the four samples at variating pre-loads with their sealing performance in brackets. The sealing performance is relative to the expected numerical results, considering the pre-deformation of the membrane and the deformation of the silicone surface, based on the results in appendix H.4.1 & appendix H.4.2.

Figure H.7: Image representation of the discrepancies in the sealing performance of the suction cups. Applied pre-load » 50 N.

H.4.3. Pre-load defection

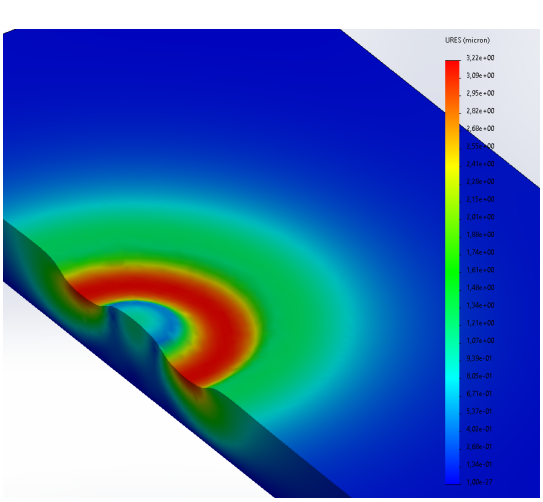

(a) Suction cup radius: a=1.0 mm.

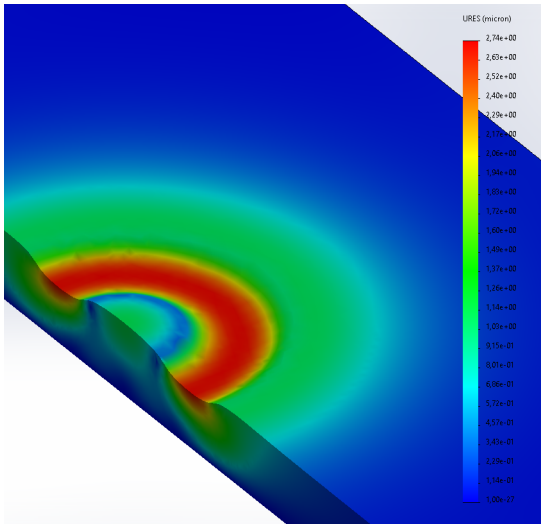

(b) Suction cup radius: a=1.3 mm.

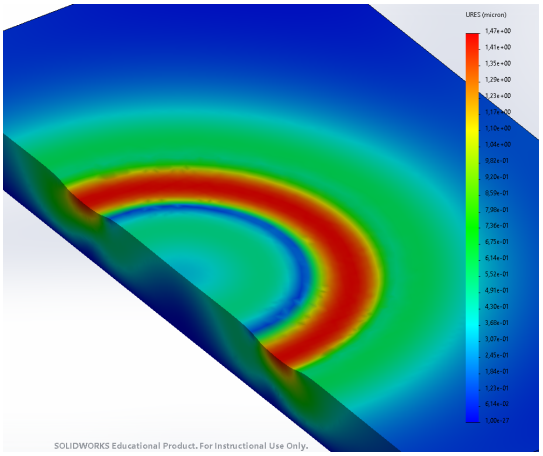

(c) Suction cup radius: a=3.0 mm.

Figure H.8: Deformation of silicone carrier material due to the applied pre-load of 15 N. Load per suction cup: 0.41 N.

I. Matlab model

```
%Dimensionalisation of the suction cups
clc
clear all
%% *System variables*

u = symunit;

%-------------------------------------------------------------------------
%THE CONSTANTS
%-------------------------------------------------------------------------
%General constants
%-------------------------------------------------------------------------
g = vpa(9.81*u.m/u.s^2); % gravity
A_S = 49 * 10^-4*u.m^2; %Area of sheets (7x7cm)
c = 299792458*u.m/u.s; %Speed of light
h_p = 6.62607015*10^-34*u.J*u.s; %constante van plank
T = 293; %Roomtemperature in kelvin
R = 8.314; %Gas constant
i_l= 200; %Length
H_r = linspace(0,1,i_l); %Relative humidty per percentage
v_w = 1.8 *10^-5; %Liquid molar volum of water
%-------------------------------------------------------------------------
%Copper material constants
E_c = 115*10^9*u.kg*u.m/u.s^2/u.m^2; %Youngsmodulus
rho_c = 8.89*10^3*u.kg/u.m^3;%Density
t_c = 20*10^-6*u.m; %Copper sheet thickness
v_c = 0.34; %Poisson factor
z_c = 0.045*10^-6*u.m; %mean estimate distance  (R_a value of surface roughness)
Ham_c = 28.3 * 10 ^-20*u.J;% Hamaker constant
c_Ac = 86; %Contact angle - hydrophobicity
s_yc = 206*10^6*u.kg*u.m/u.s^2/u.m^2; %Yield stress
%-------------------------------------------------------------------------
%TPU material constants
E_tpu = 2.5*10^6*u.kg*u.m/u.s^2/u.m^2; %Youngsmodulus
rho_tpu = 1.12*10^3*u.kg/u.m^3;%Density
t_tpu = 20*10^-6*u.m; %TPU sheet thickness
v_tpu = 0.48; %Poisson factor
z_tpu = 0.047*10^-6*u.m; %mean estimate distance  (R_a value of surface roughness)
A_tpu = 1.3 * 10 ^-20*u.J; % Hamaker constant
c_Atpu = 99.5; %Contact angle - hydrophobicity
s_ytpu = 40*10^6*u.kg*u.m/u.s^2/u.m^2; %Yield stress
%-------------------------------------------------------------------------
%membrane material constants --> Polyester is de praktijk
%E_MEM= 2332937500*u.kg*u.m/u.s^2/u.m^2; %H-old12.SL
E_MEM=    1.5587e+09*u.kg*u.m/u.s^2/u.m^2; %3M 8991 61Âµm
%E_MEM = 3.1174e+09*u.kg*u.m/u.s^2/u.m^2; %3M 8991 25Âµm
v_MEM = 0.48; %Poisson factor
c_AMEM = 79 ; %Contact angle - hydrophobicity
z_MEM = 120*10^-9*u.m; %mean estimate distance  (R_a value of surface roughness)
s_yMEM = 138*10^6*u.kg*u.m/u.s^2/u.m^2; %Yield stress
%-------------------------------------------------------------------------
%preferred membrane constants - PDMS
%membrane material constants --> Polyester is de praktijk
% E_MEM=  605*10^3*u.kg*u.m/u.s^2/u.m^2; %Youngsmodulus
% v_MEM = 0.5; %Poisson factor
% c_AMEM = 105 ; %Contact angle - hydrophobicity
% z_MEM = 120*10^-9*u.m; %mean estimate distance  (R_a value of surface roughness)
% s_yMEM = 700*10^3*u.kg*u.m/u.s^2/u.m^2; %Yield stress

%Carrier material
E_alu = 7.4*10^10*u.kg*u.m/u.s^2/u.m^2; %Youngsmodulus
rho_alu = 2.80*10^3*u.kg/u.m^3;%Density
v_alu = 0.33; %Poisson factor
```

```
z_alu = 3.2*10^-6*u.m; %mean estimate distance  (R_a value of surface roughness)
A_alu = 15 * 10 ^-20*u.J; % Hamaker constant
c_Aalu = 97; %Contact angle - hydrophobicity
s_yalu = 1.05*10^8*u.kg*u.m/u.s^2/u.m^2; %Yield stress
V_00 = 1.33*10^6*10^-18*u.m^3;


%-------------------------------------------------------------------------
% DESIGN VARIABLES
%-------------------------------------------------------------------------
syms r
r = r*u.m;
N_p = 37; %Amount of suction cups
a =500*10^-6*u.m; %Radius of suction cups
p_scm = 1.5*10^-3*u.m; %outer radius of suction cup walls
p_sv = linspace(a,2*p_scm,100); %vector of changing wall thickness
A_f = (p_sv.^2-a^2)*pi; % Singular suction cup flat contact surface
Pl = 101939;%Atmospheric pressure
P0 = Pl*u.kg*u.m/u.s^2/u.m^2; %Units of Atmospheric pressure
h = 0.469e-06*u.m; %Initial height of sealing space
%h = vpa(V_00/(pi*a^2)); %measured height
t_PET = 25*10^-6*u.m; %Thickness of membrane
P_im = 13*10^3* u.kg/u.s^2/u.m %miniÂţmm induced pressure by vacuum pump
%-------------------------------------------------------------------------
%start vectors and length
%-------------------------------------------------------------------------
 n=100;
  P_i = linspace(P_im,2*P0-P_im,100);
  P_i_w = [P_i(1),P_i(11),P_i(21),P_i(31),P_i(41),P_i(51)];

  r = linspace(-a,a,n);
rp = separateUnits(r);
V_0_v = linspace(0*u.m^3,pi*(1000*10^-6)^2*1*10^-6*u.m^3,100);
%% *Pre-defecltion: Membrane movement and initial pressure*

%MEMBRANE pre suction for desired volume change
%-------------------------------------------------------------------------

syms w_V0
n_er =500;
n0 = linspace(0, n_er,n_er);
P_iv0 = linspace(P0, P_im,n_er);
V_0 = pi*h*a^2; %2D equal


 n1 = round(linspace(1,n_er,10));
for k=1:10
rv0(k) = sqrt(sqrt(w_V0*16*E_MEM*t_PET^3  /  ( pi*(1-v_MEM^2)*(P0-P_iv0(n1(k))))+a^2);
wmax(k) = vpa(pi*(1-v_MEM^2)/(16*E_MEM*t_PET^3)*(P0-P_iv0(n1(k)))*a^4);
Vw = vpa(int((0.5*rv0(k))^2*pi,0,wmax(k)));
DV1(k)=vpa(abs(Vw/V_0-1));
end
[value1, P1] = min(DV1(:));

n2 = round(linspace(n1(P1-1),n1(P1+1),20));
     for k =1:20
rv02(k) = sqrt(sqrt(w_V0*16*E_MEM*t_PET^3  /  ( pi*(1-v_MEM^2)*(P0-P_iv0(n2(k))))+a^2);
wmax2(k) = vpa(pi*(1-v_MEM^2)/(16*E_MEM*t_PET^3)*(P0-P_iv0(n2(k)))*a^4);
Vw2 = vpa(int((0.5*rv02(k))^2*pi,0,wmax2(k)));
DV2(k)=vpa(abs(Vw2/V_0-1));
     end
[value2, P2] = min(DV2(:));

n3 = round(linspace(n2(P2-1),n2(P2+1),13));
     for k3 =1:10
rv03(k3) = sqrt(sqrt(w_V0*16*E_MEM*t_PET^3  /  ( pi*(1-v_MEM^2)*(P0-P_iv0(n3(k3))))+a^2);
wmax3(k3) = vpa(pi*(1-v_MEM^2)/(16*E_MEM*t_PET^3)*(P0-P_iv0(n3(k3)))*a^4);
Vw3(k3) = vpa(int((0.5*rv03(k3))^2*pi,0,wmax3(k3)));
DV3(k3)=vpa(abs(Vw3(k3)/V_0-1));
     end
[value3, P3] = min(DV3(:));
```

```
error= (vpa(Vw3(k3)/V_0)-1)*100;
S = vpa(P_iv0(n3(P3)))
DS = P0-S;
%Predeflection curve
for k=1:n
    w_V0_plot(k) = separateUnits(pi*(1-v_MEM^2)/(16*E_MEM*t_PET^3)*(P0-S).*(r(k)^2-a^2).^2);
end
%Before contact
figure
hold on
plot(rp,w_V0_plot)
xlim('tight')
title('Pre-deflection of membrane',' ')
xlabel('Crossection of membrane in [m]')
ylabel('Height of membrane in [m]')
ylim([0.0000000 0.0000025])
%% *Suction pressure*
% *Induced pressure*


for k =1:100
    P_s_m(k) = vpa((P_i(k)+DS)/2 + sqrt(((P_i(k)+DS) + (16*E_MEM*h*t_PET^3)/(a^4*(v_MEM^2 - 1)))^2 - (64*E_MEM*P0*h*t_PET^3)/(a^4*(v_MEM^2 - 1)))/2 + (8*E_MEM*h*t_PET^3)/(a^4*(v_MEM^2 - 1)));
    %P_s_tpu(k) = vpa(P_s_m(k)/2 + sqrt((P_s_m(k) + (16*E_tpu*z_tpu*t_tpu^3)/(a^4*(v_tpu^2 - 1)))^2 - (64*E_tpu*P0*z_tpu*t_tpu^3)/(a^4*(v_tpu^2 - 1)))/2 + (8*E_tpu*z_tpu*t_tpu^3)/(a^4*(v_tpu^2 - 1)));
    %P_s_c(k) = vpa(P_s_m(k)/2 + sqrt((P_s_m(k) + (16*E_c*z_c*t_c^3)/(a^4*(v_c^2 - 1)))^2 - (64*E_c*P0*z_c*t_c^3)/(a^4*(v_c^2 - 1)))/2 + (8*E_c*z_c*t_c^3)/(a^4*(v_c^2 - 1)));
    S_PET_max(k) = 0.75*(P_s_m(k)-P_i(k))*a^2/t_PET^2;
    S_tpu_max(k) = 0.75*(P0-P_s_m(k))*a^2/t_tpu^2;
    S_c_max(k) = 0.75*(P0-P_s_m(k))*a^2/t_c^2;
end
%Figuur 1a - Change of induced presure
%-------------------------------------
figure
hold on
plot(separateUnits(P_i),separateUnits(P_s_m),'-')
%plot(separateUnits(P_i),separateUnits(P_s_c))
%plot(separateUnits(P_i),separateUnits(P_s_tpu),'--')

xlim('tight')
title('Max clamping pressure (P_s) vs Induced pressure (P_i)',' ')
xlabel('P_i [Pa]')
ylabel('P_s [Pa]')
%legend('Only PET','PET + Copper', 'PET + Polyurethane','Location','northeastoutside')
%%
% *Radius*

as = linspace(5*10^-6*u.m,3*10^-3*u.m,100);
for k =1:n
    P_s_ma1(k) = vpa((P_i_w(1))/2 + sqrt(((P_i_w(1)) + (16*E_MEM*h*t_PET^3)/(as(k)^4*(v_MEM^2 - 1)))^2 - (64*E_MEM*P0*h*t_PET^3)/(as(k)^4*(v_MEM^2 - 1)))/2 + (8*E_MEM*h*t_PET^3)/(as(k)^4*(v_MEM^2 - 1)))
        ;
    P_s_ma2(k) = vpa((P_i_w(2))/2 + sqrt(((P_i_w(2)) + (16*E_MEM*h*t_PET^3)/(as(k)^4*(v_MEM^2 - 1)))^2 - (64*E_MEM*P0*h*t_PET^3)/(as(k)^4*(v_MEM^2 - 1)))/2 + (8*E_MEM*h*t_PET^3)/(as(k)^4*(v_MEM^2 - 1)))
        ;
    P_s_ma3(k) = vpa((P_i_w(3))/2 + sqrt(((P_i_w(3)) + (16*E_MEM*h*t_PET^3)/(as(k)^4*(v_MEM^2 - 1)))^2 - (64*E_MEM*P0*h*t_PET^3)/(as(k)^4*(v_MEM^2 - 1)))/2 + (8*E_MEM*h*t_PET^3)/(as(k)^4*(v_MEM^2 - 1)))
        ;
    P_s_ma4(k) = vpa((P_i_w(4))/2 + sqrt(((P_i_w(4)) + (16*E_MEM*h*t_PET^3)/(as(k)^4*(v_MEM^2 - 1)))^2 - (64*E_MEM*P0*h*t_PET^3)/(as(k)^4*(v_MEM^2 - 1)))/2 + (8*E_MEM*h*t_PET^3)/(as(k)^4*(v_MEM^2 - 1)))
        ;
    P_s_ma5(k) = vpa((P_i_w(5))/2 + sqrt(((P_i_w(5)) + (16*E_MEM*h*t_PET^3)/(as(k)^4*(v_MEM^2 - 1)))^2 - (64*E_MEM*P0*h*t_PET^3)/(as(k)^4*(v_MEM^2 - 1)))/2 + (8*E_MEM*h*t_PET^3)/(as(k)^4*(v_MEM^2 - 1)))
        ;
    P_s_ma6(k) = vpa((P_i_w(6))/2 + sqrt(((P_i_w(6)) + (16*E_MEM*h*t_PET^3)/(as(k)^4*(v_MEM^2 - 1)))^2 - (64*E_MEM*P0*h*t_PET^3)/(as(k)^4*(v_MEM^2 - 1)))/2 + (8*E_MEM*h*t_PET^3)/(as(k)^4*(v_MEM^2 - 1)))
        ;

    S_PET_maxa1(k) = 0.75*(P_s_ma1(k)-P_i(1))*as(k)^2/t_PET^2;
    S_c_maxa1(k) = 0.75*(P0-P_s_ma1(k))*as(k)^2/t_c^2;

```

```
191     S_PET_maxa3(k) = 0.75*(P_s_ma3(k)-P_i_w(3))*as(k)^2/t_PET^2;
192     S_c_maxa3(k) = 0.75*(P0-P_s_ma3(k))*as(k)^2/t_c^2;
193 end
194
195 %Figuur 2a - Change of suctioncup radius
196 %---------------------------------------
197 figure
198 hold on
199 plot(separateUnits(as),separateUnits(P_s_ma1),'LineWidth',2)
200 plot(separateUnits(as),separateUnits(P_s_ma2),'LineWidth',2)
201 plot(separateUnits(as),separateUnits(P_s_ma3),'LineWidth',2)
202 plot(separateUnits(as),separateUnits(P_s_ma4),'LineWidth',2)
203 plot(separateUnits(as),separateUnits(P_s_ma5),'LineWidth',2)
204 plot(separateUnits(as),separateUnits(P_s_ma6),'LineWidth',2)
205 xlim('tight')
206 title('Clamping pressure (P_s) vs Suction cup radius (a)',' ')
207 subtitle('(h=0.469Âţm, t_m = 25Âţm, Material: 3M 8991)')
208 xlabel('a [m]')
209 ylabel('P_s [Pa]')
210 legend('13kPa', '31kPa', '49kPa', '67kPa', '85kPa', 'P_i \approx P_0')
211 %%
212 as = linspace(5*10^-6*u.m,1*10^-5*u.m,100);
213 figure
214 hold on
215 plot(separateUnits(as),separateUnits(S_PET_maxa1),'Color','#0072BD','LineWidth',2)
216 plot(separateUnits(as),separateUnits(S_c_maxa1),'Color','#D95319','LineWidth',2)
217
218 plot(separateUnits(as),separateUnits(S_PET_maxa3),'--','Color','#0072BD','LineWidth',2)
219 plot(separateUnits(as),separateUnits(S_c_maxa3),'--','Color','#D95319','LineWidth',2)
220
221 xlim('tight')
222 title('Maximum stress (\sigma_{y_{max}}) vs Suction cup radius (a)',' ')
223 subtitle('(h=1Âţm, t_l = 20Âţm, t_m = 30Âţm, Material: PDMS)')
224 xlabel('a [m]')
225 ylabel('\sigma_{y_{max}} [Pa]')
226 legend('Membrante (P_i=13kPa)', 'Laminate (P_i=13kPa)','Membrante (P_i=49kPa)', 'Laminate (P_i=49kPa)')
227 %%
228 %
229 %
230 % *Initial height*
231
232 hh= linspace(1*10^-8*u.m,0.2*10^-3*u.m,100);
233 for k =1:n
234     P_s_mh1(k) = vpa(P_i_w(1)/2 + sqrt((P_i_w(1) + (16*E_MEM*hh(k)*t_PET^3)/(a^4*(v_MEM^2 - 1)))^2 - (64*
          E_MEM*P0*hh(k)*t_PET^3)/(a^4*(v_MEM^2 - 1)))/2 + (8*E_MEM*hh(k)*t_PET^3)/(a^4*(v_MEM^2 - 1)));
235     P_s_mh2(k) = vpa(P_i_w(2)/2 + sqrt((P_i_w(2) + (16*E_MEM*hh(k)*t_PET^3)/(a^4*(v_MEM^2 - 1)))^2 - (64*
          E_MEM*P0*hh(k)*t_PET^3)/(a^4*(v_MEM^2 - 1)))/2 + (8*E_MEM*hh(k)*t_PET^3)/(a^4*(v_MEM^2 - 1)));
236     P_s_mh3(k) = vpa(P_i_w(3)/2 + sqrt((P_i_w(3) + (16*E_MEM*hh(k)*t_PET^3)/(a^4*(v_MEM^2 - 1)))^2 - (64*
          E_MEM*P0*hh(k)*t_PET^3)/(a^4*(v_MEM^2 - 1)))/2 + (8*E_MEM*hh(k)*t_PET^3)/(a^4*(v_MEM^2 - 1)));
237     P_s_mh4(k) = vpa(P_i_w(4)/2 + sqrt((P_i_w(4) + (16*E_MEM*hh(k)*t_PET^3)/(a^4*(v_MEM^2 - 1)))^2 - (64*
          E_MEM*P0*hh(k)*t_PET^3)/(a^4*(v_MEM^2 - 1)))/2 + (8*E_MEM*hh(k)*t_PET^3)/(a^4*(v_MEM^2 - 1)));
238     P_s_mh5(k) = vpa(P_i_w(5)/2 + sqrt((P_i_w(5) + (16*E_MEM*hh(k)*t_PET^3)/(a^4*(v_MEM^2 - 1)))^2 - (64*
          E_MEM*P0*hh(k)*t_PET^3)/(a^4*(v_MEM^2 - 1)))/2 + (8*E_MEM*hh(k)*t_PET^3)/(a^4*(v_MEM^2 - 1)));
239     P_s_mh6(k) = vpa(P_i_w(6)/2 + sqrt((P_i_w(6) + (16*E_MEM*hh(k)*t_PET^3)/(a^4*(v_MEM^2 - 1)))^2 - (64*
          E_MEM*P0*hh(k)*t_PET^3)/(a^4*(v_MEM^2 - 1)))/2 + (8*E_MEM*hh(k)*t_PET^3)/(a^4*(v_MEM^2 - 1)));
240
241     S_PET_maxh1(k) = 0.75*(P_s_mh1(k)-P_i_w(1))*a^2/t_PET^2;
242     S_c_maxh1(k) = 0.75*(P0-P_s_mh1(k))*a^2/t_c^2;
243
244     S_PET_maxh3(k) = 0.75*(P_s_mh3(k)-P_i_w(3))*a^2/t_PET^2;
245     S_c_maxh3(k) = 0.75*(P0-P_s_mh3(k))*a^2/t_c^2;
246 end
247
248
249 figure
250 hold on
251 plot(separateUnits(hh),separateUnits(P_s_mh1),'LineWidth',2)
252 plot(separateUnits(hh),separateUnits(P_s_mh2),'LineWidth',2)
253 plot(separateUnits(hh),separateUnits(P_s_mh3),'LineWidth',2)
254 plot(separateUnits(hh),separateUnits(P_s_mh4),'LineWidth',2)
255 plot(separateUnits(hh),separateUnits(P_s_mh5),'LineWidth',2)
```

```
plot(separateUnits(hh),separateUnits(P_s_mh6),'LineWidth',2)

xlim('tight')
title('Clamping pressure (P_s) vs Suction cup height (h)',' ')
subtitle('(a=100Âţm, t_m = 30Âţm, Material: PDMS)')
xlabel('h [m]')
ylabel('P_s [Pa]')
legend('13kPa', '31kPa', '49kPa', '67kPa', '85kPa', 'P_i \approx P_0')
%%
figure
hold on
plot(separateUnits(hh),separateUnits(S_PET_maxh1),'Color','#0072BD','LineWidth',2)
plot(separateUnits(hh),separateUnits(S_c_maxh1),'Color','#D95319','LineWidth',2)

plot(separateUnits(hh),separateUnits(S_PET_maxh3),'--','Color','#0072BD','LineWidth',2)
plot(separateUnits(hh),separateUnits(S_c_maxh3),'--','Color','#D95319','LineWidth',2)

xlim('tight')
title('Maximum stress (\sigma_{y_{max}}) vs Suction cup height (h)',' ')
subtitle('(a=100Âţm, t_l = 20Âţm, t_m = 30Âţm, Material: PDMS)')
xlabel('h [m]')
ylabel('\sigma_{y_{max}} [Pa]')
legend('Membrante (P_i=13kPa)', 'Laminate (P_i=13kPa)','Membrante (P_i=49kPa)', 'Laminate (P_i=49kPa)')
%%
%
%
% *Membrane thickness*

tt= linspace(1*10^-8*u.m,2.5*10^-4*u.m,100);
for k =1:n
    P_s_mt1(k) = vpa(P_i_w(1)/2 + sqrt((P_i_w(1) + (16*E_MEM*h*tt(k)^3)/(a^4*(v_MEM^2 - 1)))^2 - (64*E_MEM
        *P0*h*tt(k)^3)/(a^4*(v_MEM^2 - 1)))/2 + (8*E_MEM*h*tt(k)^3)/(a^4*(v_MEM^2 - 1)));
    P_s_mt2(k) = vpa(P_i_w(2)/2 + sqrt((P_i_w(2) + (16*E_MEM*h*tt(k)^3)/(a^4*(v_MEM^2 - 1)))^2 - (64*E_MEM
        *P0*h*tt(k)^3)/(a^4*(v_MEM^2 - 1)))/2 + (8*E_MEM*h*tt(k)^3)/(a^4*(v_MEM^2 - 1)));
    P_s_mt3(k) = vpa(P_i_w(3)/2 + sqrt((P_i_w(3) + (16*E_MEM*h*tt(k)^3)/(a^4*(v_MEM^2 - 1)))^2 - (64*E_MEM
        *P0*h*tt(k)^3)/(a^4*(v_MEM^2 - 1)))/2 + (8*E_MEM*h*tt(k)^3)/(a^4*(v_MEM^2 - 1)));
    P_s_mt4(k) = vpa(P_i_w(4)/2 + sqrt((P_i_w(4) + (16*E_MEM*h*tt(k)^3)/(a^4*(v_MEM^2 - 1)))^2 - (64*E_MEM
        *P0*h*tt(k)^3)/(a^4*(v_MEM^2 - 1)))/2 + (8*E_MEM*h*tt(k)^3)/(a^4*(v_MEM^2 - 1)));
    P_s_mt5(k) = vpa(P_i_w(5)/2 + sqrt((P_i_w(5) + (16*E_MEM*h*tt(k)^3)/(a^4*(v_MEM^2 - 1)))^2 - (64*E_MEM
        *P0*h*tt(k)^3)/(a^4*(v_MEM^2 - 1)))/2 + (8*E_MEM*h*tt(k)^3)/(a^4*(v_MEM^2 - 1)));
    P_s_mt6(k) = vpa(P_i_w(6)/2 + sqrt((P_i_w(6) + (16*E_MEM*h*tt(k)^3)/(a^4*(v_MEM^2 - 1)))^2 - (64*E_MEM
        *P0*h*tt(k)^3)/(a^4*(v_MEM^2 - 1)))/2 + (8*E_MEM*h*tt(k)^3)/(a^4*(v_MEM^2 - 1)));


    S_PET_maxt1(k) = 0.75*(P_s_mt1(k)-P_i_w(1))*a^2/tt(k)^2;
    S_c_maxt1(k) = 0.75*(P0-P_s_mt1(k))*a^2/t_c^2;

    S_PET_maxt3(k) = 0.75*(P_s_mt3(k)-P_i_w(3))*a^2/tt(k)^2;
    S_c_maxt3(k) = 0.75*(P0-P_s_mt3(k))*a^2/t_c^2;
end


figure
hold on
plot(separateUnits(tt),separateUnits(P_s_mt1),'LineWidth',2)
plot(separateUnits(tt),separateUnits(P_s_mt2),'LineWidth',2)
plot(separateUnits(tt),separateUnits(P_s_mt3),'LineWidth',2)
plot(separateUnits(tt),separateUnits(P_s_mt4),'LineWidth',2)
plot(separateUnits(tt),separateUnits(P_s_mt5),'LineWidth',2)
plot(separateUnits(tt),separateUnits(P_s_mt6),'LineWidth',2)

xlim('tight')
title('Clamping pressure (P_s) vs Membrane thickness (t_m)',' ')
subtitle('(h=1Âţm, a=100Âţm, Material: PDMS)')
xlabel('t [m]')
ylabel('P_s [Pa]')
legend('13kPa', '31kPa', '49kPa', '67kPa', '85kPa', 'P_i \approx P_0')
%%
figure
hold on
plot(separateUnits(tt),separateUnits(S_PET_maxt1),'Color','#0072BD','LineWidth',2)
```

```
plot(separateUnits(tt),separateUnits(S_c_maxt1),'Color','#D95319','LineWidth',2)

plot(separateUnits(tt),separateUnits(S_PET_maxt3),'--','Color','#0072BD','LineWidth',2)
plot(separateUnits(tt),separateUnits(S_c_maxt3),'--','Color','#D95319','LineWidth',2)

xlim('tight')
title('Maximum stress (\sigma_{y_{max}}) vs Membrane thickness (t_m)',' ')
subtitle('(h=1Âţm, a=100Âţm, t_l = 20Âţm, Material: PDMS)')
xlabel('h [m]')
ylabel('\sigma_{y_{max}} [Pa]')
legend('Membrante (P_i=13kPa)', 'Laminate (P_i=13kPa)','Membrante (P_i=49kPa)', 'Laminate (P_i=49kPa)')
%%
%
%%
%
%
% *Membrane Material*

EE= linspace(E_MEM/100,E_MEM*100,100);
for k =1:n
    P_s_mE1(k) = vpa(P_i_w(1)/2 + sqrt((P_i_w(1) + (16*EE(k)*h*t_PET^3)/(a^4*(v_MEM^2 - 1)))^2 - (64*EE(k)
        *P0*h*t_PET^3)/(a^4*(v_MEM^2 - 1)))/2 + (8*EE(k)*h*t_PET^3)/(a^4*(v_MEM^2 - 1)));
    P_s_mE2(k) = vpa(P_i_w(2)/2 + sqrt((P_i_w(2) + (16*EE(k)*h*t_PET^3)/(a^4*(v_MEM^2 - 1)))^2 - (64*EE(k)
        *P0*h*t_PET^3)/(a^4*(v_MEM^2 - 1)))/2 + (8*EE(k)*h*t_PET^3)/(a^4*(v_MEM^2 - 1)));
    P_s_mE3(k) = vpa(P_i_w(3)/2 + sqrt((P_i_w(3) + (16*EE(k)*h*t_PET^3)/(a^4*(v_MEM^2 - 1)))^2 - (64*EE(k)
        *P0*h*t_PET^3)/(a^4*(v_MEM^2 - 1)))/2 + (8*EE(k)*h*t_PET^3)/(a^4*(v_MEM^2 - 1)));
    P_s_mE4(k) = vpa(P_i_w(4)/2 + sqrt((P_i_w(4) + (16*EE(k)*h*t_PET^3)/(a^4*(v_MEM^2 - 1)))^2 - (64*EE(k)
        *P0*h*t_PET^3)/(a^4*(v_MEM^2 - 1)))/2 + (8*EE(k)*h*t_PET^3)/(a^4*(v_MEM^2 - 1)));
    P_s_mE5(k) = vpa(P_i_w(5)/2 + sqrt((P_i_w(5) + (16*EE(k)*h*t_PET^3)/(a^4*(v_MEM^2 - 1)))^2 - (64*EE(k)
        *P0*h*t_PET^3)/(a^4*(v_MEM^2 - 1)))/2 + (8*EE(k)*h*t_PET^3)/(a^4*(v_MEM^2 - 1)));
    P_s_mE6(k) = vpa(P_i_w(6)/2 + sqrt((P_i_w(6) + (16*EE(k)*h*t_PET^3)/(a^4*(v_MEM^2 - 1)))^2 - (64*EE(k)
        *P0*h*t_PET^3)/(a^4*(v_MEM^2 - 1)))/2 + (8*EE(k)*h*t_PET^3)/(a^4*(v_MEM^2 - 1)));



    S_PET_maxE1(k) = 0.75*(P_s_mE1(k)-P_i_w(1))*a^2/t_PET^2;
    S_c_maxE1(k) = 0.75*(P0-P_s_mE1(k))*a^2/t_tpu^2;

    S_PET_maxE3(k) = 0.75*(P_s_mE3(k)-P_i_w(1))*a^2/t_PET^2;
    S_c_maxE3(k) = 0.75*(P0-P_s_mE3(k))*a^2/t_tpu^2;
end


figure
hold on
plot(separateUnits(EE),separateUnits(P_s_mE1),'LineWidth',2)
plot(separateUnits(EE),separateUnits(P_s_mE2),'LineWidth',2)
plot(separateUnits(EE),separateUnits(P_s_mE3),'LineWidth',2)
plot(separateUnits(EE),separateUnits(P_s_mE4),'LineWidth',2)
plot(separateUnits(EE),separateUnits(P_s_mE5),'LineWidth',2)
plot(separateUnits(EE),separateUnits(P_s_mE6),'LineWidth',2)

xlim('tight')
title('Clamping pressure (P_s) vs Membrane youngs modulus (E)',' ')
subtitle('(h=1Âţm, a=100Âţm, t_m = 30Âţm)')
xlabel('E [Pa]')
ylabel('P_s [Pa]')
legend('13kPa', '31kPa', '49kPa', '67kPa', '85kPa', 'P_i \approx P_0')
%%
figure
hold on
plot(separateUnits(EE),separateUnits(S_PET_maxE1),'Color','#0072BD','LineWidth',2)
plot(separateUnits(EE),separateUnits(S_c_maxE1),'Color','#D95319','LineWidth',2)

plot(separateUnits(EE),separateUnits(S_PET_maxE3),'--','Color','#0072BD','LineWidth',2)
plot(separateUnits(EE),separateUnits(S_c_maxE3),'--','Color','#D95319','LineWidth',2)

xlim('tight')
title('Maximum stress (\sigma_{y_{max}}) vs Membrane youngs modulus (E)',' ')
subtitle('(h=1Âţm, a=100Âţm, t_m=30Âţm )')
xlabel('E [Pa]')
```

```
ylabel('\sigma_{y_{max}} [Pa]')
legend('Membrante (P_i=13kPa)', 'Laminate (P_i=13kPa)','Membrante (P_i=49kPa)', 'Laminate (P_i=49kPa)')

%%
%% *Only membrane deformation*
% *Cross*

for k=1:n
wplot_m1(k) = separateUnits(pi*(1-v_MEM^2)/(16*E_MEM*t_PET^3)*(P0 - P_i_w(1)).*(r(k)^2-a^2).^2); %PET Membrane
wplot_m2(k) = separateUnits(pi*(1-v_MEM^2)/(16*E_MEM*t_PET^3)*(P0 - P_i_w(2)).*(r(k)^2-a^2).^2); %PET Membrane
wplot_m3(k) = separateUnits(pi*(1-v_MEM^2)/(16*E_MEM*t_PET^3)*(P0 - P_i_w(3)).*(r(k)^2-a^2).^2); %PET Membrane
wplot_m4(k) = separateUnits(pi*(1-v_MEM^2)/(16*E_MEM*t_PET^3)*(P0 - P_i_w(4)).*(r(k)^2-a^2).^2); %PET Membrane
wplot_m5(k) = separateUnits(pi*(1-v_MEM^2)/(16*E_MEM*t_PET^3)*(P0 - P_i_w(5)).*(r(k)^2-a^2).^2); %PET Membrane
wplot_m6(k) = separateUnits(pi*(1-v_MEM^2)/(16*E_MEM*t_PET^3)*(P0 - P0).*(r(k)^2-a^2).^2); %PET Membrane
end



figure
hold on
plot(rp,wplot_m1,'LineWidth',2)
plot(rp,wplot_m2,'LineWidth',2)
plot(rp,wplot_m3,'LineWidth',2)
plot(rp,wplot_m4,'LineWidth',2)
plot(rp,wplot_m5,'LineWidth',2)
plot(rp,wplot_m6,'LineWidth',2)
xlim('tight')
ylim('tight')
title('Membrane deflection',' ')
subtitle('(a=100Âţm, t_m = 30Âţm, Material: PDMS)')
xlabel('Crossection of membrane in [m]')
ylabel('Height of membrane in [m]')
legend('13kPa', '31kPa', '49kPa', '67kPa', '85kPa', 'P_i \approx P_0')

% *Radius*

wplot_ma1 = separateUnits(pi*(1-v_MEM^2)/(16*E_MEM*t_PET^3)*(P0 -  P_s_ma1).*(as.^2).^2); %PET Membrane
wplot_ma2 = separateUnits(pi*(1-v_MEM^2)/(16*E_MEM*t_PET^3)*(P0 -  P_s_ma2).*(as.^2).^2); %PET Membrane
wplot_ma3 = separateUnits(pi*(1-v_MEM^2)/(16*E_MEM*t_PET^3)*(P0 -  P_s_ma3).*(as.^2).^2); %PET Membrane
wplot_ma4 = separateUnits(pi*(1-v_MEM^2)/(16*E_MEM*t_PET^3)*(P0 -  P_s_ma4).*(as.^2).^2); %PET Membrane
wplot_ma5 = separateUnits(pi*(1-v_MEM^2)/(16*E_MEM*t_PET^3)*(P0-  P_s_ma5).*(as.^2).^2); %PET Membrane
wplot_ma6 = separateUnits(pi*(1-v_MEM^2)/(16*E_MEM*t_PET^3)*(P0 -  P_s_ma6).*(as.^2).^2); %PET Membrane

figure
hold on
plot(separateUnits(as),wplot_ma1,'LineWidth',2)
plot(separateUnits(as),wplot_ma2,'LineWidth',2)
plot(separateUnits(as),wplot_ma3,'LineWidth',2)
plot(separateUnits(as),wplot_ma4,'LineWidth',2)
plot(separateUnits(as),wplot_ma5,'LineWidth',2)
plot(separateUnits(as),wplot_ma6,'LineWidth',2)
xlim('tight')
ylim('tight')
title('Max membrane deformation (\omega) vs Suction cup radius (a)',' ')
subtitle('(h=1Âţm, t_m = 30Âţm, Material: PDMS)')
xlabel('a [m]')
ylabel('Max membrane deformation [m]')

legend('13kPa', '31kPa', '49kPa', '67kPa', '85kPa', 'P_i \approx P_0')
%%
%
% *Initial height*

hh= linspace(1*10^-6*u.m,0.4*10^-4*u.m,100);
wplot_mh1 = separateUnits(pi*(1-v_MEM^2)/(16*E_MEM*t_PET^3)*(P0 -  P_s_mh1).*(a^2).^2); %PET Membrane
wplot_mh2 = separateUnits(pi*(1-v_MEM^2)/(16*E_MEM*t_PET^3)*(P0 -  P_s_mh2).*(a^2).^2); %PET Membrane
```

```
wplot_mh3 = separateUnits(pi*(1-v_MEM^2)/(16*E_MEM*t_PET^3)*(P0 -  P_s_mh3).*(a^2).^2); %PET Membrane
wplot_mh4 = separateUnits(pi*(1-v_MEM^2)/(16*E_MEM*t_PET^3)*(P0 -  P_s_mh4).*(a^2).^2); %PET Membrane
wplot_mh5 = separateUnits(pi*(1-v_MEM^2)/(16*E_MEM*t_PET^3)*(P0-  P_s_mh5).*(a^2).^2); %PET Membrane
wplot_mh6 = separateUnits(pi*(1-v_MEM^2)/(16*E_MEM*t_PET^3)*(P0 -  P_s_mh6).*(a^2).^2); %PET Membrane

figure
hold on
plot(separateUnits(hh),wplot_mh1,'LineWidth',2)
plot(separateUnits(hh),wplot_mh2,'LineWidth',2)
plot(separateUnits(hh),wplot_mh3,'LineWidth',2)
plot(separateUnits(hh),wplot_mh4,'LineWidth',2)
plot(separateUnits(hh),wplot_mh5,'LineWidth',2)
plot(separateUnits(hh),wplot_mh6,'LineWidth',2)
xlim('tight')
ylim('tight')
title('Max membrane deformation (\omega) vs Suction cup height (h)',' ')
subtitle('(a=100Âţm, t_m = 30Âţm, Material: PDMS)')
xlabel('h [m]')
ylabel('Max membrane deformation [m]')
legend('13kPa', '31kPa', '49kPa', '67kPa', '85kPa', 'P_i \approx P_0')


% *Membrane thickness*

tt= linspace(10*10^-6*u.m,1.7*10^-5*u.m,100);

wplot_mt1 = separateUnits(pi*(1-v_MEM^2)./(16*E_MEM*tt.^3).*(P0 -  P_s_mt1)*(a^2)^2); %PET Membrane
wplot_mt2 = separateUnits(pi*(1-v_MEM^2)./(16*E_MEM*tt.^3).*(P0 -  P_s_mt2)*(a^2)^2); %PET Membrane
wplot_mt3 = separateUnits(pi*(1-v_MEM^2)./(16*E_MEM*tt.^3).*(P0 -  P_s_mt3)*(a^2)^2); %PET Membrane
wplot_mt4 = separateUnits(pi*(1-v_MEM^2)./(16*E_MEM*tt.^3).*(P0 -  P_s_mt4)*(a^2)^2); %PET Membrane
wplot_mt5 = separateUnits(pi*(1-v_MEM^2)./(16*E_MEM*tt.^3).*(P0-  P_s_mt5)*(a^2)^2); %PET Membrane
wplot_mt6 = separateUnits(pi*(1-v_MEM^2)./(16*E_MEM*tt.^3).*(P0 -  P_s_mt6)*(a^2)^2); %PET Membrane

figure
hold on
plot(separateUnits(tt),wplot_mt1,'LineWidth',2)
plot(separateUnits(tt),wplot_mt2,'LineWidth',2)
plot(separateUnits(tt),wplot_mt3,'LineWidth',2)
plot(separateUnits(tt),wplot_mt4,'LineWidth',2)
plot(separateUnits(tt),wplot_mt5,'LineWidth',2)
plot(separateUnits(tt),wplot_mt6,'LineWidth',2)
xlim('tight')
ylim('tight')
title('Max membrane deformation (\omega) vs Membrane thickness (t_m)',' ')
subtitle('(h=1Âţm, a=100Âţm, Material: PDMS)')
xlabel('t [m]')
ylabel('Max membrane deformation [m]')
legend('13kPa', '31kPa', '49kPa', '67kPa', '85kPa', 'P_i \approx P_0')
% *Membrane material*

EE= linspace(E_MEM,E_MEM*10,100);

wplot_mE1 = separateUnits(pi*(1-v_MEM^2)./(16*EE*t_PET^3).*(P0 -  P_s_mE1).*(a^2).^2); %PET Membrane
wplot_mE2 = separateUnits(pi*(1-v_MEM^2)./(16*EE*t_PET^3).*(P0 -  P_s_mE2).*(a^2).^2); %PET Membrane
wplot_mE3 = separateUnits(pi*(1-v_MEM^2)./(16*EE*t_PET^3).*(P0 -  P_s_mE3).*(a^2).^2); %PET Membrane
wplot_mE4 = separateUnits(pi*(1-v_MEM^2)./(16*EE*t_PET^3).*(P0 -  P_s_mE4).*(a^2).^2); %PET Membrane
wplot_mE5 = separateUnits(pi*(1-v_MEM^2)./(16*EE*t_PET^3).*(P0-  P_s_mE5).*(a^2).^2); %PET Membrane
wplot_mE6 = separateUnits(pi*(1-v_MEM^2)./(16*EE*t_PET^3).*(P0 -  P_s_mE6).*(a^2).^2); %PET Membrane

figure
hold on
plot(separateUnits(EE),wplot_mE1,'LineWidth',2)
plot(separateUnits(EE),wplot_mE2,'LineWidth',2)
plot(separateUnits(EE),wplot_mE3,'LineWidth',2)
plot(separateUnits(EE),wplot_mE4,'LineWidth',2)
plot(separateUnits(EE),wplot_mE5,'LineWidth',2)
plot(separateUnits(EE),wplot_mE6,'LineWidth',2)
xlim('tight')
ylim('tight')
title('Max membrane deformation (\omega) vs Membrane youngs modulus (E)',' ')
subtitle('(h=1Âţm, a=100Âţm, t_m=30Âţm)')
```

```
xlabel('E [Pa]')
ylabel('Max membrane deformation [m]')
legend('13kPa', '31kPa', '49kPa', '67kPa', '85kPa', 'P_i \approx P_0')
%%
%% *Deformation experiment results*
% *Unpolished*

a = 768*10^-6*u.m;
wplot_m13 = vpa(separateUnits(pi*(1-v_MEM^2)/(16*E_MEM*t_PET^3)*(P0 - P_i(1)).*(0-a^2).^2))*10^6;
wplot_m40 = vpa(separateUnits(pi*(1-v_MEM^2)/(16*E_MEM*t_PET^3)*(P0 - P_i(16)).*(0-a^2).^2))*10^6;
wplot_m70 = vpa(separateUnits(pi*(1-v_MEM^2)/(16*E_MEM*t_PET^3)*(P0 - P_i(33)).*(0-a^2).^2))*10^6;

Plain_13 = [24 26 23];
SE_P13 = std(Plain_13)/sqrt(length(Plain_13))+1.5;
Plain_40 = [20.6 21.4];
SE_P40 = std(Plain_40)/sqrt(length(Plain_40))+1.5;
Plain_70 = [16 11];
SE_P70 = std(Plain_70)/sqrt(length(Plain_70))+1.5;
fit_data_P = [mean(Plain_13) mean(Plain_40) mean(Plain_70)];
Pressure = [separateUnits(P_i(1)/1000) separateUnits(P_i(16)/1000) separateUnits(P_i(33)/1000)];


figure
hold on
plot(separateUnits(P_i(1)/1000), separateUnits(wplot_m13),'*', 'MarkerEdgeColor','b')
errorbar(separateUnits(P_i(1)/1000),mean(Plain_13),SE_P13,'*','MarkerFaceColor','r','Color','r')

plot(separateUnits(P_i(16)/1000), separateUnits(wplot_m40),'*', 'MarkerEdgeColor','b')
errorbar(separateUnits(P_i(16)/1000),mean(Plain_40),SE_P40,'*','MarkerFaceColor','r','Color','r')

plot(separateUnits(P_i(33)/1000), separateUnits(wplot_m70),'*', 'MarkerEdgeColor','b')
errorbar(separateUnits(P_i(33)/1000),mean(Plain_70),SE_P70,'*','MarkerFaceColor','r','Color','r')


title('Membrane deflection per pressure ',' ')
subtitle('Unpolished membrane scaffold (a=768Âţm)')
xlabel('Induced pressure in [kPa]')
ylabel('Defelction of membrane in [Âţm]')
legend('Model', 'Measurements')
%%
% *Polished*

a = 741*10^-6*u.m;
wplot_m13 = vpa(separateUnits(pi*(1-v_MEM^2)/(16*E_MEM*t_PET^3)*(P0 - P_i(1)).*(0-a^2).^2))*10^6;
wplot_m40 = vpa(separateUnits(pi*(1-v_MEM^2)/(16*E_MEM*t_PET^3)*(P0 - P_i(16)).*(0-a^2).^2))*10^6;
wplot_m70 = vpa(separateUnits(pi*(1-v_MEM^2)/(16*E_MEM*t_PET^3)*(P0 - P_i(33)).*(0-a^2).^2))*10^6;
Polished_13 = [21 24 24];
SE_PP13 = std(Plain_13)/sqrt(length(Polished_13))+1.5;
Polished_40 = [8 12 17];
SE_PP40 = std(Polished_40)/sqrt(length(Polished_40))+1.5;
Polished_70 = [5 5 6];
SE_PP70 = std(Polished_70)/sqrt(length(Polished_70))+1.5;


figure
hold on
plot(separateUnits(P_i(1)/1000), separateUnits(wplot_m13),'*', 'MarkerEdgeColor','b')
errorbar(separateUnits(P_i(1)/1000),mean(Polished_13),SE_PP13,'*','MarkerFaceColor','r','Color','r')

plot(separateUnits(P_i(16)/1000), separateUnits(wplot_m40),'*', 'MarkerEdgeColor','b')
errorbar(separateUnits(P_i(16)/1000),mean(Polished_40),SE_PP40,'*','MarkerFaceColor','r','Color','r')

plot(separateUnits(P_i(33)/1000), separateUnits(wplot_m70),'*', 'MarkerEdgeColor','b')
errorbar(separateUnits(P_i(33)/1000),mean(Polished_70),SE_PP70,'*','MarkerFaceColor','r','Color','r')

title('Membrane deflection per pressure ',' ')
subtitle('Polished membrane scaffold  (a=741Âţm)')
xlabel('Induced pressure in [kPa]')
ylabel('Deflection of membrane in [Âţm]')
legend('Model', 'Measurements')

```

```
%%
% *Initial deformation*


Polished_14 = [20 17 15 12];
SE_PP14 = std(Polished_14)/sqrt(length(Polished_14))+1.5;
Polished_20 = [31 30 30 35];
SE_PP20 = std(Polished_20)/sqrt(length(Polished_20))+1.5;
Polished_26 = [60 75 44 60];
SE_PP26 = std(Polished_26)/sqrt(length(Polished_26))+1.5;
Polished_60 = [89 81 105 130];
SE_PP60 = std(Polished_60)/sqrt(length(Polished_60))+1.5;


figure
hold on
errorbar(0,0,0,'*','MarkerFaceColor','r','Color','r','LineWidth',2)

errorbar(0.7,mean(Polished_14),SE_PP14,'*','MarkerFaceColor','r','Color','r','LineWidth',2)

errorbar(1,mean(Polished_20),SE_PP20,'*','MarkerFaceColor','r','Color','r','LineWidth',2)

errorbar(1.3,mean(Polished_26),SE_PP26,'*','MarkerFaceColor','r','Color','r','LineWidth',2)

errorbar(3,mean(Polished_60),SE_PP60,'*','MarkerFaceColor','r','Color','r','LineWidth',2)


title('Membrane deflection at atmospheric pressure ',' ')
subtitle('Membrane: 3M 8991')
xlabel('Suction cup radius [mm]')
ylabel('Pre-deflection of membrane in [Âµm]')
%% *Ps_end - TPU*


P_s_m_end = linspace(P0*0.9999,P0*1.0001,20);
C0 = Vw3(P3)*P_s_m(1);
q1 = waitbar(0,'Calculating converged pressure for TPU. [1/2]');
for k=1:20
    waitbar(k/20,q1);
    rv0_end_m(k,:) = sqrt(sqrt(w_V0*16*E_MEM*t_PET^3./( pi*(1-v_MEM^2)*(P_s_m_end(k)-P_i_w)))+a^2);
    wmax_end_m(k,:) = vpa(pi*(1-v_MEM^2)./(16*E_MEM*t_PET^3).*(P_s_m_end(k)-P_i_w)*a^4);
    Vw_end_m_tpu1(k) = vpa(int((0.5*rv0_end_m(k,1))^2*pi,0,wmax_end_m(k,1)));
    Vw_end_m_tpu3(k) = vpa(int((0.5*rv0_end_m(k,3))^2*pi,0,wmax_end_m(k,3)));
    Vw_end_m_tpu5(k) = vpa(int((0.5*rv0_end_m(k,5))^2*pi,0,wmax_end_m(k,5)));
    Vw_end_m_tpu6(k) = vpa(int((0.5*rv0_end_m(k,6))^2*pi,0,wmax_end_m(k,6)));
end
close(q1)

q2 = waitbar(0,'Calculating converged pressure for TPU. [2/2]');
for k=1:20
    waitbar(k/20,q2);
    rv0_end_tpu(k) = sqrt(sqrt(w_V0*16*E_tpu*t_tpu^3./( pi*(1-v_tpu^2)*(P0-P_s_m_end(k))))+a^2);
    wmax_end_tpu(k) = vpa(pi*(1-v_tpu^2)./(16*E_tpu*t_tpu^3).*(P0-P_s_m_end(k))*a^4);
    Vw_end_tpu(k) = vpa(int((0.5*rv0_end_tpu(k))^2*pi,0,wmax_end_tpu(k)));
end
close(q2)
C_end = [(Vw_end_m_tpu1(:)-Vw_end_tpu(:)).*P_s_m_end(:), (Vw_end_m_tpu3(:)-Vw_end_tpu(:)).*P_s_m_end(:), (
    Vw_end_m_tpu5(:)-Vw_end_tpu(:)).*P_s_m_end(:), (Vw_end_m_tpu6(:)-Vw_end_tpu(:)).*P_s_m_end(:)];

C_min1 = abs(C_end(:,1)/C0 -1);
[C_value1, Ck1] = min(C_min1(:));
P_s_m_end_1_tpu=vpa(P_s_m_end(Ck1))

C_min3 = abs(C_end(:,2)/C0 -1);
[C_value3, Ck3] = min(C_min3(:));
P_s_m_end_3_tpu=vpa(P_s_m_end(Ck3))

C_min5 = abs(C_end(:,3)/C0 -1);
[C_value5, Ck5] = min(C_min5(:));
P_s_m_end_5_tpu=vpa(P_s_m_end(Ck5))
```

```
664
665 C_min6 = abs(C_end(:,4)/C0 -1);
666 [C_value6, Ck6] = min(C_min6(:));
667 P_s_m_end_6_tpu=vpa(P_s_m_end(Ck6))
668 %% *Ps_end - Copper*
669
670 P_s_m_end = linspace(P0*0.9,P0*1.3,20);
671
672 q1 = waitbar(0,'Calculating converged pressure for Copper. [1/2]');
673 for k=1:20
674     waitbar(k/20,q1);
675     rv0_end_m_c(k,:) = sqrt(sqrt(w_V0*16*E_c*t_c^3./( pi*(1-v_c^2)*(P_s_m_end(k)-P_i_w)))+a^2);
676     wmax_end_m_c(k,:) = vpa(pi*(1-v_c^2)./(16*E_c*t_c^3).*(P_s_m_end(k)-P_i_w)*a^4);
677     Vw_end_m_c1(k) = vpa(int((0.5*rv0_end_m_c(k,1))^2*pi,0,wmax_end_m_c(k,1)));
678     Vw_end_m_c3(k) = vpa(int((0.5*rv0_end_m_c(k,3))^2*pi,0,wmax_end_m_c(k,3)));
679     Vw_end_m_c5(k) = vpa(int((0.5*rv0_end_m_c(k,5))^2*pi,0,wmax_end_m_c(k,5)));
680     Vw_end_m_c6(k) = vpa(int((0.5*rv0_end_m_c(k,6))^2*pi,0,wmax_end_m_c(k,6)));
681 end
682 close(q1)
683
684 q2 = waitbar(0,'Calculating converged pressure for Copper. [2/2]');
685 for k=1:20
686     waitbar(k/20,q2);
687     rv0_end_c(k) = sqrt(sqrt(w_V0*16*E_c*t_c^3./( pi*(1-v_c^2)*(P0-P_s_m_end(k))))+a^2);
688     wmax_end_c(k) = vpa(pi*(1-v_c^2)./(16*E_c*t_c^3).*(P0-P_s_m_end(k))*a^4);
689     Vw_end_c(k) = vpa(int((0.5*rv0_end_c(k))^2*pi,0,wmax_end_c(k)));
690 end
691 close(q2)
692 C_end_c = [(Vw_end_m_c1(:)-Vw_end_c(:)).*P_s_m_end(:), (Vw_end_m_c3(:)-Vw_end_c(:)).*P_s_m_end(:), (
        Vw_end_m_c5(:)-Vw_end_c(:)).*P_s_m_end(:), (Vw_end_m_c6(:)-Vw_end_c(:)).*P_s_m_end(:)];
693
694 C_min1_c = abs(C_end_c(:,1)/C0 -1);
695 [C_value1, Ck1_c] = min(C_min1_c(:));
696 P_s_m_end_1_c=vpa(P_s_m_end(Ck1_c))
697
698 C_min3_c = abs(C_end_c(:,2)/C0 -1);
699 [C_value3, Ck3_c] = min(C_min3_c(:));
700 P_s_m_end_3_c=vpa(P_s_m_end(Ck3_c))
701
702 C_min5_c = abs(C_end_c(:,3)/C0 -1);
703 [C_value5, Ck5_c] = min(C_min5_c(:));
704 P_s_m_end_5_c=vpa(P_s_m_end(Ck5_c))
705
706 C_min6_c = abs(C_end_c(:,4)/C0 -1);
707 [C_value6, Ck6_c] = min(C_min6_c(:));
708 P_s_m_end_6_c=vpa(P_s_m_end(Ck6_c))
709 %% *Deformation converged state*
710
711
712 for k=1:n
713 wplot_m_1_tpu(k) = separateUnits(pi*(1-v_MEM^2)/(16*E_MEM*t_PET^3)*(P_s_m_end_1_tpu - P_i_w(1)).*(r(k)^2-a
        ^2).^2); %PET Membrane  + TPU
714 wplot_m_3_tpu(k) = separateUnits(pi*(1-v_MEM^2)/(16*E_MEM*t_PET^3)*(P_s_m_end_3_tpu - P_i_w(3)).*(r(k)^2-a
        ^2).^2); %PET Membrane  + TPU
715 wplot_m_5_tpu(k) = separateUnits(pi*(1-v_MEM^2)/(16*E_MEM*t_PET^3)*(P_s_m_end_5_tpu - P_i_w(5)).*(r(k)^2-a
        ^2).^2); %PET Membrane  + TPU
716 wplot_m_6_tpu(k) = separateUnits(pi*(1-v_MEM^2)/(16*E_MEM*t_PET^3)*(P_s_m_end_6_tpu - P_i_w(6)).*(r(k)^2-a
        ^2).^2); %PET Membrane  + TPU
717
718 wplot_m_1_c(k) = separateUnits(pi*(1-v_MEM^2)/(16*E_MEM*t_PET^3)*(P_s_m_end_1_c - P_i_w(1)).*(r(k)^2-a^2)
        .^2); %PET Membrane  + Copper
719 wplot_m_3_c(k) = separateUnits(pi*(1-v_MEM^2)/(16*E_MEM*t_PET^3)*(P_s_m_end_3_c - P_i_w(3)).*(r(k)^2-a^2)
        .^2); %PET Membrane  + Copper
720 wplot_m_5_c(k) = separateUnits(pi*(1-v_MEM^2)/(16*E_MEM*t_PET^3)*(P_s_m_end_5_c - P_i_w(5)).*(r(k)^2-a^2)
        .^2); %PET Membrane  + Copper
721 wplot_m_6_c(k) = separateUnits(pi*(1-v_MEM^2)/(16*E_MEM*t_PET^3)*(P_s_m_end_6_c - P_i_w(6)).*(r(k)^2-a^2)
        .^2); %PET Membrane  + Copper
722
723 end
724
725 for k =1:n
```

```
726     wplot_c1(k) = separateUnits(pi*(1-v_c^2)/(16*E_c*t_c^3)*(P0-P_s_m_end_1_c).*(r(k)^2-a^2).^2); %Copper
727     wplot_c3(k) = separateUnits(pi*(1-v_c^2)/(16*E_c*t_c^3)*(P0-P_s_m_end_3_c).*(r(k)^2-a^2).^2); %Copper
728     wplot_c5(k) = separateUnits(pi*(1-v_c^2)/(16*E_c*t_c^3)*(P0-P_s_m_end_5_c).*(r(k)^2-a^2).^2); %Copper
729     wplot_c6(k) = separateUnits(pi*(1-v_c^2)/(16*E_c*t_c^3)*(P0-P_s_m_end_6_c).*(r(k)^2-a^2).^2); %Copper
730
731     wplot_tpu1(k) = separateUnits(pi*(1-v_tpu^2)/(16*E_tpu*t_tpu^3)*(P0-P_s_m_end_1_tpu).*(r(k)^2-a^2).^2)
            ; %TPU
732     wplot_tpu3(k) = separateUnits(pi*(1-v_tpu^2)/(16*E_tpu*t_tpu^3)*(P0-P_s_m_end_3_tpu).*(r(k)^2-a^2).^2)
            ; %TPU
733     wplot_tpu5(k) = separateUnits(pi*(1-v_tpu^2)/(16*E_tpu*t_tpu^3)*(P0-P_s_m_end_5_tpu).*(r(k)^2-a^2).^2)
            ; %TPU
734     wplot_tpu6(k) = separateUnits(pi*(1-v_tpu^2)/(16*E_tpu*t_tpu^3)*(P0-P_s_m_end_6_tpu).*(r(k)^2-a^2).^2)
            ; %TPU
735 end
736
737 figure
738 hold on
739 plot(rp,wplot_m_1_tpu,'Color',  '#EDB120')
740 plot(rp,wplot_tpu1,'--','Color',        '#EDB120')
741 plot(rp,wplot_m_1_c,'Color', '#D95319')
742 plot(rp,wplot_c1,'--','Color', '#D95319')
743 xlim('tight')
744 title('Membrane and laminate deflection (P_i = 13kpa)',' ')
745 xlabel('Crossection of membrane in [m]')
746 ylabel('Height of membrane in [m]')
747 legend('PET', 'Polyurethane', 'PET', 'Copper', 'Location','northeastoutside')
748 %ylim([0.0000000 0.0000025])
749
750 figure
751 hold on
752 plot(rp,wplot_m_3_tpu,'Color',  '#EDB120')
753 plot(rp,wplot_tpu3,'--','Color',        '#EDB120')
754 plot(rp,wplot_m_3_c,'Color', '#D95319')
755 plot(rp,wplot_c3,'--','Color', '#D95319')
756 xlim('tight')
757 title('Membrane and laminate deflection (P_i = 49kpa)',' ')
758 xlabel('Crossection of membrane in [m]')
759 ylabel('Height of membrane in [m]')
760 legend('PET', 'Polyurethane', 'PET', 'Copper', 'Location','northeastoutside')
761 % ylim([0.0000000 0.0000025])
762 %
763 figure
764 hold on
765 plot(rp,wplot_m_5_tpu,'Color',  '#EDB120')
766 plot(rp,wplot_tpu5,'--','Color',        '#EDB120')
767 plot(rp,wplot_m_5_c,'Color', '#D95319')
768 plot(rp,wplot_c5,'--','Color', '#D95319')
769 xlim('tight')
770 title('Membrane and laminate deflection (P_i = 85kpa)',' ')
771 xlabel('Crossection of membrane in [m]')
772 ylabel('Height of membrane in [m]')
773 legend('PET', 'Polyurethane', 'PET', 'Copper', 'Location','northeastoutside')
774 % ylim([-0.0000002 0.0000025])
775 %
776 figure
777 hold on
778 plot(rp,wplot_m_6_tpu,'Color',  '#EDB120')
779 plot(rp,wplot_tpu6,'--','Color',        '#EDB120')
780 plot(rp,wplot_m_6_c,'Color', '#D95319')
781 plot(rp,wplot_c6,'--','Color', '#D95319')
782 xlim('tight')
783 title('Membrane and laminate deflection (P_i = P_0)',' ')
784 xlabel('Crossection of membrane in [m]')
785 ylabel('Height of membrane in [m]')
786 legend('PET', 'Polyurethane', 'PET', 'Copper', 'Location','northeastoutside')
787 % ylim([-0.0000002 0.0000025])
788 %%
789 %
790 %% *Change of suction cup radius: suction*
791
792
```

```
%%

%Figuur 2b - Change of suctiocup radius
%--------------------------------------
figure
hold on
plot(separateUnits(as),separateUnits(S_PET_maxa))
plot(separateUnits(as),separateUnits(S_PET_maxac))
plot(separateUnits(as),separateUnits(S_tpu_maxa))
xlim('tight')
title('Maximum stress (\sigma_{y_{max}}) vs Suction cup radius (a)',' ')
subtitle('(P_i = 13kpa)')
xlabel('a [m]')
ylabel('\sigma_{y_{max}} [Pa]')
legend('Membrane uncovered', 'Membrane + Laminate', 'Laminate','Location','northeastoutside')

%%
% *Initial height/volume: Suction*



% figure
% hold on
% plot(separateUnits(hh),separateUnits(S_PET_maxh))
% plot(separateUnits(hh),separateUnits(S_c_maxh))
% plot(separateUnits(hh),separateUnits(S_tpu_maxh))
% xlim('tight')
% title('Max stress (\sigma_{y_{max}}) vs Suction cup height (h)',' ')
% subtitle('(P_i = 45kpa)')
% xlabel('h [m]')
% ylabel('\sigma_{y_{max}} [Pa]')
% legend('PET', 'Copper', 'Polyurethane','Location','northeastoutside')


%%
% *membrane movement: Suction*

% z=51;
% P_i_w = [P_i(1),P_i(11),P_i(21),P_i(31),P_i(41),P_i(51)];
% P_s_mw = [P_s_m(1),P_s_m(11),P_s_m(21),P_s_m(31),P_s_m(41),P_s_m(51)];
%
% r = linspace(-a,a,n);
% rp = separateUnits(r);
% for k=1:n
% wplot_m_1(k) = separateUnits(h + pi*(1-v_MEM^2)/(16*E_MEM*t_PET^3)*(P_s_mw(1) - P_i_w(1)).*(r(k)^2-a^2)
      .^2); %PET Membrane
% wplot_m_2(k) = separateUnits(h + pi*(1-v_MEM^2)/(16*E_MEM*t_PET^3)*(P_s_mw(2) - P_i_w(2)).*(r(k)^2-a^2)
      .^2); %PET Membrane
% wplot_m_3(k) = separateUnits(h + pi*(1-v_MEM^2)/(16*E_MEM*t_PET^3)*(P_s_mw(3) - P_i_w(3)).*(r(k)^2-a^2)
      .^2); %PET Membrane
% wplot_m_4(k) = separateUnits(h + pi*(1-v_MEM^2)/(16*E_MEM*t_PET^3)*(P_s_mw(4) - P_i_w(4)).*(r(k)^2-a^2)
      .^2); %PET Membrane
% wplot_m_5(k) = separateUnits(h + pi*(1-v_MEM^2)/(16*E_MEM*t_PET^3)*(P_s_mw(5) - P_i_w(5)).*(r(k)^2-a^2)
      .^2); %PET Membrane
% wplot_m_6(k) = separateUnits(h + pi*(1-v_MEM^2)/(16*E_MEM*t_PET^3)*(P_s_mw(6) - P_i_w(6)).*(r(k)^2-a^2)
      .^2); %PET Membrane
% end
%
% %Figuur 5
% %--------------------------------------
% figure
% hold on
% plot(rp,wplot_m_1)
% plot(rp,wplot_m_2)
% plot(rp,wplot_m_3)
% plot(rp,wplot_m_4)
% plot(rp,wplot_m_5)
% plot(rp,wplot_m_6)
%
% xlim('tight')
% title('PET membrane deflection vs Induced pressure (P_i)',' ')
```

```
% xlabel('Crossection of membrane in [m]')
% ylabel('Height of membrane in [m]')
% legend('P_i = 10kpa', 'P_i = 28kpa', 'P_i = 46kpa', 'P_i = 65kpa', 'P_i = 83kpa', 'P_i \approx P_0','Location','northeastoutside')
% ylim([0.0000010 0.0000035])
% %Other material movement
% P_s_cw = [P_s_c(1),P_s_c(11),P_s_c(21),P_s_c(31),P_s_c(41),P_s_c(51)];
% P_s_tpuw = [P_s_tpu(1),P_s_tpu(11),P_s_tpu(21),P_s_tpu(31),P_s_tpu(41),P_s_tpu(51)];
% for k =1:n
%     wplot_c1(k) = separateUnits(pi*(1-v_c^2)/(16*E_c*t_c^3)*(P_s_cw(1)-P_s_mw(1)).*(r(k)^2-a^2).^2); % Copper
%     wplot_c3(k) = separateUnits(pi*(1-v_c^2)/(16*E_c*t_c^3)*(P_s_cw(3)-P_s_mw(3)).*(r(k)^2-a^2).^2); % Copper
%     wplot_c5(k) = separateUnits(pi*(1-v_c^2)/(16*E_c*t_c^3)*(P_s_cw(5)-P_s_mw(5)).*(r(k)^2-a^2).^2); % Copper
%
%     wplot_tpu1(k) = separateUnits(pi*(1-v_tpu^2)/(16*E_tpu*t_tpu^3)*(P_s_tpuw(1)-P_s_mw(1)).*(r(k)^2-a^2).^2); %TPU
%     wplot_tpu3(k) = separateUnits(pi*(1-v_tpu^2)/(16*E_tpu*t_tpu^3)*(P_s_tpuw(3)-P_s_mw(3)).*(r(k)^2-a^2).^2); %TPU
%     wplot_tpu5(k) = separateUnits(pi*(1-v_tpu^2)/(16*E_tpu*t_tpu^3)*(P_s_tpuw(5)-P_s_mw(5)).*(r(k)^2-a^2).^2); %TPU
% end
%
% figure
% hold on
% plot(rp,wplot_m_1)
% plot(rp,wplot_c1)
% plot(rp,wplot_tpu1)
% xlim('tight')
% title('Membrane and laminate deflection (P_i = 10kpa)',' ')
% xlabel('Crossection of membrane in [m]')
% ylabel('Height of membrane in [m]')
% legend('PET', 'Copper', 'Polyurethane','Location','northeastoutside')
% ylim([0.0000000 0.0000035])
%
% figure
% hold on
% plot(rp,wplot_m_3)
% plot(rp,wplot_c3)
% plot(rp,wplot_tpu3)
% xlim('tight')
% title('Membrane and laminate deflection (P_i = 46kpa)',' ')
% xlabel('Crossection of membrane in [m]')
% ylabel('Height of membrane in [m]')
% legend('PET', 'Copper', 'Polyurethane','Location','northeastoutside')
% ylim([0.0000000 0.0000035])
%
% figure
% hold on
% plot(rp,wplot_m_5)
% plot(rp,wplot_c5)
% plot(rp,wplot_tpu5)
% xlim('tight')
% title('Membrane and laminate deflection (P_i = 83kpa)',' ')
% xlabel('Crossection of membrane in [m]')
% ylabel('Height of membrane in [m]')
% legend('PET', 'Copper', 'Polyurethane','Location','northeastoutside')
% ylim([0.0000000 0.0000035])
%
%% FORCES

%-------------------------------------------------------------------------

%Gravity
F_gc = g * rho_c*t_c * A_S; % Copper gravity force
F_gtpu = g * rho_tpu*t_tpu * A_S; % Tpu gravity force
%-------------------------------------------------------------------------

%Interaction energy
%-------------------------------------------------------------------------
```

```
%The layer interaction force at point of pick up, thus only the force with
%the carrier material
%--------------------------------------------------------------------------
%Van der waals paramaters
d_c0 = 0.165* 10^-9*u.m; %min cut-off distance
d_0 = 20* 10^-9*u.m; %max cut-off distance
%--------------------------------------------------------------------------
D_i = vpa(linspace(d_c0,10^-5*u.m,i_l));
%COPPER
rehash toolboxcache
q = waitbar(0,'Calculating interaction forces. Please wait...');

for i=1:i_l
waitbar(i/i_l,q);
        e_vdw_c(i) = Ham_c/(12*pi*D_i(i)^2);
%F_vdw_c(i) = separateUnits(e_vdw_c/D_i(i)*A_f);
%Casimir Force
e_casimir_c(i)=separateUnits(vpa(pi^2*h_p*c/(2*pi*720*D_i(i)^3)));
%F_casimir_c(i) = separateUnits(pi*h_p*c*A_f/(240*D_i(i)));

%Capillary force
gamma = (75.6-0.167*(T-273))*10^-3;
d_cap_c = -2 * gamma*v_w * cosd(c_Ac) / (R*T*log10(0.999));
  if separateUnits(D_i(i)) <= separateUnits(d_cap_c)
        e_cap_c(i) = gamma*(-cosd(c_Ac)+cosd(c_AMEM));
    end
    if separateUnits(D_i(i)) > separateUnits(d_cap_c)
       e_cap_c(i) = 0;
    end
e_cap_c(i) = separateUnits(vpa(e_cap_c(i)));
%F_cap_c(i) = separateUnits(e_cap_c(i)/D_i(i)*A_f);

%F_CL_c(i) = vpa(F_casimir_c(i) + F_vdw_c(i) + F_cap_c(i)); % Total interaction force with carrier
     material in the case of copper
e_CL_c(i) = vpa(separateUnits(e_vdw_c(i)) + e_casimir_c(i) + e_cap_c(i));
end
close(q)
figure
loglog(separateUnits(D_i),e_CL_c)
hold on
loglog(separateUnits(D_i),separateUnits(e_vdw_c))
loglog(separateUnits(D_i),e_casimir_c)
loglog(separateUnits(D_i),e_cap_c)
title('Copper interlayer ineteraction energy vs distance',' ')
subtitle(['R_H = 99.9%'])
xlabel('Distance to laminate [m]')
ylabel('Interaction energy [J/m^2]')
legend('Total', 'Van der Waals', 'Casimir','Capillary')
%D_cap vs Relative humidity
% for y=1:i_l
% d_cap_c_d(y) = -2 * gamma*v_w * cosd(c_Ac) / (R*T*log10(H_r(y)));
% end
% figure
% plot(separateUnits(d_cap_c_d),H_r*100)
% title('Capillary condensation distance vs Relative humidity',' ')
% subtitle(['Material: Copper (\theta = 86Âř)'])
% xlabel('Capillary condensation distance [m]')
% ylabel('Relative humidity [%]')
%
%  ylim([0.00 100])

%%
%% Interaction forces

gamma = (75.6-0.167*(T-273))*10^-3;
%(F_CL) (ALU vs laminate)
%--------------------------------------------------------------------------
%cappillary condesation distance for eman humidy netherlands
d_cap_alu = 2 * gamma*v_w * cosd(c_Aalu) / (R*T*log10(0.81));
d_cap_c = -2 * gamma*v_w * cosd(c_Ac) / (R*T*log10(0.81));
d_cap_tpu = 2 * gamma*v_w * cosd(c_Atpu) / (R*T*log10(0.81));
```

```
d_cap_PET = -2 * gamma*v_w * cosd(c_AMEM) / (R*T*log10(0.81));

%Copper
e_vdw_c_fcl = Ham_c/(12*pi*(z_c+z_alu)^2)
Pa_vdw_c_fcl= vpa(separateUnits(e_vdw_c_fcl/(z_c+z_alu)));
%Zero as carrier surface roughness is larger than the capillary condensation distance
e_cap_c_fcl = gamma*(-cosd(c_Ac)+cosd(c_AMEM))
%Pa_cap_c_f_cl = vpa(separateUnits(e_cap_c_fcl/(z_c+z_MEM)));
e_casimir_cfcl =pi^2*h_p*c/(2*pi*720*(z_c+z_alu)^3)
Pa_casimir_c_fcl = vpa(separateUnits(e_casimir_cfcl/(z_c+z_alu)));
Pa_CL_c = (Pa_vdw_c_fcl + Pa_casimir_c_fcl)*u.kg*u.m/u.s^2/u.m^2;


%TPU
e_vdw_tpu_fcl = Ham_c/(12*pi*(z_tpu+z_alu)^2);
Pa_vdw_tpu_fcl= vpa(separateUnits(e_vdw_tpu_fcl/(z_tpu+z_alu)));
%Zero as carrier surface roughness is larger than the capillary condensation distance
e_cap_tpu_fcl = gamma*(-cosd(c_Atpu)+cosd(c_AMEM))
%Pa_cap_tpu_fcl = vpa(separateUnits(e_cap_tpu_fcl/(z_tpu+z_MEM)));
e_casimir_tpu_fcl =pi^2*h_p*c/(2*pi*720*(z_tpu+z_alu)^3);
Pa_casimir_tpu_fcl = vpa(separateUnits(e_casimir_tpu_fcl/(z_tpu+z_alu)));
Pa_CL_tpu = (Pa_vdw_tpu_fcl + Pa_casimir_tpu_fcl)*u.kg*u.m/u.s^2/u.m^2;

%-------------------------------------------------------------------------
%Interaction forces (F_E) (end-effector vs Laminate)
%-------------------------------------------------------------------------

%Copper
e_vdw_c_fe = Ham_c/(12*pi*(z_c+z_MEM)^2);
Pa_vdw_c_fe= vpa(separateUnits(e_vdw_c_fe/(z_c+z_MEM)));
%Zero as surface roughness is larger than the capillary condensation distance
  e_cap_c_fe = gamma*(2*cosd(c_Ac))
% Pa_cap_c_fe = vpa(separateUnits(e_cap_c_fe/(z_c+z_MEM)));
e_casimir_c_fe =pi^2*h_p*c/(2*pi*720*(z_c+z_MEM)^3);
Pa_casimir_c_fe = vpa(separateUnits(e_casimir_c_fe/(z_c+z_MEM)));
Pa_FE_c = (Pa_vdw_c_fe + Pa_casimir_c_fe)*u.kg*u.m/u.s^2/u.m^2;

%TPU
e_vdw_tpu_fe = Ham_c/(12*pi*(z_tpu+z_MEM)^2);
Pa_vdw_tpu_fe= vpa(separateUnits(e_vdw_tpu_fe/(z_tpu+z_MEM)));
%Zero as surface roughness is larger than the capillary condensation distance
  e_cap_tpu_fe = gamma*(-2*cosd(c_Atpu))
% Pa_cap_tpu_fe =vpa(separateUnits(e_cap_tpu_fe/(z_tpu+z_MEM)));
e_casimir_tpu_fe =pi^2*h_p*c/(2*pi*720*(z_tpu+z_MEM)^3);
Pa_casimir_tpu_fe = vpa(separateUnits(e_casimir_tpu_fe/(z_tpu+z_MEM)));
Pa_FE_tpu = (Pa_vdw_tpu_fe + Pa_casimir_tpu_fe)*u.kg*u.m/u.s^2/u.m^2;

%-------------------------------------------------------------------------
%Interaction forces (F_RL) (Laminate vs Laminate)
%-------------------------------------------------------------------------

%Copper
e_vdw_c_frl = Ham_c/(12*pi*(z_c+z_c)^2);
Pa_vdw_c_frl= vpa(separateUnits(e_vdw_c_frl/(z_c+z_c)));
e_cap_c_frl = gamma*(2*cosd(c_Ac));
Pa_cap_c_frl = vpa(separateUnits(e_cap_c_frl/(z_c+z_c)));
e_casimir_c_frl =pi^2*h_p*c/(2*pi*720*(z_c+z_c)^3);
Pa_casimir_c_frl = vpa(separateUnits(e_casimir_c_frl/(z_c+z_c)));
Pa_RL_c = (Pa_vdw_c_frl  + Pa_casimir_c_frl)*u.kg*u.m/u.s^2/u.m^2;

%TPU
e_vdw_tpu_frl = Ham_c/(12*pi*(z_tpu+z_tpu)^2);
Pa_vdw_tpu_frl= vpa(separateUnits(e_vdw_tpu_frl/(z_tpu+z_tpu)));
%Zero as surface roughness is larger than the capillary condensation distance
e_cap_tpu_frl = gamma*(-2*cosd(c_Atpu))
%Pa_cap_tpu_frl =vpa(separateUnits(e_cap_tpu_frl/(z_tpu+z_tpu)));
e_casimir_tpu_frl =pi^2*h_p*c/(2*pi*720*(z_tpu+z_tpu)^3);
Pa_casimir_tpu_frl = vpa(separateUnits(e_casimir_tpu_frl/(z_tpu+z_tpu)));
Pa_RL_tpu = (Pa_vdw_tpu_frl  + Pa_casimir_tpu_frl)*u.kg*u.m/u.s^2/u.m^2;
```

```
%% *Force prediction in laminate pick-up for a= 0.7*10^-3 [m]     !!!per suction cup!!!*

%-------------------------------------------------------------------------
%Pickup copper -- per suction cup
F_pickup_c_a = -separateUnits(P_s_m_end_1_c-P0) * separateUnits(pi*a^2);
F_stiction_c_a = separateUnits(-Pa_CL_c+Pa_FE_c)* separateUnits(pi*(p_scm+a)^2)+separateUnits(Pa_FE_c)*
    separateUnits(pi*(p_scm^2-a^2));
F_res_c_a = F_pickup_c_a + F_stiction_c_a;

%Pickup tpu
F_pickup_tpu_a = -separateUnits(P_s_m_end_1_tpu-P0) * separateUnits(pi*a^2);
F_stiction_tpu_a = -separateUnits(-Pa_CL_tpu+Pa_FE_c)* separateUnits(pi*(p_scm+a)^2)+separateUnits(
    Pa_FE_tpu)* separateUnits(pi*(p_scm^2-a^2));
F_res_tpu_a = F_pickup_tpu_a + F_stiction_tpu_a;


%release copper -- per suction cup
F_release_c_a = -separateUnits(P_s_m_end_6_c-P0) * separateUnits(pi*a^2);

%release tpu -- per suction cup
F_release_tpu_a = -separateUnits(P_s_m_end_6_tpu-P0) * separateUnits(pi*a^2);
%%
% *Force experiment (solid surface)*
%
% _no suction pressure is present under to be picked up laminate_

%-------------------------------------------------------------------------
%Pickup copper -- per suction cup
for k=1:99
F_pickup_c(k) = separateUnits(P0-P_s_ma1(k)) * separateUnits(as(k).^2)*pi;
F_stiction_c(k) = separateUnits(-Pa_CL_c+Pa_FE_c)* separateUnits(pi*(p_scm+as(k))^2);
F_res_c(k) = F_pickup_c(k) + F_stiction_c(k);

%Pickup tpu
F_pickup_tpu(k) = separateUnits(P_s_ma1(k)-P0) * separateUnits(as(k).^2)*pi;
F_stiction_tpu(k) = -separateUnits(-Pa_CL_tpu+Pa_FE_c)* separateUnits(pi*(p_scm+as(k))^2);
F_res_tpu(k) = F_pickup_tpu(k) + F_stiction_tpu(k);
end

figure
hold on
plot(separateUnits(as(1:99)),separateUnits(F_pickup_c*N_p),'LineWidth',2)
plot(separateUnits(as(1:99)),separateUnits(F_stiction_c*N_p),'Color', '#D95319','LineWidth',2)
plot(separateUnits(as(1:99)),separateUnits(F_stiction_tpu*N_p),'--','Color','#EDB120','LineWidth',2)
plot([0.7 1 1.3 3]*10^-3, separateUnits([F07 F10 F13 F30]),'*','LineWidth',2);
plot([0.7 1 1.3 3]*10^-3, separateUnits(-1*[mean_force_des_07 mean_force_des_10 mean_force_des_13
    mean_force_des_30]),'*','LineWidth',2);
title('Force vs suction cup radius',' ')
subtitle(['Pickup of rigid undeformable laminate (P_i=13kPa)'])
xlabel('Suction cup radius [m]')
ylabel('Force generated by end-effecor [N]')
legend('Pickup force', 'Stiction - Copper', 'Stiction - TPU', 'Expected compensated force', 'Measured
    force' )
ylim('tight')

%%
%

a07s = [1436 1462 1464 1484]*0.5;
a07 = mean(a07s)*10^-6*u.m;
a10s = [1882 1880 1876 1930]*0.5;
a10 = mean(a10s)*10^-6*u.m;
a13s = [2541 2530 2520 2550]*0.5;
a13 = mean(a13s)*10^-6*u.m;
a30s = [5823 5801 5786 5769]*0.5;
a30 = mean(a30s)*10^-6*u.m;

t_oppervlate = 1.5*10^-3*u.m;
E_oppervlakte =5*10^6*u.kg*u.m/u.s^2/u.m^2;
f_w=1.8936; %factor between wmax and w_mean

```

```
h07_pre = 16/f_w*10^-6*u.m;
h10_pre = 31.5/f_w*10^-6*u.m;
h13_pre = 59.75/f_w*10^-6*u.m;
h30_pre = 101.25/f_w*10^-6*u.m;

h07_f = 3.8*10^-6*u.m;
h10_f = 2.3*10^-6*u.m;
h13_f = 1.8*10^-6*u.m;
h30_f = 0.9*10^-6*u.m;

% h07_d= (P0-P_s_ma7)*t_oppervlate/E_oppervlakte;
% h10_d= (P0-P_s_ma10)*t_oppervlate/E_oppervlakte;
% h13_d= (P0-P_s_ma13)*t_oppervlate/E_oppervlakte;

h07 = (h07_pre-h07_f);
h10 = (h10_pre-h10_f);
h13 = (h10_pre-h13_f);
h30 = (h30_pre-h30_f);

P_s_ma7 = vpa((P_i_w(1))/2 + sqrt(((P_i_w(1)) + (16*E_MEM*h07*t_PET^3)/(a07^4*(v_MEM^2 - 1)))^2 - (64*
    E_MEM*P0*h07*t_PET^3)/(a07^4*(v_MEM^2 - 1)))/2 + (8*E_MEM*h07*t_PET^3)/(a07^4*(v_MEM^2 - 1)));
P_s_ma10 = vpa((P_i_w(1))/2 + sqrt(((P_i_w(1)) + (16*E_MEM*h10*t_PET^3)/(a10^4*(v_MEM^2 - 1)))^2 - (64*
    E_MEM*P0*h10*t_PET^3)/(a10^4*(v_MEM^2 - 1)))/2 + (8*E_MEM*h10*t_PET^3)/(a10^4*(v_MEM^2 - 1)));
P_s_ma13 = vpa((P_i_w(1))/2 + sqrt(((P_i_w(1)) + (16*E_MEM*h13*t_PET^3)/(a13^4*(v_MEM^2 - 1)))^2 - (64*
    E_MEM*P0*h13*t_PET^3)/(a13^4*(v_MEM^2 - 1)))/2 + (8*E_MEM*h13*t_PET^3)/(a13^4*(v_MEM^2 - 1)));
P_s_ma30 = vpa((P_i_w(1))/2 + sqrt(((P_i_w(1)) + (16*E_MEM*h30*t_PET^3)/(a30^4*(v_MEM^2 - 1)))^2 - (64*
    E_MEM*P0*h30*t_PET^3)/(a30^4*(v_MEM^2 - 1)))/2 + (8*E_MEM*h30*t_PET^3)/(a30^4*(v_MEM^2 - 1)));


F07 = vpa((P0-P_s_ma7)*a07^2*pi*N_p)
F10 = vpa((P0-P_s_ma10)*a10^2*pi*N_p)
F13 = vpa((P0-P_s_ma13)*a13^2*pi*N_p)
F30 = vpa((P0-P_s_ma30)*a30^2*pi*N_p)
%%
%
%
%
%% *Force prediction vs changing side wal thickness -  Pick-up*

for k=1:100
%Copper
F_pickup_c_total = F_pickup_c_a*N_p;
F_stiction_c_total(k) = separateUnits(vpa(-Pa_CL_c*A_S+Pa_FE_c*(p_sv(k)^2-a^2)*pi*N_p));
F_res_total_c_v(k) = vpa(-separateUnits(F_gc)+F_stiction_c_total(k)+F_pickup_c_total);


%TPU
F_pickup_tpu_total = F_pickup_tpu_a*N_p;
F_stiction_tpu_total(k) = separateUnits(vpa(-Pa_CL_tpu*A_S+Pa_FE_tpu*(p_sv(k)^2-a^2)*pi*N_p));
F_res_total_tpu_v(k) = vpa(-separateUnits(F_gtpu)+F_stiction_tpu_total(k)+F_pickup_tpu_total);
end
figure
hold on
plot(separateUnits(p_sv),separateUnits(F_res_total_c_v),'Color', '#D95319')
title('Pick-up resultant force vs suction cup wall radius',' ')
subtitle('Copper (P_i=13kPa)')
xlabel('Suction cup wall radius [m]')
ylabel('Resultant force[N]')
xlim('tight')

figure
hold on
plot(separateUnits(p_sv),separateUnits(F_res_total_tpu_v),'Color','#EDB120')
title('Pick-up resultant force vs suction cup wall radius',' ')
subtitle('TPU (P_i=13kPa)')
xlabel('Suction cup wall radius [m]')
ylabel('Resultant force[N]')
xlim('tight')

%% *Release*

```

```
for k=1:100
%Copper
F_release_c_total = F_release_c_a*N_p;
F_stiction_c_total_r(k) = separateUnits(vpa(-Pa_RL_c*A_S+Pa_FE_c*(p_sv(k)^2-a^2)*pi*N_p));
F_res_total_c_v_r(k) = vpa(-separateUnits(F_gc)+F_stiction_c_total_r(k)+F_release_c_total);


%TPU
F_release_tpu_total = F_release_tpu_a*N_p;
F_stiction_tpu_total_r(k) = separateUnits(vpa(-Pa_RL_tpu*A_S+Pa_FE_tpu*(p_sv(k)^2-a^2)*pi*N_p));
F_res_total_tpu_v_r(k) = vpa(-separateUnits(F_gtpu)+F_stiction_tpu_total_r(k)+F_release_tpu_total);
end

figure
hold on
plot(separateUnits(p_sv),separateUnits(F_res_total_c_v_r),'Color', '#D95319')
title('Release resultant force vs suction cup wall radius',' ')
subtitle('Copper (P_i=13kPa)')
xlabel('Suction cup wall radius [m]')
ylabel('Resultant force[N]')
xlim('tight')

figure
hold on
plot(separateUnits(p_sv),separateUnits(F_res_total_tpu_v_r),'Color','#EDB120')
title('Release resultant force vs suction cup wall radius',' ')
subtitle('TPU (P_i=13kPa)')
xlabel('Suction cup wall radius [m]')
ylabel('Resultant force[N]')
xlim('tight')
%%
% *Force prediction in complete laminate pick-up for a= 0.7*10^-3 [m] and p
% = 1.5mm*

%Copper
F_pickup_c_total = F_pickup_c_a*N_p;
F_stiction_c_total = separateUnits(vpa(-Pa_CL_c*A_S+Pa_FE_c*(p_scm^2-a^2)*pi*N_p));
F_res_total_c = vpa(-separateUnits(F_gc)+F_stiction_c_total+F_pickup_c_total)


%TPU
F_pickup_tpu_total = F_pickup_tpu_a*N_p;
F_stiction_tpu_total = separateUnits(vpa(-Pa_CL_tpu*A_S+Pa_FE_tpu*(p_scm^2-a^2)*pi*N_p));
F_res_total_tpu = vpa(-separateUnits(F_gtpu)+F_stiction_tpu_total+F_pickup_tpu_total)

%%
% *Force prediction in complete laminate release for a= 0.7*10^-3 [m]  p=1.5mm*

%Copper
F_release_c_total_release = F_release_c_a*N_p;
F_stiction_cr_total = separateUnits(vpa(-Pa_RL_c*A_S+Pa_FE_c*(p_scm^2-a^2)*pi));
F_res_total_c_release = vpa(-separateUnits(F_gc)+F_stiction_cr_total+F_release_c_total_release)


%TPU
F_pickup_tpu_total_release = F_release_tpu_a*N_p;
F_stiction_tpur_total = separateUnits(vpa(-Pa_RL_tpu*A_S+Pa_FE_tpu*(p_scm^2-a^2)*pi));
F_res_total_tpu_release = vpa(-separateUnits(F_gtpu)+F_stiction_tpur_total+F_pickup_tpu_total_release)
```